



UNIVERSITÀ DEGLI STUDI DI NAPOLI
FEDERICO II



UNIVERSITÀ DEGLI STUDI DI NAPOLI FEDERICO II

PH.D. THESIS

IN

INFORMATION TECHNOLOGY AND ELECTRICAL ENGINEERING

**SPACEBORNE RADAR FOR
SPACE SITUATIONAL AWARENESS**

MARCO MAFFEI

TUTOR: PROF. ANTONIO DE MAIO

COORDINATOR: PROF. DANIELE RICCIO

XXXIV CICLO

**SCUOLA POLITECNICA E DELLE SCIENZE DI BASE
DIPARTIMENTO DI INGEGNERIA ELETTRICA E TECNOLOGIE DELL'INFORMAZIONE**

Abstract

The space environment around planet Earth comprises a variety of nonhomogeneous and nonstationary fluxes of natural and man-made junk. Such debris may collide at hyper-velocity with strategic orbital infrastructure, thus jeopardizing the space economy. For this reason, the European Space Agency (ESA) sustains a strategy to acquire a “*..capability to watch for objects and natural phenomena that could harm satellites in orbit.*” Accordingly, large ground-based radars and optical telescopes allow monitoring debris populations with an average size larger than, say 10 cm, up to Low Earth Orbit (LEO) and Geostationary Orbit (GEO), respectively. In fact, these assets form fence coverage areas along with a grueling data fusion for orbit estimation while coping with limits related to temporal and spatial observation constraints, atmospheric hindrances, and detection performance (especially with respect to small-size targets). Interestingly, an active space-based debris detection and tracking capability in the microwave region could complement current surveillance assets for an improved Space Situational Awareness (SSA) and, more dauntingly, provide future spacecraft with an early warning capability for direct collision-avoidance maneuvering. Within this framework, the Technology Readiness Level (TRL) of several key enabling technologies in both digital and Radio Frequency (RF) domains, as well as advances in Active Electronically Scanned Array (AESA) antennas, allow contriving imposing onboard processing tasks for bespoke SSA operations and services. Indeed, this Ph.D. work is structured as a *Gedankenexperiment* to augment SSA by delving into a novel SpaceBorne Radar (SBR) concept inspired by modern and legacy airborne radars.

In particular, such an SBR operates as a fully-polarimetric active instrument in the K_a -band to detect and track small-size debris, entailing a scalable Field of View (FoV) which depends on the available transmit peak power (on the order of kilowatts), multichannel diversity, and AESA steering capabilities. This research avenue highlights the benefit of adopting a cognitive-based SBR for future SSA in terms of improved debris orbit determination and time series analysis on Radar Cross Section (RCS) signatures. Moreover, it poses new questions in radar-theory while endorsing further research and development on key space-qualified enabling technologies. Last but not least, an SBR for SSA may support Space Domain Awareness (SDA), thus cueing a potential liaison with the Homeland Protection (HP), since a debris characterized by a low-RCS is “similar” to a stealth hyper-velocity High Value Target (HVT).

The dissertation is organized into five chapters and one appendix as follows:

Chapter 1 introduces an ontology for SSA from an SBR perspective. In particular, it outlines an holistic description for possible environmental scenarios that an SBR may have to cope with. The focus of such an ontology is related to the modeling of both channel and target phenomenology as well as target motion models. This, in turn, paves the way for reasonable mathematical formulations and architectural paradigms to frame radar detection and tracking techniques.

Chapter 2 presents the concept of a novel monopulse-based SBR transceiver for near-Earth SSA based on a fully-polarimetric Single Input Multiple Output (SIMO) configuration. The sensor complex data hyper-cube structure and timing hierarchies in surveillance mode are addressed along with a Low Pulse Repetition Frequency (Low-PRF) Range and Range-Rate

Search (RRRS) with a Pause While Scan (PWS) contacts collection strategy. The AESA-based radar sensor in the K_a -band is further clarified in order to cope with the significant Doppler stress characterizing a burst of echoes from hyper-velocity debris. Before feeding the onboard Bayesian tracker, the complex data hyper-cube is processed by means of a Doppler filter bank including Pulse Compression (PC) in cascade with a Constant False Alarm Rate-like (CFAR-like) block.

Chapter 3 analyzes the effects of plasma turbulence on the detection performance of SBRs for SSA. Physical insights on both channel and target phenomenology lead to reasonable statistical models with a focus on the Fading Occurrence Probability (FOP) in case of weak scintillation. Consequently, the performance analysis of conventional radar detectors in Additive White Gaussian Noise (AWGN) is provided in a monostatic configuration for either Rayleigh or Rice fluctuating targets, and considering Rice plasma scintillation as a function of the scintillation index s_4 . Numerical results identify a paramount framework to characterize the influence of plasma turbulence on SBR detection performance for SSA. Finally, ancillary notes make provision for tailoring the performance analysis also in the case of bistatic radar configurations.

Chapter 4 extends the complexity of the SBR payload in the K_a -band based on a Code Division Multiplexing (CDM) Multiple Input Multiple Output (MIMO) configuration. Considering small-size hyper-velocity debris, the functional architecture of the fully-polarimetric transceiver is described including key comparisons with the SIMO configuration. SBR operations are clarified via timing hierarchies in surveillance mode, the complex data hyper-cube structure, and the Low-PRF RRRS entailing a Track While Simultaneous Search (TWSS) contacts collection strategy. Ancillary details on the SBR

functional architecture yield paramount insights to ponder critical MIMO aspects and pave the way for key research and development efforts. Moreover, numerical results bring forth a proof of concept for the signal processor upstream the CFAR-like detection block.

Chapter 5 frames the conclusions of the thesis, cueing cognitive-based Bayesian Multi Target Tracking (MTT) as the reference paradigm downstream the CFAR-like detection block. Also, the chapter summarizes the findings of the Ph.D. work and stresses further lines of research in terms of both system engineering aspects and modern radar detection theory. Finally, it makes provision for harmonizing the SBR payload with the futuristic onboard-based debris avoidance system concept proposed by Robert Briskman.

Appendix A provides proof of analytic solutions to structured integrals expressed as the Laplace transform of the product of Marcum Q and power functions.

Conference Articles Related to the Thesis

1. M. Maffei, A. Aubry, A. D. Maio and A. Farina, "On the Exploitability of the Ka Band for Spaceborne Radar Debris Detection and Tracking Measurements," 2019 IEEE 5th International Workshop on Metrology for AeroSpace (MetroAeroSpace), 2019, pp. 355-360.
2. M. Maffei, A. Aubry, A. De Maio and A. Farina, "Spaceborne Radar Functional Architecture for Debris Bayesian Inference," 2020 IEEE 7th International Workshop on Metrology for AeroSpace (MetroAeroSpace), 2020, pp. 1-6.
3. A. De Maio, M. Maffei, A. Aubry and A. Farina, "Fading Occurrence Probability for Spaceborne Radar in Weak Plasma Scintillation," 2021 IEEE 8th International Workshop on Metrology for AeroSpace (MetroAeroSpace), 2021, pp. 193-198.

Journal Articles Related to the Thesis

1. M. Maffei, A. Aubry, A. De Maio and A. Farina, "An Ontology for Spaceborne Radar Debris Detection and Tracking: Channel-Target Phenomenology and Motion Models," in IEEE Aerospace and Electronic Systems Magazine, vol. 36, no. 6, pp. 18-42, 1 June 2021.
2. M. Maffei, A. Aubry, A. De Maio and A. Farina, "Spaceborne Radar Sensor Architecture for Debris Detection and Tracking," in IEEE Transactions on Geoscience and Remote Sensing, vol. 59, no. 8, pp. 6621-6636, Aug. 2021.

3. A. De Maio, M. Maffei, A. Aubry and A. Farina, "Effects of Plasma Media With Weak Scintillation on the Detection Performance of Spaceborne Radars," in *IEEE Transactions on Geoscience and Remote Sensing*, vol. 60, pp. 1-13, 2022.
4. M. Maffei, A. Aubry, A. De Maio, A. Farina, "MIMO SBR via Code Division Multiplexing for Track While Simultaneous Search," in *IEEE Transactions on Geoscience and Remote Sensing*, 2022 (DOI: 10.1109/TGRS.2022.3152350).

Book Chapters Related to the Thesis

1. M. Maffei, A. Aubry, A. De Maio, A. Farina, "Fully Polarimetric Monopulse SBR for Space Situational Awareness," book chapter to appear in "Polarimetric Radar Signal Processing," ed. by A. Aubry, A. De Maio, A. Farina, IET, 2022.

Awards Related to the Thesis

1. Finalist 3 Minute Thesis (3MT) Contest - 2020 IEEE Radar Conference. [Online]. Available: <https://www.radarconf20.org/3-minute-thesis>
2. Best Conference Paper Runner Up - Special Session "Metrology for Radar Systems" - A. De Maio, M. Maffei, A. Aubry, A. Farina, "Fading Occurrence Probabilities for Spaceborne Radar in Weak Plasma Scintillation," 2021 IEEE 8th International Workshop on Metrology for AeroSpace (MetroAeroSpace).

Acknowledgements

There is a frame hanging on the walls of the MIT Stata Center in Cambridge, MA, which holds a quote by Nelson Y. S. Kiang: *What struck me in the beginning was that this building really had the right people in the right slot. That's what made it all go. People were always looking outward, beyond the immediate scope of their research; they were always thinking, "Where can we take this?"* This is exactly my mindset. To this end, my Ph.D. work at the University of Napoli Federico II has been a wonderful experience embracing the cultural tradition entrenched in Naples in 1224 A.D. by the magnificent Emperor Friedrich II. von Hohenstaufen. The tireless endeavor for this Ph.D. represents both a pedagogic journey for personal growth and a successful intertwinement between industry and academia. I would like to express my profound gratitude to my honorary-advisor Alfonso Farina for his outstanding humanity, radar knowledge, wisdom, and mentorship. I hug my brilliant advisor Antonio De Maio and co-advisor Augusto Aubry not only for their extreme competence, devotion to excellence, and intellectual acumen, but also for their friendship. I thank the two bright professors who acted as reviewers and provided me with valuable suggestions to improve this thesis: Alessio Balleri from Cranfield University, Shrivenham, UK, and Stefano Marano from the University of Salerno, Fisciano (SA), Italy. Many thanks to those friends of mine who always encouraged me: James Massey (RIP Master Jim), Fernando Marchetti, Antonio Bauleo, Andrea Fiaschetti, Nabil Elgabalawi, Tiziano Costa.

I dedicate this dissertation to my family.

Rome/Naples, March 8, 2022



From left to right:
Marco, Alfonso, Augusto, Antonio.

Author biography



Marco Maffei (Senior Member, IEEE) was educated at the Jesuit collegium *Istituto M. Massimo*, Rome, Italy, from the age of 5 until 18. He received the Dr. Ing. degree in electrical engineering from the *University of Roma TRE*, Rome, Italy, in 2004. During high school and graduate school, he attended summer school programs at *Georgetown Preparatory School*, North Bethesda, MD; *Phillips Academy Andover*, Andover, MA; *Yale University*, New Haven, CT; and *Uppsala University*, Uppsala, Sweden. Since 2004, he is a radar engineer and research scientist with Thales Alenia Space, Rome, Italy, where he is responsible for algorithm design, analysis, and simulation with a concentration in real and synthetic aperture radars as well as telemetry, tracking, and command systems. On sabbatical leave, he attended courses on radar and data science in the summer of 2012 and 2013 at *MIT*, Boston, MA, and on radar and electronic warfare in the winter of 2015 and 2019 at *Cranfield University*, Shrivenham, UK. Since 2018, he is also a research affiliate with the *University of Napoli Federico II*, Naples, Italy, pursuing the Ph.D. degree in information technology and electrical engineering. So far, he has been working on both deep space and military programs for ESA, NASA, ASI, Italian MOD, and German MOD, namely, Sicral, Cosmo SkyMed, Juno, BepiColombo, SARah, along with breadboarding activities for advanced spaceborne transceivers. His research interest lies in the fields of radar theory and statistical signal processing.

*né dolcezza di figlio, né la pieta
del vecchio padre, né 'l debito amore
lo qual dovea Penelopé far lieta,*

*vincer potero dentro a me l'ardore
ch'i' ebbi a divenir del mondo esperto,
e de li vizi umani e del valore;*

*ma misi me per l'alto mare aperto
sol con un legno e con quella compagna
picciola da la qual non fui deserto.*

*L'un lito e l'altro vidi infin la Spagna,
fin nel Morrocco, e l'isola d'i Sardi,
e l'altre che quel mare intorno bagna.*

Dante Alighieri
Divina Commedia - Inferno Canto XXVI



*Freude, schöner Götterfunken,
Tochter aus Elysium,
Wir betreten feuertrunken,
Himmlische, dein Heiligtum!*

Johann Christoph Friedrich von Schiller
An die Freude

Table of Contents

Chapter 1	1
An Ontology for SBR Debris Detection and Tracking: Channel-Target Phenomenology and Motion Models.	
Chapter 2	51
SIMO SBR Sensor Architecture for Debris Detection and Tracking.	
Chapter 3	87
Effects of Plasma Media With Weak Scintillation on the Detection Performance of SBRs.	
Chapter 4	119
MIMO SBR via Code Division Multiplexing for Track While Simultaneous Search.	
Chapter 5	153
Conclusions Towards Cognitive-Based Bayesian Multi Target Tracking.	
Appendix A	171
Analytic Solutions to Structured Integrals Expressed as the Laplace Transform of the Product of Marcum Q and Power Functions.	
References	177

Chapter 1

An Ontology for SBR Debris Detection and Tracking: Channel-Target Phenomenology and Motion Models

The environment around planet Earth comprises nonhomogeneous and nonstationary fluxes of natural and man-made junk¹ (often referred to as “debris”) entailing possible collision threats to strategic assets in space (e.g., orbital infrastructure, spacecraft, and satellites) [1,2].

In this scenario, governments, armed forces, and space agencies have set up Space Situational Awareness (SSA) programs aimed at monitoring and planning reaction capabilities for the protection of critical infrastructure in space. Such

¹ It is worth noting that the “space debris” term, also known as “orbital debris,” has been defined by the Inter Agency Space Debris Coordination Committee (IADC) as “...all man-made objects including fragments and elements thereof, in Earth orbit or re-entering the atmosphere, that are non functional” [3]. In fact, the IADC definition does not include natural (i.e., nonman-made) meteoroids, whose size can oftentimes be negligible. For the sake of clarification, both man-made and natural space junk could be properly, and more generally, referred to as “Meteoroid and Orbital Debris” (MOD). However, in order to adopt common acronyms and terminology within the aerospace community, both man-made and natural space junk can also be jointly referred to using the “MicroMeteoroid and Orbital Debris” (MMOD) term [3].

operations are entrenched in difficulties in terms of gauging capability and orbital trajectory prediction. The former is related to current constraints of measurement systems, whereas the latter is due to uncertainties caused by gradients affecting debris dynamics, chiefly during long observation campaigns [4]. Within this framework, current data fusion systems for SSA are fed with different types of data, oftentimes measured by large Ground-Based Radars (GBRs) (in addition to ground-based and in-situ optical instruments), namely, in the very high frequency (VHF) band [5,6], ultrahigh-frequency (UHF) band [5,6], *L*-band [5–8], *S*-band [9], *C*-band [8], *X*-band [5,10], *K_u*-band [5,10], as well as novel measurements up to the *W*-band [11]. Accordingly, conventional SSA operations are based on forming fence coverage areas, which allow collecting detection contacts when trespassed by a debris. In particular, this occurs by monitoring large warped volumes of space relying on either beam park or scanning modes (along with additional experimental modes [7]). Moreover, for such monitoring, there is an operative tradeoff between available transmit peak-power and carrier frequency of the radar asset. In other words, the larger the transmit peak-power, the lower the transmit carrier frequency availability in terms of Technology Readiness Level (TRL).

Following the foregoing overview on SSA, this chapter highlights limits and constraints of both GBRs and SpaceBorne Radars (SBRs) to support SSA. It appears wise to frame this problem adopting an ontological perspective on the environmental scenario, thus providing a structured representation of concepts and relations thereof. In particular, for radars supporting SSA (either GBRs or SBRs), the goal is to highlight several ideas, categories, and properties, as well as identifying possible connections among these concepts with a focus on channel-target phenomenology and motion models. Interestingly, the analysis of environmental models structured within suitable ontologies [12] can be a useful source of hints on

suitable inference schemes for debris detection and tracking from a radar perspective. On the other side, these cues may also support a more confident exploitation of radar assets by aerospace communities to nurture and validate catalogs of debris populations. Finally, such a reasoning provides a set of boundary conditions for framing the architectural design of a novel archetype of SBR to support SSA.

The remainder of this chapter is structured as follows. Section 1.1 introduces the environmental scenario with an overview of debris-class populations currently cataloged by aerospace communities. Section 1.2 describes the methodologies adopted by aerospace communities for validating such catalogs with relevant comments on inferences from a radar perspective. Section 1.3 addresses the channel phenomenology where the spatial medium is possibly affected by space weather with an influence on electromagnetic propagation. Section 1.4 reviews the target phenomenology with a focus on the expected scattering behavior of debris. Section 1.5 discusses reasonable translational and rotational motion models of debris. Finally, Section 1.6 outlines the leitmotiv question and keystones for space-based SSA proposed in this Ph.D. work.

1.1 Debris-Class Populations

Considering the volume of space around the Earth, the cardinality of debris with an average diameter larger than $1\ \mu\text{m}$ is estimated to exceed several hundred trillions of items. Yet, when the average diameter is larger than $1\ \text{mm}$, the debris population size shrinks to roughly several hundred millions of items. Nevertheless, when the average diameter is larger than $1\ \text{cm}$, the debris population reaches several hundred thousands of items. If the focus is on debris larger than $10\ \text{cm}$, the debris population count reduces to tens of thousands of objects (see [5] and [13]).

From such a huge population cardinality, it appears useful to identify debris-related taxonomies. Thorough categorizations of debris populations appear in [1], labeled by either the lack or abundance of knowledge to “*associate the root cause of the debris to a launch event.*” Unidentified objects represent the former class, whereas the latter class is further structured into several features and origin. Namely, payloads, e.g., satellites instruments; payload mission related objects, e.g., astronaut tools; payload fragmentation debris, e.g., items fragmented or released during a specific event; payload debris, e.g., items fragmented or released during an unknown event; rocket body, e.g., released orbital stages belonging to a launcher; rocket mission related objects, e.g., shrouds and engines; rocket fragmentation debris, e.g., objects created in case of a launch vehicle explosion; and rocket debris, e.g., objects created from a rocket body during an unknown event. Moreover, a plethora of fragmentation events are also pinpointed as metadata related to the break-up cause such as: accidental, aerodynamics, anomalous, collision, deliberate, electrical, propulsion, and unknown. Items are also grouped into two major populations: a *large-object population* whose debris size is roughly larger than 1 cm, and a *small-object population* whose debris size is roughly larger than 1 mm, yet smaller than 1 cm. For example, micrometeoroids, solid rocket motor dust, paint flakes, and ejecta belong to the small-object population. Multilayer insulation materials as well as launch and mission related objects including the items tracked in the two-line element set of orbital items (publicly shared by the United States Air Force Space Command) belong to the large object population. Basically, explosion and collision fragments, sodium–potassium droplets, and solid rocket motor slag belong to both classes. So far, such taxonomies have been wisely organized by aerospace communities and can, in turn, highlight operative target scenarios needed for proper radar detection and tracking. For example, Fig. 1.1 shows a pictorial representation of an operative scenario from

an SBR (the red point) perspective made of individual debris targets (the yellow chunks) belonging to the large-object population and a debris cloud (the purple chunks) from the small-object population, possibly coexisting in the Field-of-View (FoV) volume (the red dashed lines).

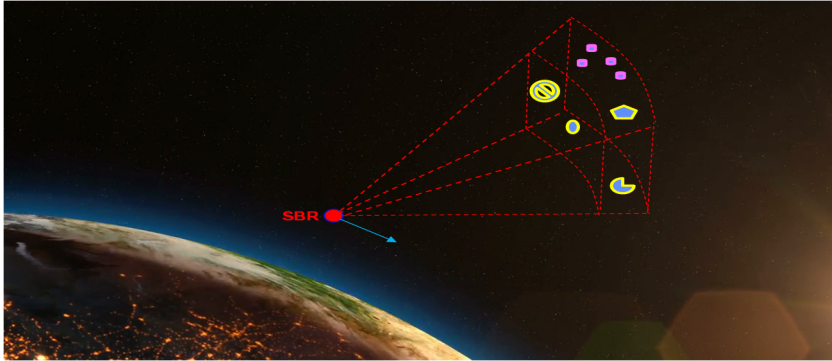


Fig. 1.1. Pictorial view of a SBR (red point) whose FoV (red dashed lines) comprises elements of a *large object population* (yellow chunks) and a *small object population* (purple chunks).

In addition, another important aspect analyzed by aerospace communities (which may further circumscribe the expected operative scenarios for proper radar detection and tracking) is related to the volume distribution of debris populations. Indeed, the identification of specific regions and subregions in space as a Volume of Interest (VoI) allow optimizing the design of the required Field of Regard (FoR) as well as operative modes and functionalities of radars. In particular, several coarse orbital regions filled with debris populations are defined with respect to the Earth's surface [5]. That is, the low Earth orbit (LEO) comprises the highest volume-density of items moving with significant angular velocities along different inclinations; the lower medium Earth orbit (Lower MEO) houses a limited number of items with no specific inclination; the MEO encompasses a limited number of items along specific inclinations; and the

geostationary orbit (GEO) accounts for a limited number of items moving at reduced angular velocities along specific inclinations. For the sake of completeness, the LEO, MEO, and GEO regions are further partitioned into the following subregions [1] identified by the semimajor axis a_a , eccentricity e_e , inclination i_i , perigee height h_p , and apogee height h_a :

- GEO: Geostationary orbit ($i_i < 25^\circ$, $35\,586 \text{ km} < h_p < 35\,986 \text{ km}$, $35\,586 \text{ km} < h_a < 35\,986 \text{ km}$).
- IGO: Inclined geosynchronous orbit ($37\,948 \text{ km} < a_a < 46\,380 \text{ km}$, $e_e < 0.25$, $25^\circ < i_i < 180^\circ$).
- EGO: Extended geostationary orbit ($37\,948 \text{ km} < a_a < 46\,380 \text{ km}$, $e_e < 0.25$, $i_i < 25^\circ$).
- NSO: Navigation satellites orbit ($50^\circ < i_i < 70^\circ$, $18\,100 \text{ km} < h_p < 24\,300 \text{ km}$, $18\,100 \text{ km} < h_a < 24\,300 \text{ km}$).
- GTO: GEO transfer orbit ($i_i < 90^\circ$, $h_p < 2\,000 \text{ km}$, $31\,570 \text{ km} < h_a < 40\,002 \text{ km}$).
- MEO: Medium Earth orbit ($2\,000 \text{ km} < h_p < 31\,570 \text{ km}$, $2\,000 \text{ km} < h_a < 31\,570 \text{ km}$).
- GHO : GEO-superGEO crossing orbits ($31\,570 \text{ km} < h_p < 40\,002 \text{ km}$, $40\,002 \text{ km} < h_a$).
- LEO : Low Earth orbit ($h_p < 2\,000 \text{ km}$, $h_a < 2\,000 \text{ km}$).
- HAO: High-altitude Earth orbit ($40\,002 \text{ km} < h_p$, $40\,002 \text{ km} < h_a$).
- MGO: MEO-GEO crossing orbits ($2\,000 \text{ km} < h_p < 31\,570 \text{ km}$, $31\,570 \text{ km} < h_a < 40\,002 \text{ km}$).
- HEO: Highly eccentric Earth orbit ($h_p < 31\,570 \text{ km}$, $40\,002 \text{ km} < h_a$).
- LMO: LEO-MEO crossing orbits ($h_p < 2\,000 \text{ km}$, $2\,000 \text{ km} < h_a < 31\,570 \text{ km}$).
- UFO: UndeFined Orbit.
- ESO: EScape Orbits.

1.2 Validation Methods of Debris Catalogs

So far, the confidence on the knowledge described in Section 1.1 relies on bespoke analytical tools and verification methods developed in the past decades by aerospace communities. Remarkably, by providing relevant comments on these methods from a radar perspective, it is possible to highlight limits and stimulate possible novel paradigms to improve confidence on SSA inferences. Indeed, several tools and models have been introduced by both NASA and ESA to manage MMOD issues. NASA has developed the Orbital Debris Engineering Model and the Meteoroid Engineering Model, whereas ESA has focused on the Meteoroid and Space Debris Terrestrial Environment Reference (MASTER). Primarily, these models have been developed to assess the flux of MMOD imparted on a spacecraft [5]. Nevertheless, these models also cue the spatial density of items in the aforementioned orbital regions with paramount insights on the possible occurrence of multiple targets in the operative scenarios for radar detection and tracking. For instance, Horstmann *et al.* [13] report the volume density of debris within the LEO region (as per the MASTER model) up to the 2018 epoch. The LEO appears as the region with the highest density of objects per cubic kilometer, with peak density at an altitude of 800 km (namely, about 8×10^{-5} items/km³ for debris whose diameter is larger than 1 mm; 3×10^{-6} items/km³ for debris whose diameter is larger than 1 cm; and 2×10^{-7} items/km³ for debris whose diameter is larger than 10 cm). Within this framework, a paramount issue for SSA is to validate the acquired knowledge on debris-class populations. Small object populations knowledge is, de facto, validated only by checking impact data extracted from dents on available hardware returned from space. On the contrary, large-object populations knowledge is validated

by comparing a reference virtual-sensor detection performance, e.g., the Program for Radar and Optical Observation Forecasts by ESA, against real radar or optical measurement campaigns. In the latter case, any incongruency is reflected backward into a suitable modification of the original large-object population model until the virtual-sensor and real-sensor detection performance become aligned [14].

Interestingly, considering the large-object population knowledge, it appears that the debris-size around 1 cm represents a serious challenge for detection since the amount of measurement data is extremely scarce. This, in turn, raises the legitimate question of how accurate the 1-cm debris population is represented by current space debris models. Similar remarks are evident in [15], whereby the histogram of monitored objects at the orbital altitude of the Cosmo SkyMed surveillance satellites (i.e., roughly 620 km) shows a clear gap in the size of undetected objects approximately below 10 cm. In more general terms, one of the most important tasks to support SSA is the confident initialization and maintenance of debris catalogs. For example, the European Union (EU) manages the, so-called, Database and Information System Characterising Objects in Space (DISCOS) [1]. DISCOS servers are located at the ESA European Space Operations Centre (ESOC) premises in Darmstadt, Germany, under the wing of the Space Debris Office. DISCOS collects structured data and metadata for several tens of thousands of trackable items [5,6,13]. In general, catalog initialization requires a new item to be detectable by one or more sensors for a time span and spatial extent necessary to enable an accurate orbit determination. At last, catalog maintenance requires items to be reobservable for track association.

Consequently, it appears worth pondering the detection and parameter estimation capabilities of current assets for SSA. For the most part, ground-based active radars have been tailored to observe the LEO region. On the contrary, passive optical

systems have been exploited to monitor objects at further distances up to the GEO region. Representative GBRs in the USA comprise the Midland Space Radar (MSR) in the *UHF*-band; the Poker Flat Incoherent Scatter Radar (PFISR) in the *UHF*-band; the Cobra Dane radar in the *L*-band; the Goldstone Solar System Radar (GSSR) in the *X*-band; the Haystack Ultrawideband Satellite Imaging Radar (HUSIR) also known as the Haystack Radar in the *X*-band; the Haystack Auxiliary Radar (HAX) in the K_u -band; as well as the Space Fence on the Kwajalein Atoll in the *S*-band. Facilities in the EU include the EISCAT radars in both the *VHF*-band and the *UHF*-band; the European Grand Réseau Adapte a la Veille Spatiale (GRAVES) in the *VHF*-band; the Ballistic Missile Early Warning System (BMEWS) at Fylingdales, U.K., in the *UHF*-band; the BiStatic Radar for Leo Survey (BIRALES) in the *UHF*-band; the Tracking and Imaging Radar (TIRA) in both the *L*-band and the K_u -band; and the novel German Experimental Space Surveillance and Tracking Radar (GESTRA) in the *L*-band. Furthermore, the southern hemisphere also contributes to SSA, e.g., via the Kiwi Space Radar (KSR) in New Zealand in the *S*-band. Similarly, representative assets for ground-based optical telescopes include the Michigan Orbital Debris Survey Telescope (MODEST); the Télescope à Action Rapide pour les Objets Transitoires (TAROT); the ESA Space Debris Telescope; the ZIMLAT telescope; or the British National Space Centre (BNSC) Starbrook telescope. In general, (active) GBRs in the microwave region are significantly less dependent on clear atmospheric conditions and can illuminate the environment via their own transmission. Unfortunately, the detection performance of GBRs (even with state-of-the-art transmit power capabilities) decreases beyond the LEO region. On the contrary, (passive) optical telescopes are able to monitor orbital regions beyond the LEO region, albeit requiring clear-atmospheric conditions and an indirect (i.e., external) illumination source such as the sun.

Now, for the sake of clarification on current monitoring paradigms for SSA, let us consider a scenario under surveillance, whereby the orbits of debris populations are assumed unknown. In order to specify the detection performance of GBRs, Krag and Klinkrad [16] define first a measurable VoI. In particular, the VoI center is cued by a triplet made of range r (with extension Δr in the radial direction), elevation angle θ (with extension $\Delta\theta$ along the elevation arc), and azimuth angle φ (with extension $\Delta\varphi$ along the azimuthal arc), in a general spherical coordinates frame centered at the radar itself. When such a VoI is crossed by a debris or a debris swarm, the result is a so-called *cell passage event* which, in principle, can or cannot be detected. In other words, the detection contact depends on the specific capabilities of the radar asset. Within this context, one may take heed of statements about GBRs sensitivities adopted within the aerospace community [16]. In these cases, the detection performance is defined in terms of a *cell passage event* at a maximum range at which a spherical object with a minimum size associated to a minimum Radar Cross Section (RCS) σ_{RCS} can still be confidently detected. As can be seen from the work in [17], a wide range of RCS (between -70 dBsm up to 20 dBsm) is taken into account for framing detection capabilities. In [5], -48 dBsm is reported, for instance, as the minimum RCS detectable by the TIRA asset for a target in the L -band at a 1 000-km range corresponding to an equivalent metallic sphere with a diameter of 2 cm. In line with the same reasoning, Krag and Klinkrad [16] report a minimum RCS threshold of - 20 dBsm corresponding to an equivalent sphere with a diameter of 11.28 cm at a 50-cm wavelength, which is the legacy gauging limit of the U.S. Space Surveillance Network catalog. Such detection statements abide by a general beam-park mode that counts items passing through the radar instantaneous FoV during an observation campaign. To a large extent, these campaigns are based on processing the received echo complex envelopes through a bank of filters, and comparing their squared outputs to

thresholds after a noncoherent integration. Albeit aimed at estimating (whenever possible) the debris range, range-rate, and RCS, the gauging configuration and the available elapse time for data acquisition from a single ground-based asset in beam-park mode do not allow for an immediate estimation of the orbital trajectory of a detected item. In principle, replacing beam-park modes with more advanced surveillance scanning modes, e.g., based on the steering capabilities of an active electronically scanned array (AESA), may allow for orbit determinations from a single radar site. Yet, this could occur (as it will be clarified later on in this chapter) only if multiple observations of the same object along an orbital arc were to be collected and grouped together even in a densely populated scenario.

Additional paramount comments for either GBRs or SBRs inference capabilities follow. DISCOS includes, wherever possible, the characteristic length of a cataloged item defined either as its average or its largest dimension along three orthogonal axes. When these dimensions are completely unknown, the characteristic length is derived only indirectly from an estimated RCS, assuming a debris with a perfectly conducting spherical shape for the size-estimation model (SEM) [16]. Yet, several uncertainties may arise from an “SEM cued by an RCS-estimate”. Indeed, biasing fluctuations may occur due to unknown scattering [18] and propagation [19] mechanisms with respect to the operative wavelength. For example, nuisances are related to possible target scattering fluctuations, Antenna Radiation Pattern (ARP) straddling losses, as well as scintillation of the media due to space weather effects [20]. In addition, possible Faraday rotations and target depolarization effects have induced state-of-the-art GBRs architectures [7,9] to rely on polarization diversity in order to collect echoes on two orthogonal channels. In summary, both propagation and scattering effects may prevent radars (either GBRs or SBRs) from confidently estimating an RCS and, therefore, the characteristic length of an

item via a specific SEM. Apparently, these notes may appear negligible for RCS estimations of debris with a large size. Yet, they become of paramount importance when the debris size is small and a low RCS value must be accurately estimated.

On the basis of these difficulties in SSA, as it will be clarified during the rest of this chapter, SBRs represent a complementary aid to GBRs to support the initialization and maintenance of debris catalogs, such as DISCOS. A key architectural paradigm relies on considering an SBR in the K_a -band with a transmit peak power of the order of kilowatts [2]. Compared to the larger FoR spanned by state-of-the-art GBRs with a transmit peak power of the order of megawatts, the detection and tracking capability from an orbiting SBR would be clearly tailored to the surveillance of a smaller and less warped FoR resembling a solid torus around planet Earth. In this case, the larger the SBR transmit peak power and ARP agility the larger the solid torus and, therefore, the fewer the SBRs needed (e.g., displaced in inclination with respect to the Earth's equator) in a constellation aimed at monitoring a specific VoI.

1.3 Channel Phenomenology

The channel phenomenology for SSA discussed in this section addresses signal propagation through either free space or plasma slabs with reasonable assumptions on channel behaviors and related effects on signal waveforms.

1.3.1 Signal Propagation in Free Space and Plasma Slabs

The propagation of electromagnetic signals for SSA can be perturbed by space weather originating within the solar system (see Fig. 1.2). In [20], several notes report useful indications for

framing the channel phenomenology for either GBRs or SBRs. In particular, Table 1.1 indicates the main space regions affected by space weather in relation to orbits. Moreover, ECSS [20] highlights the ionospheric density profile of electrons in space whereby the highest electron density lies at a geodetic altitude between 300 and 600 km and gradually decreases outside this range even in case of an approaching geomagnetic storm (as indicated by the $5-K_p$ index in [21], which characterizes the magnitude of geomagnetic activity as a minor storm). Thus, the LEO not only appears as the space region with the highest density of debris per cubic kilometer, but also as the one with the highest electron density profile (for the most part at a geodetic altitude of roughly 400 km, with peaks over one million electrons per cubic centimeter at noon).

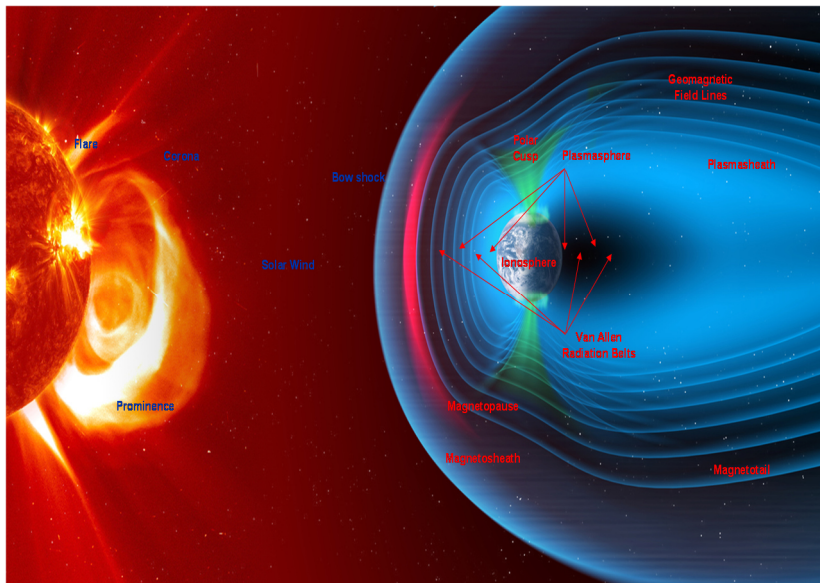


Fig. 1.2. Pictorial view of the Sun (left) and the Earth (right) affected by space weather.

Orbit	Space Region affected by Space Weather
LEO Low Inclination	Ionosphere
LEO High Inclination	Ionosphere, Auroral Zone
GEO	Outer Magnetosphere, Plasmasphere, Magnetosheath
MEO	Outer Magnetosphere, Plasmasphere, Magnetosheath
GTO	Outer Magnetosphere, Plasmasphere, Ionosphere
High Apogee Elliptical Orbit	All Regions
L1, L4, L5 Lagrangian Points	Solar Wind
L2	Solar Wind, Magnetotail, Magnetosheath
Interplanetary Cruise	Solar Wind
Planetary Orbit	Planetary Environment

Table 1.1. Orbits associated with regions affected by space weather [20].

The channel phenomenology on radar signals can be analyzed solely by an electromagnetic perspective (in other words, it is reasonable to neglect the effects of gravitational fields, which introduce refraction on radio waves [22]). In particular, depending on the carrier wavelength and solar activity, a microwave radar (either an SBR or GBR) may have to take into account propagation through free space vacuum and through slabs of turbulent plasma. The former condition is the nominal operative condition of propagation within linear homogeneous and isotropic media as described by the classical Helmholtz equation [23]. The latter condition implies nonstationary and nonhomogeneous physical media (to be referred to as random media) where the dielectric constant is a random variable (r.v.),

the refraction index may fluctuate, and the Helmholtz equation is stochastic [24]. In simple terms, a plasma medium is a gas of charged particles where the particles do not interact through collisions as per a neutral gas, but rather via electromagnetic forces. The presence of external electromagnetic fields can thus influence the motion of these charged particles, whereas the motion of charged particles can, in turn, generate currents and, therefore, electromagnetic fields. From this perspective, a valid description of plasma is that of a fluid slab of turbulent media made of two particle species (i.e., a so-called 2-component plasma [25] comprising electrons and ions) and assuming the oversimplified approximation of rarefaction and thermodynamic equilibrium. In this case, being the mass of the electrons much smaller than that of the ions, the dynamic response of the electrons becomes predominant with respect to the motion of ions. Consequently, it appears worth pondering following two questions.

- When should a radar (either SBR or GBR) consider signal propagation through slabs of turbulent plasma?
- What kind of effects can occur on signals propagating through slabs of turbulent plasma?

To this end, let us represent in Fig. 3 a possible operative scenario in which an orbiting monostatic SBR (i.e., the red point) transmits a burst of waveforms propagating in both free space (i.e., the dark region) and plasma (i.e., the green slab filled with electrons) toward a debris cloud (i.e., the purple chunks) whereas part of the energy is backscattered from the debris cloud toward the SBR (thus propagating once again in both free space and plasma). Accordingly, the answer to the first question relies on the spatial and temporal extent of the total electron content (TEC) in the medium [24], as this indicates whether propagation will be

influenced only by free space or also by a plasma slab. The answer to the second question pertains to absorption, refraction, dispersion, carrier offset, Faraday rotation, as well as amplitude and phase scintillation [22].

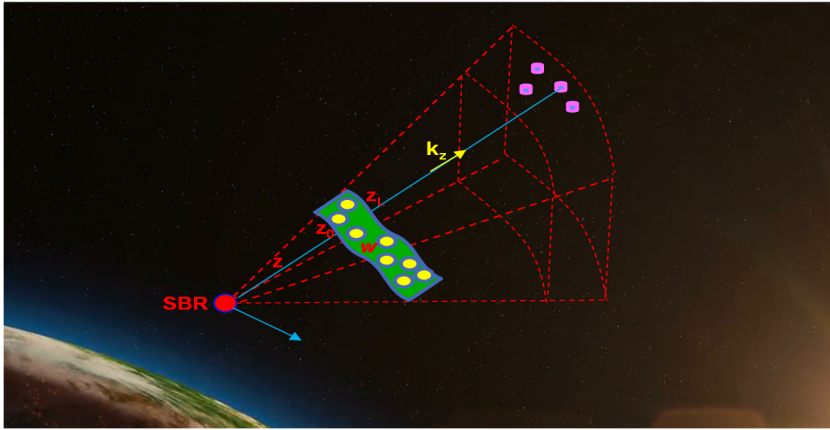


Fig. 1.3. Signal propagation in free space (dark space) and plasma (green slab) towards debris clouds (purple chunks).

These undesired effects may (or may not) be negligible for a radar (either SBR or GBR) aimed at SSA. The first step is to verify the condition of existence of propagation and highlight whether or not absorption can be assumed negligible. For signals propagating through free space vacuum, Maxwell's equations can be elaborated considering the absence of volume charge density or current density. Introducing the signal wavenumber $k = 2\pi/\lambda$ (where λ is the electromagnetic carrier wavelength), the dispersion relation for free space vacuum can be formulated as

$$\omega^2 = c^2 k^2 \quad (1.1)$$

with respect to the radian frequency $\omega = 2\pi f$ where f is the electromagnetic carrier frequency and $c = \lambda f$ is both the phase

and group speed. On the contrary, for signal propagation through slabs of plasma, a significant physical complexity arises. Indeed, plasma supports a plethora of oscillation modes (either as electrostatic or induced electric fields) depending on many boundary conditions and variables, including temperature and the occurrence of a magnetic field. In simple terms, the dispersion relation in a plasma region can be characterized by the frequency of plasma media ω_p , which lies completely within the *HF*-band taking into account the electron density profiles shown in [20]. More specifically, for $\omega < \omega_p$ the dispersion relation entails absorption on signal propagation whereas for $\omega \gg \omega_p$ the dispersion relation for free space vacuum in eq. (1.1) becomes a reasonable approximation also in a plasma region. In other words, radar signals (either GBR or SBR based) may certainly propagate above the *HF*-band not only in free space but also in plasma media. Clearly, GBRs must also take into account possible absorption in specific windows of the electromagnetic spectrum due to signals inevitably crossing neutral atmospheres while SBRs can be deployed on orbits above the troposphere. Yet, it is also well known that the 26.5–40 GHz range of the K_a -band fitting the WR-28 waveguide is a suitable spectral window with minor attenuation due to water vapor and oxygen.

Once the condition of existence of propagation has been faced, the treatment on channel phenomenology through free space vacuum and plasma slabs hinges on the stochastic Helmholtz equation as well as on possible gyrotropics effects. With regards to the Helmholtz equation, it can be shown [24] that a weak or moderate plasma turbulence allows simplifying the propagation model through a plasma slab predominantly as a forward scattering mechanism around a small cone with negligible attenuation and backscattering within the cone itself (thus excluding multiple scattering effects in the plasma slab). This results in a Rytov solution (see [24, eqs. (3.24) and (3.25)])

based on the superposition of contributions for both amplitude and phase of the emerging field out of a plasma slab and represents the keystone for modeling weak scintillations on radar signals as it allows for the applicability of the central limit theorem (CLT). With regards to gyrotropics effects [23] and considering magnetized plasma media, it is well known that the original polarization axes of a general propagating transverse electromagnetic mode (TEM) are rotated by the so-called Faraday rotation angle.

1.3.2 Channel Models

By modeling plasma as a fluid slab made of 2 components (i.e., electrons and ions) [25], the spatial and temporal behavior of the electron content can be analyzed by the electron density n_e at a specific spatial location (x, y, z) at a given instant (t) as per small perturbations (indicated by the “1” subscript) around fixed values (indicated by the “0” subscript), i.e.,

$$n_e(x, y, z, t) = n_0 + n_{e1}(x, y, z, t) \quad (1.2)$$

This, in turn, allows introducing a *normalized electron density* as per the following r.v. $\xi_d \in \mathbb{R}^+$

$$\xi_d(x, y, z, t) = \frac{n_{e1}(x, y, z, t)}{n_0} \quad (1.3)$$

to describe the medium via spectral and statistical properties [24]. For example, assuming Wide Sense Stationarity (WSS), the Wiener-Khinchin theorem represents the Fourier-based relation between the correlation function of the normalized electron density $\Gamma_{\xi_d \xi_d}(x, y, z, t)$ and its spectrum $S_{\xi_d \xi_d}(K_x, K_y, K_z, \omega)$, i.e.,

$$\Gamma_{\xi_d \xi_d}(x, y, z, t) = \mathbb{E}[\xi_d(x' + x, y' + y, z' + z, t' + t)\xi_d(x', y', z', t')] \quad (1.4)$$

$$S_{\xi_d \xi_d}(K_x, K_y, K_z, \omega) = \frac{1}{(2\pi)^4} \int_{x=-\infty}^{x=+\infty} \int_{y=-\infty}^{y=+\infty} \int_{z=-\infty}^{z=+\infty} \int_{t=-\infty}^{t=+\infty} \Gamma_{\xi \xi}(x, y, z, t) \times \exp(-j[K_x x + K_y y + K_z z - \omega t]) dx dy dz dt \quad (1.5)$$

where $\mathbb{E}[\cdot]$ indicates the statistical expectation operator. In principle, from the knowledge of the spectral structure of the irregularities of plasma patches in eq. (1.5), it is possible to characterize the state of the medium and subsequently analyze detrimental effects on propagating signals. As a simpler alternative paradigm, it is possible to consider experimental scintillation parameters [22] such as the scintillation index

$$s_4(\lambda) = \sqrt{\frac{\mathbb{E}[I(\lambda)^2] - \mathbb{E}[I(\lambda)]^2}{\mathbb{E}[I(\lambda)]^2}} \quad (1.6)$$

as a function of the intensity I of the electric field \vec{E} at a specific wavelength λ in a given location and temporal window (i.e., $I(\lambda) = |\vec{E}(\lambda)|^2$ where $|\cdot|$ is the modulus operator). In addition to s_4 (the wavelength dependence on s_4 has been omitted for simplicity, i.e., $s_4(\lambda) = s_4$), an additional description of the medium may derive from the *scattering function* of the channel which defines the coherence-time Δt_{coh} and coherence-bandwidth Δf_{coh} for propagation through a WSS channel (characterized by an *uncorrelated scattering* constraint [26,27]). Accordingly, the coherence-time Δt_{coh} and coherence-bandwidth Δf_{coh} of the channel can be useful parameters to frame detection schemes. Indeed, the former frames the temporal elapse of possible coherent and noncoherent combining, whereas the latter highlights frequency selectivity. For example, considering propagation in the K_a -band, Feria *et al.* [28] reports a Δt_{coh} of

3.72 ms during experimental campaigns affected by solar scintillation (as per a JPL internal memo from Armstrong and Woo in 1981). More recently, Morabito [29] shows results from Cassini solar conjunctions where Δt_{coh} spans from roughly 40 to 200 ms. Hopefully, the novel BepiColombo mission to Mercury (equipped with state of the art onboard microwave instruments in the K_a -band [30]) will provide additional indications of Δt_{coh} . As of today, the paucity of available data allows framing Δt_{coh} on the order of ms. Consequently, the channel in the K_a -band can be modeled as flat-in-time during an operative radar burst elapse of a few ms. On the other side, to the author’s best knowledge no assessment or experimental evidence has been found on the coherence-bandwidth Δf_{coh} of such a channel in the K_a -band. A conjecture considers the extent of Δf_{coh} as a decreasing function of the scintillation index s_4 (i.e., the larger s_4 , the smaller Δf_{coh}). In pragmatic terms, for radar detection in the K_a -band a frequency nonselective channel (i.e., flat-in-frequency) is also a valid assumption for “small” bandwidths of the radar signal (e.g., up to a few megahertz) and “weak” plasma turbulence (e.g., $s_4 \leq 0.5$). In summary, in case of mild or moderate plasma turbulence (in the absence of experimental data) it is reasonable to assume a flat-flat channel on small bandwidths during a short radar burst elapse, thus resulting in a fixed multiplicative complex term affecting the complex envelope of the radar signal.

Alongside the flat-flat assumption on the channel for short radar bursts on limited bandwidths, statistical models allow representing fluctuating effects of plasma media on radar signals. Favorable models are supposed to be intertwined to physical descriptions, mathematical tractability, and compatibility with experimental results. This, in turn, entails delving into first order (and higher order) amplitude and phase statistics. For instance, Yeh and Liu [24] outline a number of statistical models starting from first-order statistics of the signal envelope distribution such as the log-normal, Rice, and Nakagami- m . Nevertheless, praised

statistical models are those relying on proxy parameters to be directly measured in-situ and uploaded to an operative radar. Indeed, the possibility to exploit parameter estimates represents a Knowledge Aided (KA) paradigm which may set up the radar configuration for more robust, selective, or efficient debris detection and tracking schemes. For example, the scintillation index s_4 in eq. (1.6) (i.e., the ratio of the standard deviation of the received signal power to its mean at a specific wavelength) is a useful telemetry [21] to swap the channel model between an *Additive White Gaussian Noise (AWGN) channel* and a *scintillating channel* (see Table 1.2).

	Channel Phenomenology	
s_4	$s_4 < 0.1$	$0.1 \leq s_4 \leq 0.5$
Mechanical Perspective	free space vacuum	slabs of weakly turbulent plasma
Electromagnetic Perspective	isotropic linear homogeneous media	random media
Signal Perspective	AWGN channel	scintillating channel

Table 1.2. Channel models relying on the scintillation index s_4 .

For such a scintillating channel, let us consider in weak plasma turbulence the occurrence of forward scattering mechanisms within a slab as a one-way propagation along a set of, say L , nonresolvable paths during a radar burst elapse time (see [28]). Accordingly, one may then elaborate the aforementioned multiplicative complex scintillation process at a given time t as per the following r.v.

$$B e^{j\phi} = b_0 e^{j\phi_0} + \sum_{k=1}^{L-1} B_k e^{j\phi_k} = b_0 e^{j\phi_0} + B_R e^{j\phi_R} \quad (1.7)$$

and assume that $b_0 \in \mathbb{R}^+$ and $\phi_0 \in (-\pi, \pi]$ are deterministic terms (representing the specular deterministic propagation path)

whereas B_R is a Rayleigh-distributed r.v. with parameter σ_b^2 , and ϕ_R is a uniformly distributed r.v. in $(-\pi, \pi]$ statistically independent of B_R which model the weak-scattering stochastic propagation paths. For such assumptions the probability density function (pdf) of B is Rice [31], i.e.,

$$P_B(b) = \frac{b}{\sigma_b^2} e^{-\left(\frac{b^2+b_0^2}{2\sigma_b^2}\right)} I_0\left(\frac{b_0 b}{\sigma_b^2}\right) u(b) \quad (1.8)$$

where $I_n(b)$ is the modified Bessel function of the first kind and n -th order, and $u(b)$ is the Heaviside unit step function. In this case, the Rice factor $r = b_0^2/2\sigma_b^2$ is the ratio of the specular dominant power (i.e., the power of the main propagation path contribution, b_0^2) and the random power (i.e., the power of the remaining nonresolvable multipath contributions due to weak-scattering, $2\sigma_b^2$). Interestingly, the assumption on ϕ_0 as a deterministic parameter frames B and ϕ as statistically dependent. Yet, by enforcing randomness also on ϕ_0 as a uniformly distributed r.v. in $(-\pi, \pi]$ and statistically independent of B_R and ϕ_R , B and ϕ become statistically independent, with ϕ a uniformly distributed r.v. in $(-\pi, \pi]$, and the pdf of B is Rice as per eq. (1.8). For the sake of completeness, the Rice assumption for electromagnetic propagation with weak plasma scintillation appears also on works related to one-way telemetry data links [28], Radio Science Experiments (RSE) related to solar-scintillation measurements [29], and Global Navigation Satellite Systems (GNSS) [32].

In addition, by constraining the average power of a signal propagating under scintillation to remain constant as per the forward scattering assumption in the weak scintillation model [24], one may enforce the mean square value of B (for example) as unitary, i.e., the *scale parameter* $\Omega = b_0^2 + 2\sigma_b^2$ is

$$\mathbb{E}[B^2] = \Omega = b_0^2 + 2\sigma_b^2 = 1 \quad (1.9)$$

Remarkably, Feria *et al.* [28] models telemetry scintillations with a Rice distribution in the K_α -band along with the benefit of being specified in terms of the scintillation index s_4 [28,33]. Indeed (see also [34]), for one-way propagation a direct relationship between the scintillation index s_4 and the Rice pdf in eq. (1.8) with parameters b_0^2 and σ_b^2 can be written as

$$r = \frac{b_0^2}{2\sigma_b^2} = \frac{\sqrt{1-s_4^2}}{1-\sqrt{1-s_4^2}} \quad (1.10)$$

That is, combining eqs. (1.9) and (1.10) in terms of the scintillation index s_4 it is possible to frame a liaison between experimental results from plasma radio-physics and one-way propagation in radar theory for debris detection and tracking, i.e.,

$$b_0^2 = \sqrt{1 - s_4^2} \quad (1.11)$$

$$\sigma_b^2 = \frac{1-\sqrt{1-s_4^2}}{2} \quad (1.12)$$

As a reference, Table 1.3 summarizes the Rician parameters associated to several operative plasma scintillation index values s_4 related to a weak scattering paradigm.

s_4	b_0	σ_b^2
0.1	0.997	0.002
0.2	0.990	0.010
0.3	0.977	0.023
0.4	0.957	0.042
0.5	0.931	0.067

Table 1.3. Scintillation index values s_4 and related Rician parameters.

1.3.3 Degrading Effects on Signals

A review of the degrading effects of plasma on propagation follows for radar signals (either GBR or SBR based), yet with a particular focus on SBRs in the K_a -band. First of all, it is worth stressing that empirical measurements in the K_a -band [33] confirm several effects to be described by the general degradation formula $a_\epsilon f_c^{-b_\epsilon} TEC^{c_\epsilon}$ where the positive constants a_ϵ , b_ϵ , c_ϵ are estimated via regression on experimental data with respect to signals on a carrier frequency f_c . TEC is defined between two reference radial propagation extents z_0 and $z_L > z_0$ (see also Fig. 1.3), i.e.,

$$TEC = \int_{z_0}^{z_L} n_e(x, y, z, t) dz \quad (1.13)$$

such that a TEC Unit (TECU) is defined as 10^{16} electrons/m². For example, a degradation (which is also a key nuisance for RSE on general relativity [30]) is related to the possible refraction of signals due to plasma in terms of an offset angle departing from Line Of Sight (LOS) propagation. Interestingly, Yakovlev [22] highlights that bending from LOS propagation occurs in case vertical gradients of the refractivity are significant. Such a refraction angle is characterized by a f_c^{-2} frequency dependence (i.e., $b_\epsilon = 2$ in the general degradation formula), thus stressing the benefit of adopting the K_a -band for SSA compared to the use of lower bands. As an additional example, the f_c^{-2} frequency dependence for degradation (i.e., $b_\epsilon = 2$ in the general degradation formula) also appears in the Faraday rotation angle as

$$\alpha_{Faraday} = a' |\vec{B}| \cos(\psi) f_c^{-2} TEC \quad (1.14)$$

where a' is a positive constant, \vec{B} is an existing magnetic induction field (e.g., the ubiquitous geomagnetic induction field),

and ψ is the angle between $\vec{\mathbf{B}}$ and the signal wavenumber direction. Once again, $\alpha_{Faraday}$ is definitely more marginal in the K_a -band [18] compared to the use of lower bands. Further examples of degradation include the group time delay distortion due to plasma. Indeed, radar signals are inherently time-based waveforms with the Optical Path Length (OPL) propagation light time (t_{0p}) nominally aimed at cueing the Physical Path Length (PPL) propagation light time (t_{0s}) [22]. While in free space t_{0p} coincides with t_{0s} , plasma media may enlarge t_{0p} , thus biasing the estimation of the desired range by Δt_0 . That is, plasma distorts the time of propagation of light over a physical distance by the amount

$$\Delta t_0 = t_{0p} - t_{0s} = a'' \frac{1}{f_c^2} TEC \quad (1.15)$$

where a'' is a positive constant [22]. Again, the f_c^{-2} frequency dependence (i.e., $b_\epsilon = 2$ in the general degradation formula) shows a more marginal degradation of the (group) time delay bias in the K_a -band compared to the use of lower bands. As a by-product, one may also derive the frequency shift f_{shift} [22] as

$$f_{shift} = f_c - a'' \frac{1}{f_c} \frac{d}{dt} TEC \quad (1.16)$$

In this case, the spectral shift due to plasma is reduced (albeit more marginally) by the f_c^{-1} frequency dependence (i.e., $b_\epsilon = 1$ in the general degradation formula). This shows, in any case, the benefit of adopting higher band (such as the K_a -band) compared to the use of lower bands. It is also worth noting that such a frequency shift appears only in case of a temporal variability of the TEC due to the time derivative operator in eq. (1.16).

1.4 Target Phenomenology

The *large-object population* and the *small-object population* identified by aerospace communities uphold the following target models from a low-resolution radar perspective, respectively.

- Single debris targets characterized as a singleton point-like-based entity.
- Debris cloud targets characterized as a distributed point-process-based entity.

Interestingly, beside detection and tracking schemes for SSA, these target models are also applicable to support time series analysis on RCS signatures using fully polarimetric radars (i.e., quad-pol GBRs or SBRs). In particular, polarimetric-based inferences of debris features (e.g., shape, orientation, dielectric structure, and interpretation of scattering mechanisms) can rely on measurements of the scattering matrix for a single debris and second-order statistics thereof (e.g., the polarimetric coherency matrix, the polarimetric covariance matrix, or the polarimetric Kennaugh matrix [35]) for a debris cloud. Consequently, the target phenomenology for SSA discussed in this section addresses several scattering behaviors of debris as well as important digressions on radar sensitivity and the Doppler effect. Once again, a special attention is paid to SBRs in the K_α -band for small-size targets.

1.4.1 RCS Definitions for Single Debris and Debris Clouds

The origin of a debris is related to harsh spawning events, natural outgassing, erosions, explosions, fragmentations, or hyper-velocity impacts. Consequently, for SSA it is reasonable to make several assumptions on targets features and expected behaviors. That is, a debris is likely a piece of junk with asymmetric shapes, possibly made of a mixture of constituents, along with a reference density roughly between 2.5 g/cm^3 and 3 g/cm^3 as hinted in [20]. Then, let us assume that a radar transmits an electromagnetic waveform impinging on the external surface of a single debris as a general Transverse Electric Mode (TEM) in the Fraunhofer region [18,23]. It is well known that the scattering behaviour can occur in three regions [36] depending on the target physical size L_d to wavelength λ ratio (i.e., L_d/λ):

- A *Rayleigh region* for “small” L_d/λ characterized by a reduced scattered field. In this case, the electric field is instantaneously uniform along the extension L_d of the debris. This induces charge densities on the debris and, therefore, a dipole moment to be framed in terms of electrostatics. Thus, basically the whole physical size and orientation of the debris affects the scattering mechanism, independently of the geometrical shape of the debris.
- A *resonant region* for $L_d/\lambda \cong 1$ characterized by a fluctuating scattered field. In this case, optical scattering is predominant (i.e., scattering in which reflection angles are equal to incident angles) albeit creeping and edge surface waves may marginally arise. Consequently, the scattering from one location of the body is influenced by the collective contributions of induced currents within the rest of the object. Again, the entire physical size of the debris affects the

scattering, although this does depend on its geometrical shape.

- A *high-frequency optical region* for “large” L_d/λ characterized by an unfaltering scattered field. In this case, the scattered field from one location of the object is marginally affected by induced currents on the entire object. Due to such weaker coupling interactions, the objects can thus be modeled resembling a collection of independent scattering centers. The geometrical shape of the object becomes very important and the scattered field from each scattering center depends only on the incident field. In this scenario, specific scattering mechanisms emerge such as specular scattering from each scattering center, multiple bounces, diffractions, and end-region scattering.

Accordingly, the adoption of higher carrier frequencies (e.g., the K_a -band compared to the S -band) enforces small-size debris scattering mechanisms to occur closer to the high frequency optical region with a beneficial stability for repetitive measurements. Yet, despite enforcing scattering mechanisms to occur in the high frequency optical region, an instability for repetitive measurements may still emerge due to either the electromagnetic roughness of the surface or the possible variation of dielectric constituents on the aging surface. In particular, surface roughness can diffuse the scattered signal over a broad cone of angles (i.e., coherent scattering effects step aside and make way to larger incoherent scattering contributions), whereas slight constituents variations can scale the scattering response of the debris. An example of this twofold behavior is evident for a monochromatic signal in the K_a -band propagating in free space (i.e., characterized by a dielectric constant $\varepsilon_1 = \varepsilon_1' = 1$ where ε_1' is the real part of ε_1) impinging with an incident angle ϑ_i on a lossless debris surface (i.e., characterized by a dielectric constant $\varepsilon_2 = \varepsilon_2'$ where ε_2' is the real part of ε_2) [18]. In particular, let us

consider a Physical Optics (PO) solution of Kirchoff's scattering model in the high-frequency optical region as a function of the electromagnetic roughness ks_h (i.e., the product of the wavenumber k and the surface rms height s_h) [18]. The reduction of coherent scattering as a function of electromagnetic roughness can be obtained as the so-called *zeroth-order PO solution for reflection by a rough surface* [37]. That is, the *coherent reflectivity for horizontal Γ_{coh}^H and vertical Γ_{coh}^V polarization* can be written as per eqs. (1.17) and (1.18), respectively, i.e.,

$$\Gamma_{coh}^H = \left| \frac{\cos \vartheta_i - \sqrt{\left(\frac{\varepsilon_2'}{\varepsilon_1'}\right) - (\sin \vartheta_i)^2}}{\cos \vartheta_i + \sqrt{\left(\frac{\varepsilon_2'}{\varepsilon_1'}\right) - (\sin \vartheta_i)^2}} \right|^2 (e^{-2ks_h \cos \vartheta_i})^2 \quad (1.17)$$

$$\Gamma_{coh}^V = \left| \frac{\sqrt{\left(\frac{\varepsilon_2'}{\varepsilon_1'}\right) - (\sin \vartheta_i)^2} - \left(\frac{\varepsilon_2'}{\varepsilon_1'}\right) \cos \vartheta_i}{\sqrt{\left(\frac{\varepsilon_2'}{\varepsilon_1'}\right) - (\sin \vartheta_i)^2} + \left(\frac{\varepsilon_2'}{\varepsilon_1'}\right) \cos \vartheta_i} \right|^2 (e^{-2ks_h \cos \vartheta_i})^2 \quad (1.18)$$

For example, in the K_a -band the variability of the coherent specular reflectivity in the horizontal polarization is clearly evident on the ordinate axis in Fig. 1.4 as a function of the incident angle on a lossless debris surface when the electrical permittivity is $\varepsilon' = 2$ for different roughness levels ks_h . For the sake of clarification, a similar variability for the coherent specular reflectivity shows up in the vertical polarization as well, albeit including the notching effect of the Brewster's angle.

Beside surface roughness, the variability of the coherent specular reflectivity in both the horizontal and vertical polarizations occur even in case of a slight change in the electrical permittivity. For example, for very small incident angles ϑ_i on the debris surface, a scaling effect of roughly 5 dB emerges when the electrical permittivity changes from $\varepsilon' = 2$ to $\varepsilon' = 3$.

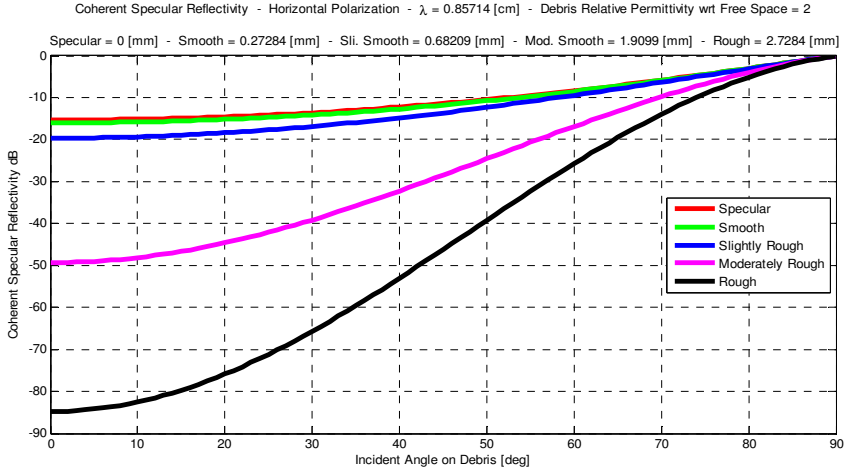


Fig. 1.4. Coherent scattering variability in the K_a -band (i.e., $\lambda=8.6$ mm) (H-pol) versus incident angle ϑ_i on a debris surface with dielectric constant $\epsilon' = 2$. Red curve: specular scattering (i.e., surface rms height $s_h=0$ mm); Green curve: smooth scattering (i.e., surface rms height $s_h=0.3$ mm); Blue curve: slightly rough scattering (i.e., surface rms height $s_h=0.7$ mm); Purple curve: moderately rough scattering (i.e., surface rms height $s_h=1.9$ mm); Black curve: rough scattering (i.e., surface rms height $s_h=2.7$ mm).

In pragmatic terms, for medium-size to large-size debris (with respect to λ) the scattering power at a radar receiver input (either GBR or SBR) can be assumed to originate in the high-frequency optical region as per the following scattering contributions:

- Primarily, from specular scattering comprising a flat or slightly curved surface whose normal points towards the radar antenna (including ancillary noncoherent scattering contributions depending on the surface roughness).
- Secondly, from possible multiple-bounce scattering from dihedral and trihedral shapes of the debris (including multiple bounces within cavity structures from slightly structured debris).

- Marginally, from sporadic scattering contributions related to diffraction from edges, discontinuities, and surface waves.

Remarkably, such a reasoning has been the guiding principle for the interpretation of radar-based observations of planets [22,38] and comets [39]. Consequently, a reasonable modeling assumption for operating a low-resolution surveillance radar for SSA is to (first) consider scattering mechanisms at a given λ to occur close to the high-frequency optical region and (then) define the RCS of a single debris as that of a point-like target and the RCS of a debris cloud as that of chaff. But beforehand, a few clarifications prove useful.

First of all, due to the possible conductivity of the debris, it is worth stressing that the power impinging on the debris may not only be scattered in several directions, but also be absorbed by the debris itself (this phenomenon can be handled by introducing the *extinction cross section* as the sum of an *absorption cross section* and a *scattered cross section*).

Second, it is well known (see [18] and [40]) that the RCS of a point-like target can be explicitly defined in terms of the scattering matrix or, equivalently, in terms of both the scattered field arriving at the radar antenna input (at a given polarization) and the incident field on the debris (with a given polarization).

Third, a debris cloud can be modeled as a distributed collection of single debris. Thus, in the high-frequency optical region scattering can be assumed to occur from multiple items similarly to chaff scattering mechanisms [41-43]. Yet, unlike chaff-based oriented resonant dipoles at large spatial densities, the scattering from a debris cloud can be assumed to arise from randomly positioned items at a lower spatial density. In principle, the appearance of multiple scattering among such individual entities might create electromagnetic coupling. It is well known that this phenomenon depends on the number, displacement, and

distance among the items. Yet, when spaced a few wavelengths apart in a random direction and orientation, it is reasonable to assume negligible mutual coupling within the debris cloud.

Finally, if the debris cloud spatial extent is larger than λ several phase offsets arise among the scattered field of each item within the cloud. Clearly, the larger the frequency of the radar the more reasonable the occurrence of phase offsets among the scattered fields from a debris cloud.

Consequently, elaborating on these aspects as per [36], the RCS of a debris target, i.e., either a debris cloud or, alternatively, a single debris (possibly characterized by one or more scattering centers) can be expressed as a function derived from, say N_d items (where the i -th item located at a distance R_i from the radar is characterized by a RCS σ_{RCS_i} , for $i = 1, \dots, N_d$). More specifically, taking into account the i -th radar-item round trip distance as a phase offsets $\phi_i = -4\pi R_i/\lambda$ along with an additional scattering phase offset ϕ_{s_i} (see for example [44, eq. (5)]), the RCS of a debris target can be formulated as

$$\sigma_{RCS} = \left(\sum_{i=1}^{N_d} \sqrt{\sigma_{RCS_i}} e^{j(\phi_i + \phi_{s_i})} \right)^2 \quad (1.19)$$

Thus, the single debris item (i.e., the i -th term in eq. (1.19) for $i = 1, \dots, N_d$) may possibly induce RCS fluctuations per se depending on the aspect angle since the coherent reflectivity of a debris is surely influenced by the electromagnetic roughness and relative permittivity of the constituents materials. Furthermore, additional fluctuations may emerge from either a debris cloud or from a single debris characterized by one or more scattering centers. In this case, peaks and nulls of σ_{RCS} may also depend on the occurrence of a 0 or π phase offset, respectively, among the relevant scattering items in eq. (1.19)

1.4.2 Radar Sensitivity

Taking into account the variability of the aforementioned scattering mechanisms, the range-of-power expected at a radar receiver should be *designed to be tunable* in order to fit a large instantaneous range-of-power along with dynamic gain control. Following Skolnik's wisdom *to make predictions of the radar performance using the Radar Equation* [45], a sensitivity analysis frames the radar receive power (at a given maximum operative range) with respect to the minimum and maximum receive power associated to a range of RCSs (see Fig. 1.5). More specifically, considering either a single debris or a debris cloud, let us represent an antenna with gain G_a at a given λ , radiating a peak power P_T at a distance R in the Fraunhofer region where the *center of RCS gravity* σ_{RCS} is located. In free space, a backscattered echo power is intercepted by the radar effective antenna area $A_{eff} = G_a \lambda^2 / 4\pi$ such that (including instrument losses L_l) the radar receive input power P_R can be approximated as

$$P_R = \frac{P_T G_a^2 \lambda^2 \sigma_{RCS}}{(4\pi)^3 L_l R^4} \quad (1.20)$$

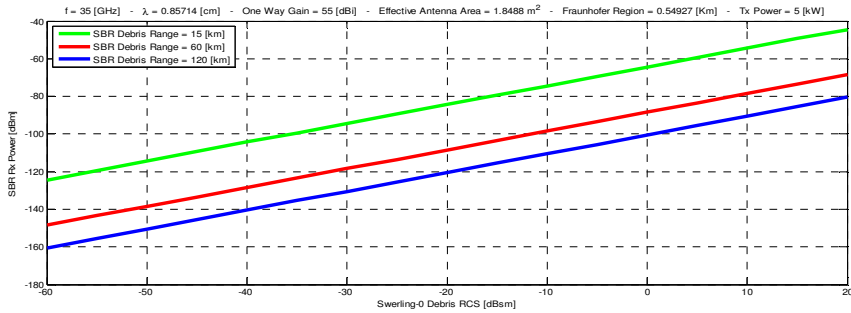


Fig. 1.5. Example of a power-based sensitivity-analysis for an SBR at 35 GHz for a 5-kW transmit peak power and a 2-m² effective antenna area. Maximum operative range at: 15 km (green curve); 60 km (red curve); 120 km (blue curve).

To this end, the plot in Fig. 1.5 shows a power-based sensitivity analysis in decibel-milliwatts (dBm) for an SBR receiver with respect to a set of target RCSs at 35 GHz for a 5-kW transmit peak power, a 2-m² effective antenna area, and a given set of maximum debris range (i.e., 15, 60, and 120 km).

In parallel to the power from a target, an analysis of the power from sources of interference paves the way for the identification of suitable Signal to Interference Ratio (SIR) regimes for signal processing schemes. In a nonhostile environment (i.e., without jammers), undesired interference intercepted by the radar can be due to large clutter discretets (e.g., satellites or orbital infrastructure in the FoV), or receiver and antenna noise [46] (including radiation sources from the Earth's surface, the solar photosphere, as well as galactic noise from the outer space). For example, a radar may monitor the outer space (see for instance the FoV of the leftmost SBR in Fig. 1.6). Clearly, the SBR-based scenario in Fig. 1.6 becomes a GBR-based scenario by simply replacing the leftmost SBR in orbit with a GBR on the Earth's surface. Another scenario which is applicable only to a SBR is represented by the FoV of the rightmost SBR in Fig. 1.6 spanning the Earth's surface.



Fig. 1.6. Scenarios for power intercepted by a SBR FoV. Leftmost SBR) FoV spanning the outer space; Rightmost SBR) FoV spanning the Earth's surface.

More specifically, the interference from a natural source of electromagnetic radiation of area A_{bb} located at a distance R_{bb} from the radar (i.e., $A_{bb} = \Omega_{bb} R_{bb}^2$ where Ω_{bb} is the solid angle subtending A_{bb} from either the GBR or SBR perspective), can be approximated as a blackbody of absolute temperature T_{bb} whose radiation is unpolarized. Accordingly, two fundamental cases for SSA are further described hereafter when the blackbody represents an *extended region* or a *limited region*, respectively, within the FoV of a radar [46].

- The blackbody represents an *extended region* when the entire solid angle Ω_{bb} can be assumed to overfit the ARP mainlobe (e.g., when the radiation source emerges from the Earth's surface or from galactic noise). In this case (see also [18]), for a given polarization p the power $P_{A(p)}$ intercepted by the effective antenna area A_{eff} of the radar (i.e., $A_{eff} = \Omega_{A_{eff}} R_{bb}^2$ where $\Omega_{A_{eff}}$ is the solid angle subtending A_{eff} from the blackbody perspective) can be approximated as

$$P_{A(p)} \cong A_{eff} \frac{K_B T_A}{\lambda^2} \mathcal{B} \Omega_{ARP} = K_B T_A \mathcal{B} \quad (1.21)$$

in which $\Omega_{ARP} = \lambda^2 / A_{eff}$ is the ARP solid angle, K_B is the Boltzmann constant, \mathcal{B} is the radar bandwidth, and the blackbody absolute temperature T_{bb} is approximated by a constant T_A . For example, for an SBR with an FoV spanning the Earth at, say $T_0 = 290$ K, or spanning the outer space at, say $T_{galactic} = 6$ K, T_A can be approximated as $T_A \cong T_0$ or $T_A \cong T_{galactic}$, respectively.

- On the other side, the blackbody represents a *limited region* when the entire solid angle Ω_{bb} subtending A_{bb} can

be assumed to underfit the ARP mainlobe or sidelobes (e.g., when the radiation source emerges from the solar photosphere). If the SBR ARP mainlobe with solid angle Ω_{ARP} can be assumed to envelope the entire solid angle Ω_{bb} , the following approximation proves adequate:

$$P_{A(p)} = K_B T_A \left(\frac{\Omega_{bb}}{\Omega_{ARP}} \right) B = K_B T_A' B \quad (1.22)$$

Again, the blackbody absolute temperature T_{bb} is approximated by a constant T_A whereas the scaling factor Ω_{bb}/Ω_{ARP} (which is less than unity) is embedded in the general T_A' term in eq. (1.22). Alternatively, when an SBR ARP sidelobe (characterized by a sidelobe gain G_{sl} , an equivalent sidelobe effective area $A_{eff_sl} = \lambda^2 G_{sl}/4\pi$, and an equivalent sidelobe solid angle $\Omega_{ARP_sl} = \lambda^2/A_{eff_sl}$) can be assumed to envelope the entire solid angle Ω_{bb} , the following approximation proves adequate:

$$P_{A(p)} = K_B T_A B \left(\frac{A_{eff_sl}}{A_{eff}} \right) \left(\frac{\Omega_{bb}}{\Omega_{ARP}} \right) = K_B T_A B \left(\frac{G_{sl}}{G_a} \right) \left(\frac{\Omega_{bb}}{\Omega_{ARP}} \right) = K_B T_A' B \quad (1.23)$$

Once again, the blackbody absolute temperature T_{bb} is approximated by a constant T_A , whereas the scaling factors G_{sl}/G_a (i.e., the sidelobe to mainlobe ratio) and Ω_{bb}/Ω_{ARP} (which are both less than unity) are embedded in the general T_A' term as well.

In summary, the interference power $P_{A(p)} = K_B T_A' B$ for a blackbody representing an *extended region* implies $T_A' = T_A$ as per eq. (1.21) whereas a *limited region* entails $T_A' = T_A(\Omega_{bb}/\Omega_{ARP})$ as per eq. (1.22) or $T_A' = T_A(G_{sl}/G_a)(\Omega_{bb}/\Omega_{ARP})$ as per eq. (1.23) when the blackbody is spanned by the ARP mainlobe or sidelobe, respectively.

For the sake of clarification, several comments follow from a system engineering perspective (see also [18]). At a distance of 1 Astronomical Unit (AU) from an SBR (approximately 150 million km), the diameter of the Sun (approximately 1.4 million km) is subtended approximately by a 0.5° angle. In the K_a -band at 35 GHz, the 0.86-cm wavelength applied to an effective antenna diameter of, say 1 and 10 m, results in a 3-dB beamwidth coarsely around 0.5° and 0.05° , respectively. As a reference example, let us then consider a radar operating in the K_a -band with an effective antenna diameter of 1 m with a FoV spanning the solar photosphere. In this case, as a rough order of magnitude it is reasonable to assume $T_{sun} = 6000$ K, i.e., $T_A \cong T_{sun}$, $G_{sl}/G_a \cong 0.001$ (i.e., -30 dB), and $\Omega_{bb}/\Omega_{ARP} \cong 1$. In this example, it is thus evident that a radar (either GBR or SBR) for SSA operating in the K_a -band with its FoV pointing towards the Sun via its ARP mainlobe may suffer from radiation noise from the solar photosphere. Yet, if the FoV spanning the Sun occurs via its ARP sidelobes at less than 30 dB with respect to the ARP mainlobe, the radiation noise from the solar photosphere is less detrimental. Downstream this digression, it is also worth noting that, depending on the SBR FoV and related ARP with respect to the environmental scenario, the general *antenna temperature* T_A' may comprise contributions from T_0 , $T_{galactic}$, T_{sun} , or a weighted combination thereof.

Now, considering a radar with either an AESA antenna, a reflector based antenna, or a hybrid combination of a reflector with an AESA as its feed, the system temperature T_S can be written as [47]

$$T_S = T_A' + T_R \quad (1.24)$$

where T_R is the receiver temperature. For each of the above antenna configurations, the receiver temperature T_R can be written as [40]

$$T_R = (F_{op} - 1)T_{op} \quad (1.25)$$

where F_{op} represents the receiver operative noise figure and T_{op} represents the receiver operative temperature. Again from a system engineering perspective, considering an SBR without onboard cryogenics with a FoV towards the Earth's surface, an approximation is $T_0 = 290$ K for both T_A and T_{op} which, in turn, results in $T_S = F_0 T_0$ where F_0 is the SBR receiver standard noise figure at T_0 [40].

Finally, the interference power that a radar (either GBR or SBR) for SSA must cope with can be expressed as

$$P_I = K_B T_S \mathcal{B} \quad (1.26)$$

Fig. 1.7 shows an example of the interference power for different receiver bandwidths \mathcal{B} of an SBR in the K_a -band. In this scenario, the sun extent lies in the ARP sidelobe (i.e., $G_{sl}/G_a \cong -30$ dB and $\Omega_{bb}/\Omega_{ARP} = 0.8$) whereas the main interference is due to contributions from the receiver and the Earth's surface (see the red and green curves in Fig. 1.7, respectively). On the other side, when the sun extent is spanned by the ARP mainlobe and $\Omega_{bb}/\Omega_{ARP} = 1$, the main interference contribution becomes sun-related (see the blue curve in Fig. 1.8).

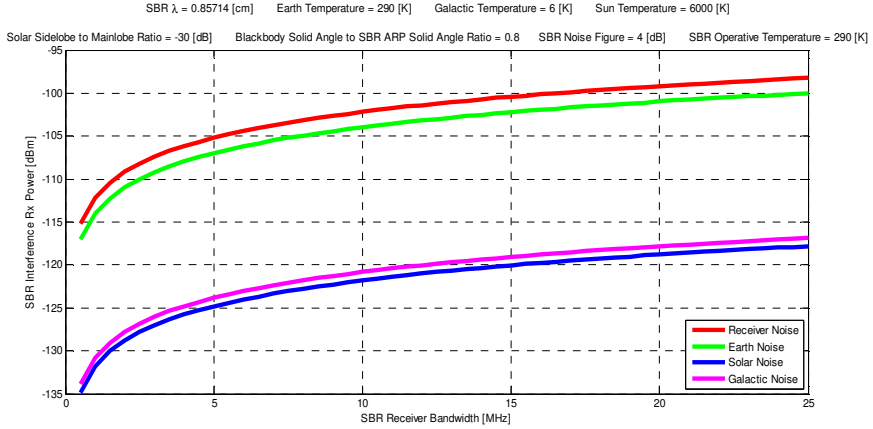


Fig. 1.7. Example of interference power contributions from a sidelobe in the K_a -band with respect to B (Receiver Noise Power dominant) with $G_{sl}/G_a = -30$ dB; $\Omega_{bb}/\Omega_{ARP} = 0.8$; $F_0 = 4$ dB. Receiver Noise Power (red curve); Earth Noise Power (green curve); Solar Noise Power (blue curve); Galactic Noise Power (purple curve).

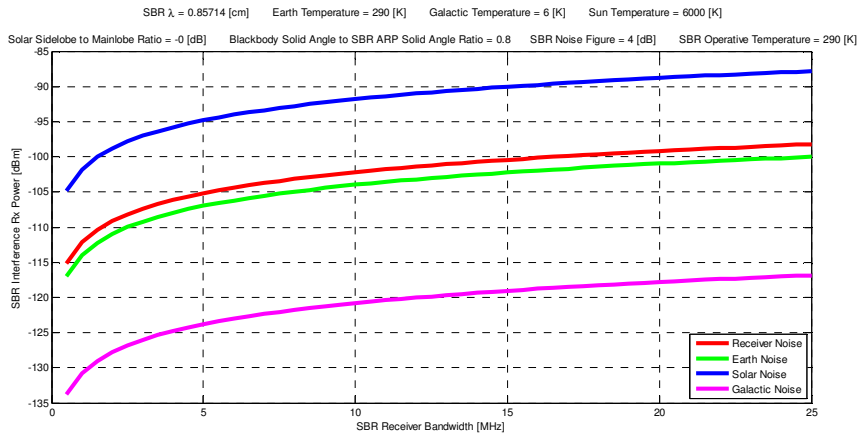


Fig. 1.8. Example of interference power contributions from the mainlobe in the K_a -band with respect to B (Solar Noise Power dominant) with $\Omega_{bb}/\Omega_{ARP} = 0.8$; $F_0 = 4$ dB. Receiver Noise Power (red curve); Earth Noise Power (green curve); Solar Noise Power (blue curve); Galactic Noise Power (purple curve).

1.4.3 Digression on the Doppler Effect

A brief digression follows for the Doppler effect first on a monochromatic signal at a given wavelength λ and, subsequently, on a pulsed signal of duration T occupying a bandwidth \mathcal{B} . It is well known [40,45,48] that the Doppler effect (round-trip) can be approximated as a shift of the frequency of the monochromatic signal by $f_d = -2v/\lambda$. In particular, v represents the relative radial velocity between the radar and the target, whereas the “minus” sign is a convention which enforces the Doppler frequency shift f_d to be positive for an approaching target (when an outward target motion is defined positive). Now, the imposing debris velocities induce a significant Doppler stress on signals for SSA (particularly in the K_a -band). More specifically, the Doppler effect on the received echo can amount to a few megahertz (e.g., as a rough reference, one may consider that a 16-km/s relative velocity at 36 GHz would result in a Doppler frequency shift around 3.8 MHz). In order to delve more deeply into this topic, instead of using a monochromatic signal, let us consider a signal whose frequency support occupies a bandwidth \mathcal{B} . Accordingly, on a single-pulse echo pertaining to a point-like target, f_d affects solely the carrier of the echo only in case a narrowband assumption for the signal holds. In other words, only in case of a narrowband assumption for the signal, the scaling of the amplitude and the stretching of the time axis in the echo return by a γ_d factor can be neglected (e.g., for a f_{Ka} carrier in the K_a -band $\gamma_d = 1 + f_d/f_{Ka}$). More specifically, Rihaczek [49,50] provides key bounds for employing either narrowband or wideband representations of the signal and, consequently, for adopting a suitable formulation of the signal ambiguity function. Indeed, referring to c as the speed of light in the propagation media and, for a relative radial velocity v and a signal with a time-

bandwidth product $T\mathcal{B}$, the narrowband representation of a signal relies on the following assumption

$$v \ll \frac{c}{BT} \quad (1.27)$$

whereas for a radial acceleration \dot{v} a narrowband representation relies on the following inequality to hold

$$\dot{v} \ll \frac{c}{BT^2} \quad (1.28)$$

1.5 Motion Models

From a mechanical perspective, debris translational and rotational motions occur within an inertial² (Euclidean) vector space comprising both GBRs and SBRs. In particular, the Earth oblate keeps revolving around the Sun, along with additional spinning, precessing, and nutating motions due to celestial mechanics. Within this framework, an SBR moves periodically around the Earth on elliptical orbits while the Earth keeps spinning around its own axis. In parallel, MMODs (either meteoroids passing by the Earth or debris swarms periodically orbiting around the Earth) move according to Newtonian and Eulerian mechanics, whereby the Earth exerts the main central force. Armed with such a general overview, the following paragraphs identify further assumptions and insights for radars (either GBRs or SBRs) aimed at supporting SSA. Namely, mechanical behaviors, operative paradigms for orbit determination, and debris state transition models.

² For near-Earth SSA, an inertial system is assumed to exist and can be referred to as “distant” stars, e.g., the First Point of Aries, or the First Point of Libra.

1.5.1 Newtonian and Eulerian Mechanics

For translational astrodynamics, the motion of both debris or SBRs lies on elliptical orbits. These orbits result from fundamental integrals of the two-body problem [51,52]. In addition, perturbation drifts from such elliptical orbits occur as a disturbing acceleration \mathbf{a}_d due to the superposition of nuisances: namely, zonal and tesseral geopotential gradients; gravitational influences of the Sun and the Moon (with negligible gravitational effects from other solar planets); drifting effects due to atmospheric drags (predominantly in lower LEO regions); and Solar Radiation Pressure (SRP) [51-54]. In principle, by neglecting the aforementioned contributions to \mathbf{a}_d it is possible to model the nominal translational motion of an orbiting item as

$$\ddot{\mathbf{p}} = -\frac{\mu}{|\mathbf{p}|^3}\mathbf{p} + \mathbf{a}_d \cong -\frac{\mu}{|\mathbf{p}|^3}\mathbf{p} \quad (1.29)$$

where \mathbf{p} is the item's position, $\ddot{\mathbf{p}}$ is the second order time derivative of \mathbf{p} , and μ is a gravitation related constant. Indeed, by neglecting \mathbf{a}_d , important insights can emerge from the conservation of energy in the two-body problem in an inverse square gravity field [52]. For example, the *vis-viva* equation for the speed V_I of an item on an elliptical orbit characterized by a semimajor axis a_a can be obtained with an inverse dependence on the geodetic height h_I of the item (as per Kepler's laws), i.e.,

$$V_I = \sqrt{\mu \left(\frac{2}{h_I} - \frac{1}{a_a} \right)} \quad (1.30)$$

While relative translational velocities among items can be less than 1 km/s for rendezvous trajectories, in case of head on trajectories relative velocities may reach up to 16 km/s in LEO

regions and, astonishingly, from 20 km/s up to 70 km/s for meteoroids.

On the other side, in order to address rotational astrodynamics, it must be stressed once again that debris bodies spawn due to possible explosions, collisions, or fragmentation events. In the long term, space weather may also induce an erosion of debris constitutive materials. Consequently, a mild and slow tumbling or a staggered spinning behavior may also emerge. This is mostly true especially at lower orbits and on larger debris bodies, where the entries of the (diagonalized) inertia matrix $\mathbf{I}_Q = \text{diag}(I_{Q11}, I_{Q22}, I_{Q33})$ of an item are certainly dissimilar (i.e., $I_{Q11} \neq I_{Q22} \neq I_{Q33}$), thus inducing possible gravity torques [52]. Remarkably, the possible rotational behaviour of debris cues how likely (or rather unlikely) it is to perform *orbit-repetitive measurements* for debris detection and tracking from the *same radar-debris geometrical scattering perspective*.

For data fusion operations, it is also fruitful to identify the state-space liaison among track estimates (also known as tracklets) obtained by an SBR and those obtained by a GBR. Interestingly, this can be tackled as a problem of particle kinematics with moving frames [52] for *debris position and velocity state* in relation to a GBR and a SBR. Clearly, the knowledge of the distance and velocity of an SBR with respect to that of a GBR can be obtained using GNSS receivers both on-board and on-ground. Remarkably, if the estimation accuracies of a debris position and velocity from an SBR were to be finer than the estimation accuracies obtained by GBRs, the quantitative benefit of using SBRs for SSA would thus be proven.

1.5.2 Laplacian and Gaussian Orbit Determination

Considering operations for SSA, probabilistic impacts rely on orbital predictions to be computed several orbital periods in

advance before a debris-spacecraft conjunction is likely to occur. The estimation uncertainty of the conjunction (which is propagated from a reference epoch t_0 to a future conjunction time t) worsens when increasing the time elapse $\Delta t = t - t_0$. This, in turn, depends on the adopted *orbit determination* paradigm. In [51], it is clarified that the problem of *orbit determination* of an item can be distinguished between two cascaded phases. The first phase is the *preliminary orbit determination* providing a (coarse) 6-tuple set of Keplerian parameters from (at least) a 6-tuple set of observables, and generally no *a priori* information. The second phase is the *orbit estimation* providing a (fine) 6-tuple set of Keplerian parameters, possibly relying on *a priori* information and approached via either batch or sequential estimations.

For a preliminary orbit determination, starting from a given initial condition $\{\mathbf{p}(t_0), \dot{\mathbf{p}}(t_0)\}$ (i.e., a 6-tuple set of position \mathbf{p} and velocity $\dot{\mathbf{p}}$ parameters at an instant t_0) it is possible to solve eq. (1.29) at a given time t . Such a solution is more or less adherent to the true future item's motion depending on the extent of the time elapse Δt . A preliminary orbit determination based on the aforementioned $\{\mathbf{p}(t_0), \dot{\mathbf{p}}(t_0)\}$ initial condition is known as a *Laplacian orbit determination* [51]. Another preliminary orbit determination is the *Gaussian orbit determination* [51] which uses different sets of observables displaced in time and space. In general, a given initial condition (necessary for predicting the $\{\mathbf{p}(t), \dot{\mathbf{p}}(t)\}$ kinematic pair of an item at a future time t) is deemed as much "valid" as Δt is "short." The validity derives from neglecting the disturbance acceleration \mathbf{a}_d during the time elapse Δt as per eq. (1.29). In line with this overview, GBRs in beam park modes are able to observe only a Too Short Arc (TSA) during observation campaigns [55]. In general, it is reasonable to assume that this prevents GBRs from estimating $\{\mathbf{p}(t_0), \dot{\mathbf{p}}(t_0)\}$ during the passage event of an orbiting item. Indeed, the preclusion of a Laplacian orbit determination derives from large debris-GBR distances, warped surveillance cells, and limited

scanning capabilities, especially in case of large reflector-based assets. Now, at least in principle, a Gaussian orbit determination paradigm can be adopted using a single GBR asset. In particular, this would be possible in case of advanced surveillance modes depending on the scanning capabilities of phased arrays [7,9] as well as on the density of the debris population in the surveillance scenario. In fact, a network of GBRs for SSA is usually exploited in either beam park or scanning surveillance modes for collecting as many TSA measurements as possible. In this case, such a GBR network faces the issue of grouping contacts from the available TSA measurements. Moreover, in a network-based measurement campaign for SSA, it is very likely that multiple observations (eventually cueing the tracklet of an object) can be obtained only after the object has presumably propagated for a number of orbits. Therefore, the motion model for such a “long time span Δt ” certainly abides by nonlinear dynamics in which both conservative and nonconservative forces must be taken into account, thus banning the approximation in eq. (1.29). As a consequence, Tommei *et al.* [55] tackle the problem of orbit determination for SSA from available TSA measurements exploiting legacy studies on heliocentric orbiting asteroids. In particular, Tommei *et al.* [55] constraint the track-association (i.e., the association of more than one available TSA measurements to the same orbiting item) via recursive correlations of observables belonging to Orbital Admissible Regions (OAR). Alternatively, Delande *et al.* [56] represents another modern approach encompassing multi-object tracking based on Random Finite Sets (RFS)[57].

Remarkably, an AESA-based SBR aimed at monitoring a smaller and less warped surveillance space while it keeps orbiting the Earth (see Fig. 1.9) represents an interesting scheme to overcome the difficulties of GBR networks. Indeed, considering limited time spans on the orders of a second for debris detection and tracking in a small FoV (e.g., roughly a 100-km

instantaneous-range from an orbiting SBR), it appears fruitful to model both debris and SBRs moving along straight lines in 3-D at constant hyper-velocity with no maneuvering, i.e., a Near Constant Velocity (NCV) motion (see Fig. 1.10).

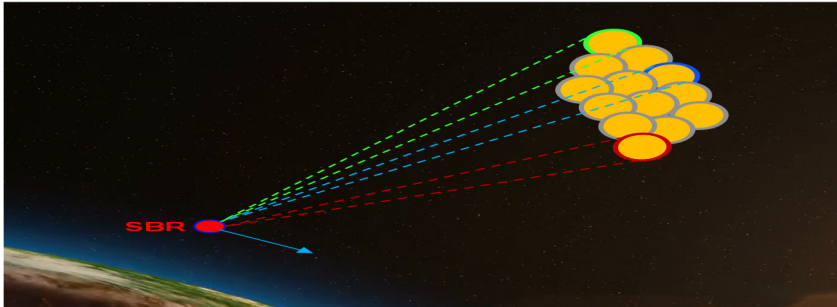


Fig. 1.9. AESA-based SBR raster scanning a specific VoI.

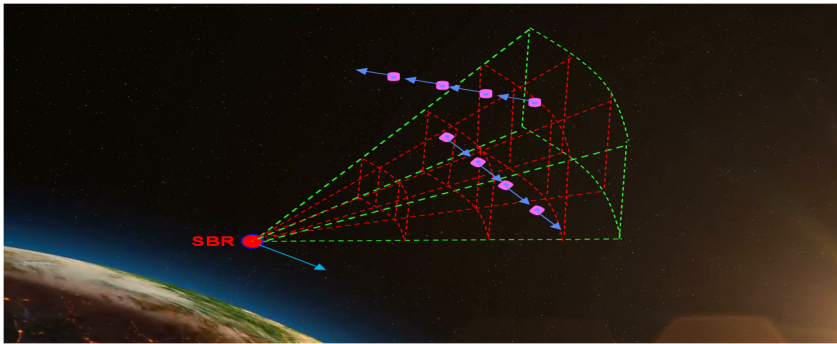


Fig. 1.10. Debris moving along straight lines for a short observation time elapse.

The validity of the NCV motion is clarified in Figs. 1.11 and 1.12 by showing two examples for possible degradation of the NCV assumption. This appears in terms of rectilinear displacement of a debris orbiting at an arbitrary reference geodetic height according to eq. (1.29). Starting from an arbitrary true anomaly (e.g., 30°), the rectilinear displacement with respect to a time elapse of roughly 2 s is negligible as shown in Fig. 1.11(b) and becomes evident after 10 min as shown in Fig. 1.12(b).

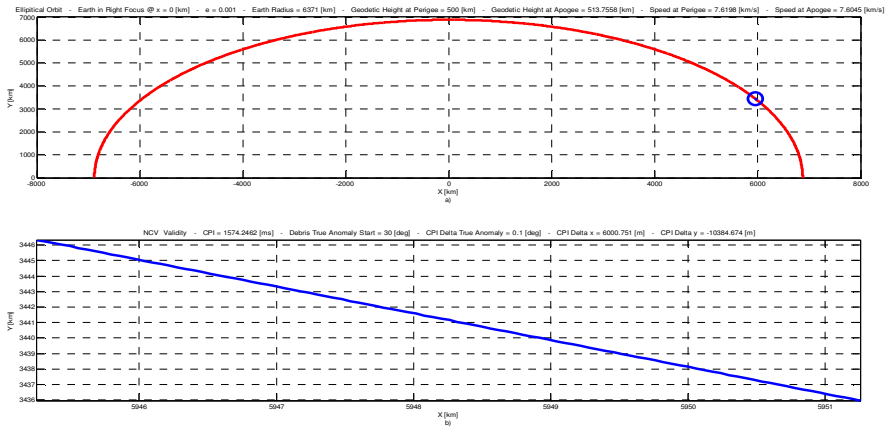


Fig. 1.11. Negligible degradation of NCV assumption - Geodetic Height at Perigee 500 km, True Anomaly Start 30° (shown as a blue circle on the elliptical orbit), Speed at Perigee 7.6 km/s, Time Elapse 1.6 seconds. a) elliptical orbit ; b) zoom on rectilinear displacement.

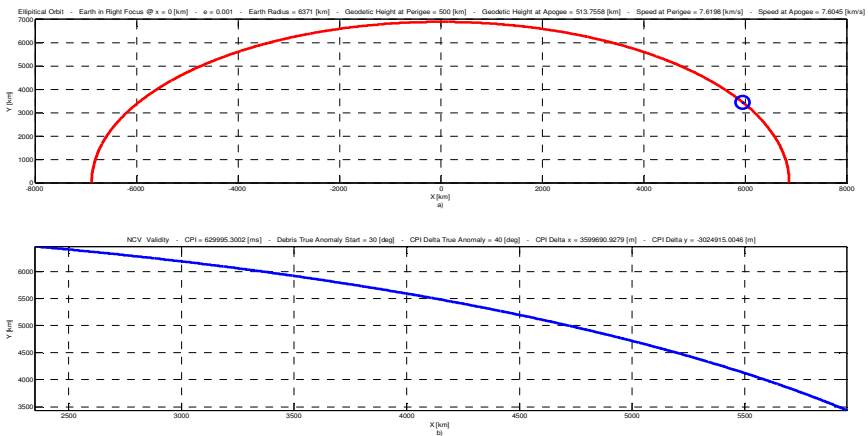


Fig. 1.12. Prominent degradation of NCV assumption - Geodetic Height at Perigee 500 km, True Anomaly Start 30° (shown as a blue circle on the elliptical orbit), Speed at Perigee 7.6 km/s, Time Elapse 10 minutes. a) elliptical orbit ; b) zoom on rectilinear displacement.

Accordingly, in a short elapse time the approximation in eq. (1.29) holds tight, whereby an AESA-based SBR can collect with scanning agility the observable $\mathbf{Z}_{\mathcal{K}} \triangleq \{\mathbf{z}_1, \dots, \mathbf{z}_{\mathcal{K}}\}$, defined as a set of SBR measurements \mathbf{z}_i (for $i = 1, \dots, \mathcal{K}$) at \mathcal{K} -instants (from an initial time instant t_1 to a final time instant $t_{\mathcal{K}}$). From such a set of observables, an SBR can possibly estimate the state $\{\mathbf{p}(t_j), \dot{\mathbf{p}}(t_j)\}$ of an orbiting item at a given time instant t_j occurring within the elapse time and, consequently, allow for a Laplacian orbit determination of the item. Thus, with an SBR, there is no need to wait and hope for TSA observations in the future to be properly coupled for confident orbit determinations. Interestingly, in case of a dense scenario solely pertaining to the FoV (see for example the 2 purple tracklets in Fig. 1.10) an automatic Multi Target Tracking (MTT) paradigm can be adopted for discriminating a group of contacts [58,59]. Since observables collected by an SBR during a short elapse time can be used to estimate immediately the orbit of an item, it is thus possible to remove orbit determination ambiguities pertaining to sets of observables widely displaced in time and space. As a by-product, the set of valid hypotheses on observation-paths that an already detected target has "potentially" produced (i.e., the streams of observations for a *distinguishable debris* in [56]) can be decreased with beneficial effects on the complexity of multi-object filtering for SSA (see [56, Fig. 1]).

1.5.3 Approximation for Debris State Transition Model

Kinematic approximations prove useful to frame debris state transitions and, eventually, the necessary operative modes for radar measurements (and, therefore, the debris controllability and observability). For the sake of clarification, a few insightful comments follow taking into account Figs. 1.10 and 1.11.

In case of a white process noise, the state-transition matrix of a dynamic system embodies the Markovian paradigm to be used in sequential orbit estimation and allows analyzing how trajectory errors may evolve in a time elapse Δt [52]. Interestingly, for nonlinear dynamic systems evolving in the time variable t , the *state-transition matrix* $[\Phi(t, t_0)]$ represents the sensitivity of the state $\mathbf{x}(t)$ to the initial state $\mathbf{x}(t_0)$ where t_0 is the initial instant, i.e., $[\Phi(t, t_0)] \triangleq \partial \mathbf{x}(t) / \partial \mathbf{x}(t_0)$, yet without mapping $\mathbf{x}(t_0)$ into $\mathbf{x}(t)$ as it occurs in linear dynamic systems [52]. In principle, when a radar collects a number of measurements during a Δt much larger than “seconds”, the debris motion departs from being approximately rectilinear, the disturbing acceleration \mathbf{a}_d cannot be neglected, and eq. (1.29) is no longer applicable (in this case, $\dot{\mathbf{p}} = -(\mu/|\mathbf{p}|^3)\mathbf{p} + \mathbf{a}_d$). On the other side, for automatic tracking [58] during a short elapse time, a linear Continuous White Noise Acceleration (CWNA) model [60] allows representing the NCV motion. In particular, a linear dynamic system can be assumed neglecting forcing terms (e.g., assuming no spawning event is occurring) from the time instant t_1 to the time instant $t_{\mathcal{K}}$ and considering a constant system matrix and process noise matrix (a discretized version of the CWNA model can be elaborated defining $t_{\mathcal{K}} - t_{\mathcal{K}-1} \triangleq \mathbb{T}$). The CWNA model defines the velocity of a debris as the integral (in the mean square sense) of white noise (i.e., a Wiener process) and allows representing the Power Spectral Density (PSD) of the process noise $q_j(t) = q_j$ in case of noise stationarity [60]. In addition, by properly constraining the CWNA model parameters³, it is also possible to characterize mild changes in debris velocity components during an observation interval considering time spans beyond the order of a second.

³ For example, the NCV motion can be implemented as a CWNA model during a short elapse time by properly constraining a small $\sqrt{q_j \mathbb{T}}$ (where q_j and \mathbb{T} are expressed in m^2/s^3 and s , respectively).

1.6 Leitmotiv Question and Keystones for Space-Based SSA

The ontology described in this chapter provided reasonable insights on space physics, debris fluxes environmental scenarios, orbital mechanics, along with ties to space-based radio science, and general remote sensing experimental legacies. Moreover, it pinpointed an SBR power-based sensitivity analysis aimed at indicating specific SIR regimes for possible onboard processing schemes. The discussion on channel-target phenomenology as well as motion models lead to a leitmotiv question proposed in this Ph.D. work:

“How can a SBR for SSA be designed to estimate at a given time epoch t_0 at least an initial condition $\{\mathbf{p}(t_0), \dot{\mathbf{p}}(t_0)\}$ of one (or more than one) debris crossing the SBR FoV?”

The answer to such question relies on following three keystones:

- An approximation for NCV motion during limited time spans on the order of s.
- An AESA-based SBR sensor architecture in the K_a -band conceived around a digital processing core.
- A cognitive-based onboard tracker for Bayesian MTT.

Chapter 2

SIMO SBR Sensor Architecture for Debris Detection and Tracking

The idea of exploiting the K_α -band on a real aperture SBR for debris detection and tracking represents a novel space-based remote sensing archetype to support near-Earth SSA [2]. Indeed, in 1978 the first digital space-based Synthetic Aperture Radar (SAR) was embarked as part of the Seasat satellite for studying ocean physics [61], along with an altimeter, a scatterometer, and multi-spectral radiometers. Subsequently, early taxonomies for SBRs classes [27] comprised Type I SBRs aimed at tracking for guidance control during rendezvous maneuvers; Type II SBRs providing SAR reflectivity mapping; and Type III SBRs for surveillance and eventually early warning Moving Target Indicator (MTI) functionalities. A couple of decades later, SBRs classes [62] were also described as Earth Observation (EO) SARs for geoscience services, sounders for planetary explorations, and surveillance SBRs for the Homeland Protection (HP). Now, a real aperture SBR providing timely, accurate, and reliable inference on debris populations in the K_α -band, may complement ground based surveillance assets for SSA by tackling debris populations with an average size smaller than 10 cm. In addition, it may provide a shorter, and more accurate, small debris conjunction prediction, e.g., one or two orbits in advance with respect to those needed by ground based sensors, along with a smaller uncertainty. Such an SBR concept (represented by the inner dashed red box in Fig. 2.1) is built upon a digital core interfacing the onboard computer, the power supply, and the data storage and downlink

subsystems of a spacecraft (i.e., the outer black box in Fig. 2.1). The SBR system architecture has been envisaged as a superheterodyne transceiver comprising an AESA subsystem, a Radio Frequency (RF) Subsystem, and a digital Subsystem. Within the digital subsystem a microprocessor (μP) acts as an SBR manager whereas an Ultra Stable Oscillator (USO) provides a stable reference for coherent radar operations.

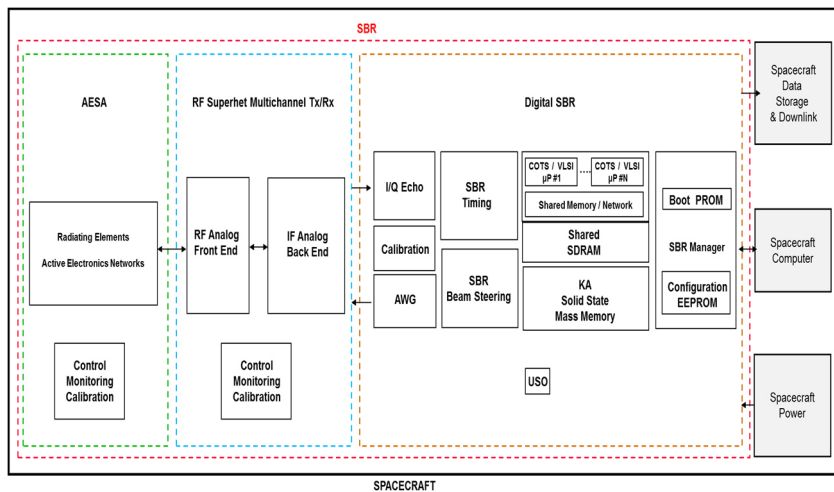


Fig. 2.1. SBR system architecture.

In general terms, the SBR system architecture in Fig. 2.1 is aimed at implementing a bespoke fully-polarimetric monopulse-based radar (operating “similarly” to legacy air-to-air missions [63]). In order to perform detection and parameter estimation of sprouting debris in the SBR FoV, the SBR configuration proposed in this chapter is Single Input Multiple Output (SIMO) whereby the FoV is illuminated by one channel on transmit while multiple channels are used on receive. The SBR subsystems hinted in Fig. 2.1 will be further clarified throughout the rest of the chapter with close ties to the SBR monopulse-based functional architecture depicted in Fig. 2.2.

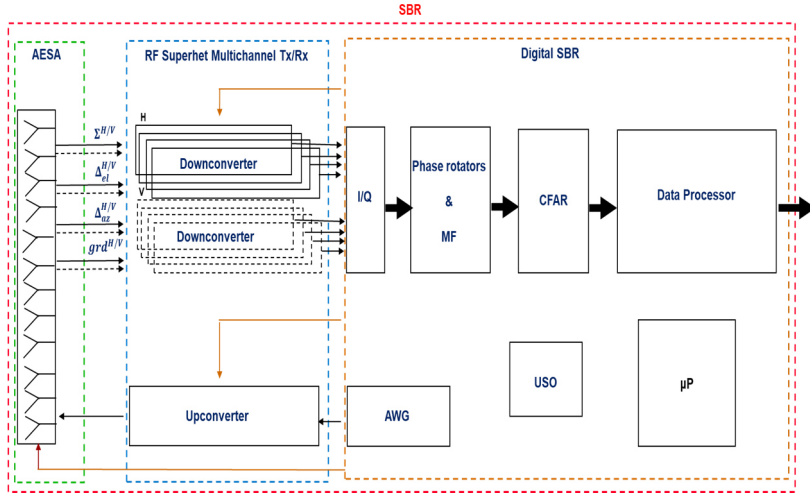


Fig. 2.2. SBR monopulse-based functional architecture.

In simple terms, the transmit waveforms at a given polarization are synthesized within an Arbitrary Waveform Generator (AWG). The upconverter block translates the transmit waveform carrier to the K_a -band (viceversa, the downconversion chains translate the spectrum of the echoes from the K_a -band towards the digital subsystem). The AESA subsystem allows for digitally steerable radiation patterns in both azimuth and elevation planes with no need for True Time Delay Lines (TTDL) due to the limited required operative bandwidth of a few megahertz (i.e., $\mathcal{B} \leq 2$ MHz). The complex envelope extraction process pertaining to a complex data hyper-cube occurs within an echo digitizer (i.e., see the I/Q Echo subsystem in Fig. 2.1 and the I/Q functional block scheme in Fig. 2.2). The acquired samples are processed at every range-gate through a Doppler filter bank implementing Pulse Compression (PC) via a cascade of phase rotators and Matched Filters (MFs). The branch with maximum modulus value (built upon the noncoherent combining of a burst of pulse echoes) is fed to a Constant False Alarm Rate like

(CFAR-like) block. Finally, the data stream is fed to the data-processor for tracking purposes. For onboard tracking in limited time spans on the order of seconds, specific parameter estimates extracted in dual polarization from a set of complex data hyper-cubes pave the way for further Bayesian inference capabilities on small-size debris dynamic states as well as on scattering-related signatures. Namely:

- The target range parameter (r), computed via the monopulse sum-channels by scaling the delay parameter estimate.
- The target elevation and azimuth angle parameters (θ, φ), computed via the monopulse delta-channels (jointly with the sum-channels for gain normalization) by adding the monopulse delta difference estimations and the *a priori* known AESA off-broadside angles.
- The target RCS parameter (σ_{RCS}), computed via the monopulse sum-channels (jointly with the monopulse delta-channels for ancillary target attributes) by time series analysis downstream the MF outputs.

In holistic terms, such an SBR payload is conceived to act as a stand-alone active remote sensing instrument in the K_a -band, embarked on a spacecraft orbiting around planet Earth with a standard platform agility for attitude control. In this case, we may assume that the SBR payload surveillance mode may rely solely on the steering capabilities of the AESA antenna, and whose operative orbit-duty-cycle is limited by power consumption and thermal conditioning thereof. Consequently, from a set of complex data hyper-cubes acquired in limited time spans on the order of seconds and deeply processed onboard the SBR for detection and tracking purposes, an efficient telemetry with a

reduced amount of information bits can be formed. Subsequently, such a telemetry can be either transferred in downlink to the ground station for supporting SSA or, more dauntingly, for providing future spacecraft with an autonomous early warning capability for direct collision avoidance maneuvering [5]. For the sake of completeness, it is also worth stressing that the assumed cardinality of a constellation of SBRs needed to properly support SSA would be, de facto, a mission-dependent aspect which is outside the scope of this work. Clearly, such a cardinality depends on the desired VoI for the mission along with the operative SBR instantaneous FoV and overall FoR. In other words, the SBR instantaneous FoV and overall FoR are scalable concepts depending on the available transmit peak power (on the order of kilowatts), payload multichannel diversity, and AESA steering capabilities. Finally, the idea of a K_a -band SBR based on an AESA with a 2-D surface area on the order of 1 m^2 can be conceived to be embarked on small-size spacecraft launched by either dedicated airborne platforms or small rockets (e.g., Vega).

The rest of the chapter is organized as follows. Section 2.1 clarifies the SBR sensor data and operative strategies. Section 2.2 outlines further details on the SBR sensor functional architecture shown in Fig. 2.2 (with a close intertwinement with the subsystem perspective in Fig. 2.1).

2.1 SBR Sensor Data and Operative Strategies

This section outlines the sensor timing hierarchies in surveillance mode, the complex data hyper-cube structure, and the Low Pulse Repetition Frequency (Low-PRF) Range and Range-Rate Search (RRRS) with a Pause While Scan (PWS) contacts collection strategy.

2.1.1 Time Hierarchies and Complex Data Hyper-Cube

Considering an operative surveillance mode, the SBR raster scans a specific VoI to obtain an overall acquaintance on a set of cells⁴ (as a reference see Fig. 1.9). In particular, the SBR hops its AESA transmit beam according to a programmable temporal hierarchy. As a general example, the temporal hierarchy described in [63] is made of a frame at its root (whose elapse time comprises the spanning of the entire set of yellow spots in Fig. 1.9). A frame is parsed into a set of (horizontal or vertical) bars whereas each bar comprises a number of beam positions (i.e., a group of yellow spots in Fig. 1.9). Each beam position occurs during a dwell which is, in turn, temporally grouped into a number of looks with each look spanning several Coherent Processing Intervals (CPIs). Finally, a CPI embeds a set of one (or more than one) Pulse Repetition Interval (PRIs). For the sake of clarification, the foregoing (programmable) temporal hierarchy hinted in [63] is pictorially represented in Fig. 2.3.

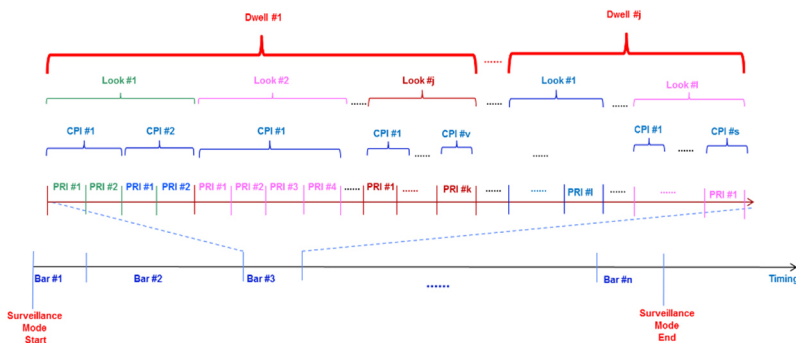


Fig. 2.3. SBR (programmable) temporal hierarchy in surveillance mode.

⁴ Each cell, addressed as a Cell Under Test (CUT), entails a binary hypothesis test (in terms of whether or not a debris might be present) along with possible parameters estimates thereof.

The SBR proposed in this work has been envisaged to rely on a (programmable) temporal hierarchy based on [63] where each dwell comprises 1 look spanning 1 CPI made of several PRIs. Accordingly, at every dwell the set of In-phase (I) and Quadrature (Q) components (extracted by the I/Q functional block scheme in Fig. 2.2) can be structured into a complex data hyper-cube. The complex data hyper-cube is depicted in Fig. 2.4 and comprises a number of dimensions including the fast-time ξ_{fast} , the slow-time ξ_{slow} , as well as additional dimensions such as the receive polarization ξ_{pol} , the receive Doppler frequency ξ_{Dop} , and the monopulse channel ξ_{mon} .

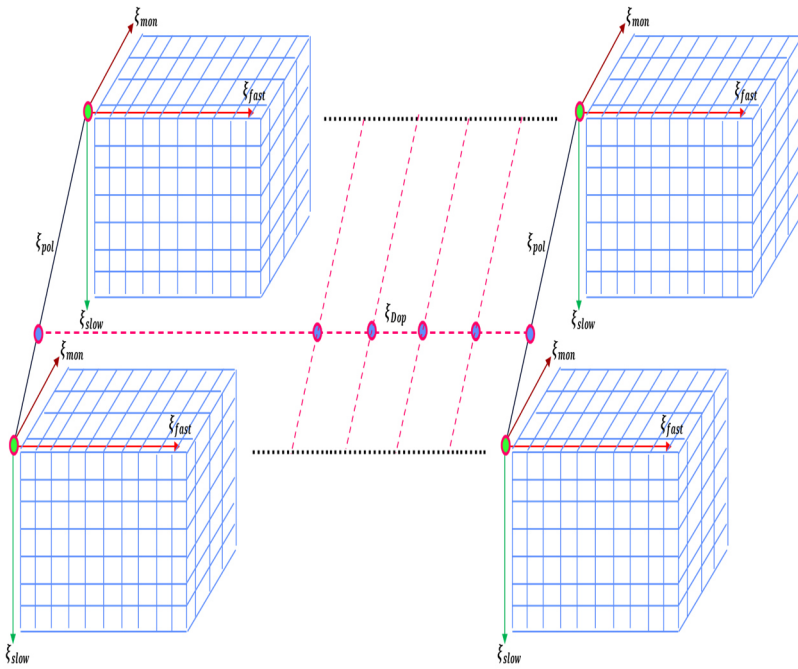


Fig. 2.4. SIMO SBR complex data hyper-cube for SSA during a dwell.

That is, at every dwell the SBR radiation pattern points towards a specific angular direction via the AESA beam controller and acquires raw data which can be organized into a 5-D complex data hyper-cube upstream the MF, i.e.:

- a) The fast-time ξ_{fast} which pertains to the samples acquired during the Sampling Window Length (SWL) within a PRI.
- b) The slow-time ξ_{slow} which indicates the number of transmitted pulses during a dwell.
- c) The monopulse dimension ξ_{mon} which includes the sum Σ , elevation-difference Δ_{el} , azimuth-difference Δ_{az} , and guard *grd* channels.
- d) The receive polarization ξ_{pol} which refers to the horizontal (*H*) and vertical (*V*) receive channels.
- e) The receive Doppler frequency ξ_{Dop} which is related to the number of programmable frequency offsets to be processed in parallel for selecting the most effective PC branch.

For the sake of clarification of Fig. 2.4, the upper left data-cube represents the a) b) and c) dimensions at a given receive polarization and minimum Doppler frequency offset; the lower left data-cube represents the a) b) and c) dimensions at the orthogonal receive polarization and minimum Doppler frequency offset; the upper right data-cube represents the a) b) and c) dimensions at a given receive polarization and maximum Doppler frequency offset; the lower right data-cube represents the a) b) and c) dimensions at the orthogonal receive polarization and maximum Doppler frequency offset.

2.1.2 Low-PRF RRRS and PWS Strategy

Taking into account the aforementioned temporal hierarchies for acquiring complex data hyper-cubes, during a dwell on the order of a few milliseconds (e.g., 2 ms), a set of CUTs cascaded in slant range form an elongated volume of space (spanned by the solid angle of the SBR AESA beam) after transmission of a burst of Linear Frequency Modulation (LFM) waveforms at a Low-PRF (e.g., 2 kHz) and a medium-low transmit duty-cycle. Clearly, in this case a target is range non-ambiguous in the fast-time, and highly Doppler ambiguous in the slow-time. Despite such inherent pulse-to-pulse Doppler ambiguity, a bank of frequency offsets applied in parallel to the echo complex envelope in the fast-time allows enforcing Doppler tolerance on the LFM ambiguity function implemented by a MF. Remarkably, the frequency offset applied to the branch with minimum PC loss at the MF magnitude output in the fast-time cues an estimate of the echo range-rate (embedding the relative radial velocity between the SBR and the debris). In addition, combining multiple samples in the slow-time (e.g., 4 pulses) allows for the build-up of the Signal to Noise Ratio (SNR) before cascading any CFAR-like detection scheme. Such a strategy departs from the high PRF Velocity Search (VS) paradigm indicated in [63] and it is referred to as a Low-PRF RRRS. Furthermore, by suitable design of the temporal hierarchies, a cascade of more than one RRRS allows introducing additional alert-confirm strategies combined with spoiled beams during the search task. It must be stressed that the FoV extent of such a surveillance mode based on a Low-PRF RRRS relies on the AESA transmit peak power as well as on beam shaping and steering capabilities.

Due to the imposing debris velocities, in a post detection scenario a Track While Scan (TWS) approach appears as a

formidable collection strategy over a significant VoI. Interestingly, in a post detection scenario pertaining to a sparsely populated debris environment (as described in chapter 1), the VoI can be immediately reduced in order to initiate an automatic tracking task. A fruitful approach can be characterized by adopting a Low-PRF RRRS in a PWS contacts-collection-strategy during an assumed NCV motion of a debris for an elapse time up to several hundreds of milliseconds. Indeed, despite the hyper-velocity of debris targets, changes in target motions are not expected events unless spawning among colliding debris modify abruptly the trajectory of existing orbital items. That is, considering a dwell time no longer than, say 2 ms, in case a detection via RRRS on a CUT occurs, the SBR finite state machine transitions into Low-PRF RRRS PWS and acquires 4 complex data hyper-cubes during 4 additional dwells (i.e., in less than 8 ms) in a round robin fashion pertaining to the 4 beams surrounding the original beam in which a detection had occurred. Nevertheless, by extending the elapse time to no more than, say 16 ms (whereby the detected target is supposed to move for, say roughly 100 m) it is possible to envisage 8 beams circumscribing in a round robin fashion the original beam in which a detection had occurred. Namely, during the first 4 dwells the SBR acquires the complex data hyper-cubes of the North-West, North-East, South-East, and South-West relative pointing directions, respectively; and then, during the next 4 dwells the SBR acquires the complex data hyper-cubes pertaining to the West, North, East, and South relative pointing directions, respectively. From this point onwards the onboard traker can process measurements as either thresholded or unthresholded data upon one, or more than one, hyper-velocity targets.

2.2 SBR Payload Functional Architecture

This section provides further details on the payload functional architecture in terms of μP and USO, AWG, RF upconversion, AESA subsystem, RF downconversion, multichannel complex envelope acquisition, including ancillary notes on the guard channel.

2.2.1 μP and USO

The digital core of the SBR in Fig. 2.1 implements a general purpose Reduced Instruction Set Computer (RISC) fault tolerant μP (e.g., LEON3FT [64]) whose micro-kernel could be housed on dedicated Programmable Read Only Memory (PROM) and Electrically Erasable PROM (EEPROM) along with specific algorithms and transceiver related constants. In this case, the overall System On Chip (SOC) architecture can be based on a standard, modular and synchronous bus structure: the Advanced Microcontroller Bus Architecture (AMBA) which would result in the “backbone” of the entire configurable and modular SOC architecture with master/slaves communicating entities. Such a hardware-and-software partitioning would allow performing high-speed signal processing tasks of Digital Signal Processing (DSP) slaves on Application Specific Integrated Circuit (ASIC) or Field Programmable Gate Array (FPGA) (e.g., complex envelope extraction, Doppler filter banks and PC in the custom logics), while carrying out advanced low-speed signal processing techniques (e.g., data processor) in software by employing the available μP or, eventually, a coprocessor (e.g., RC64 [65]). Moreover, the μP would control the custom DSP parameters while receiving, through the AMBA bus, proper DSP samples to be further processed in software. It is worth noting that the use of such a high-performance μP embedded in the architecture with

suitable memory hierarchies (see the shared memories and KA mass memory stack in Fig. 2.1) could allow extending the transceiver processing capabilities as a representative example of a novel cognitive instrument devoted to debris detection and tracking applications. In addition, this μP -based approach allows for SBR management and data handling functions with the spacecraft and entails great flexibility in terms of functions, algorithms, and design parameters.

Such an SBR architectural design (and related signal processing techniques) includes a reference USO for generating all the required Local Oscillator (LO) frequencies coherently locked to the USO. Furthermore, without changing the frequency reference of the USO, one may exploit the programmability of advanced Phase Locked Loop (PLL) synthesis to flexibly generate the upconversion and downconversion LOs on the SBR transmit and receive sections, respectively.

2.2.2 AWG

Alongside the μP and USO subsystems, another key subsystem is the AWG in Fig. 2.1 aimed at synthesizing a transmit LFM signal with a flexible programmability, high spectral purity in terms of phase noise and Spurious Free Dynamic Range (SFDR), and high within-pulse and pulse-to-pulse stability. Such a design allows synthesizing the single-pulse waveform directly on a carrier in the Ultra High Frequency (UHF) band (e.g., $f_{\text{UHF}} \sim 500$ MHz) as

$$s_{\text{UHF}}(t) = \mathcal{A} \cdot \cos \left[2\pi f_{\text{UHF}} t + 2\pi \frac{1}{2} K_0 t^2 + \varphi_0 \right] \cdot \text{rect} \left(\frac{t - \mathcal{T}/2}{\mathcal{T}} \right) \quad (2.1)$$

where $\text{rect}(t/\mathcal{T})$ is 1 for $|t| \leq \mathcal{T}/2$ and zero elsewhere. The synthesis of such an LFM waveform can be based on the Direct Digital Synthesis (DDS) approach in [66] with high accuracy

along with an efficient waveform descriptor by only four parameters: start phase φ_0 , start frequency f_{UHF} , LFM slope K_0 , and pulse duration \mathcal{T} (for the sake of completeness, the amplitude parameter \mathcal{A} can be programmed as well).

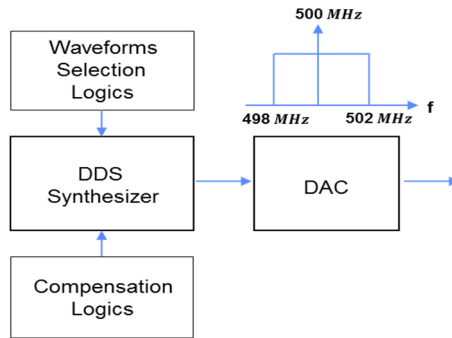


Fig. 2.5. DDS-based waveform generator.

Moreover, the DDS operational behavior may benefit from a number of ancillary signal processing structures including waveform selection logics as well as compensation control logics in order to cope with undesired non-idealities in the transmit stages (Fig. 2.5).

2.2.3 RF Upconversion

A number of strategies can be adopted for translating the UHF LFM radar signal in eq. (2.1) to the K_a -band before being distributed via a power divider to the transmit Analog Beam Forming Network (ABFN) of the AESA antenna. [66] hints, for example, a Single Side Band Modulator (SSBM) based architecture, a PLL based translation loop, or a superheterodyne-based architecture. Due to the limited required operative bandwidth and the necessity of synthesizing spectrally pure waveforms, a superhet architecture based on a double conversion

stage with no need for a \aleph -fold band stretching represents a keystone for proper upconversion with mild Band Pass Filter (BPF) transition bandwidths and phase noise containment. In comparison, this represent a $20 \log(\aleph)$ improvement in phase noise compared to the use of stretching stages for ultra wideband applications. Interestingly, a superhet architecture based on a double conversion stage can further deal with spectral purity demands by relying on a suitable selection of the USO and enforcing phase noise masks and Allan deviation performance [67, 68] directly on the LOs [69]. Fig. 2.6 hints a possible frequency translation relying on a first upconversion stage in the C-Band (e.g., $f_C \sim 5.5$ GHz) and a second upconversion stage in the K_a -band (e.g., $f_{K_a} \sim 35.5$ GHz). Consequently, the K_a -band single-pulse signal input to the transmit power divider can be written as

$$s_{K_a}(t) = \mathcal{A}_1 \cdot \cos \left[2\pi f_{K_a} t + 2\pi \frac{1}{2} K_0 t^2 + \varphi_0 \right] \cdot \text{rect} \left(\frac{t-T/2}{T} \right) \quad (2.2)$$

where the \mathcal{A}_1 parameter also accounts for the tunable output power to properly drive the AESA subsystem transmit lineup.

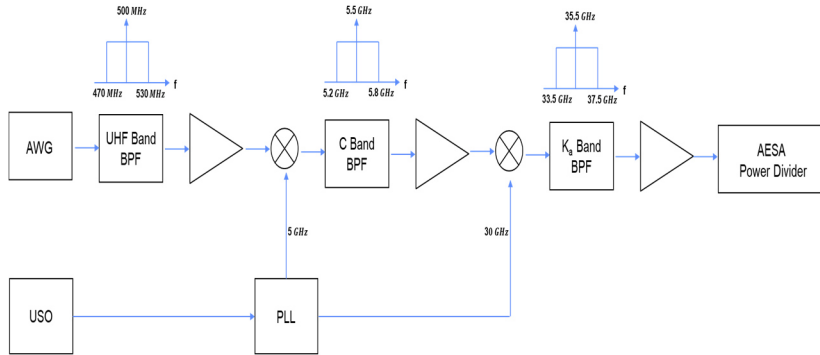


Fig. 2.6. Upconverter frequency plan.

2.2.4 AESA Subsystem

The upconverted signal in eq. (2.2) is distributed from the transmit power divider towards the AESA antenna solid state High Power Amplifiers (HPA) housed within Transmit/Receive (T/R) modules and finally transduced as a single-pulse low-duty-cycle pulsed electromagnetic wave in free space. The electrical-electromagnetic transduction occurs via the AESA radiators within a specific VoI as per the AESA array factor, managed by the SBR beam steering controller in Fig. 2.1. The limited required operative bandwidth of a few megahertz in the K_a -band allows neglecting the adoption of TTDL against frequency dispersion, whereas a wide surveillance VoI needs significant steering angle capabilities in both azimuth and elevation dimensions. Consequently, steering angles larger than 50° with respect to broadside without arising grating lobes do require abandoning subarray grouping of radiating elements on a T/R module, thus mapping one T/R module to each radiating element. While transmit capabilities are required to illuminate a wider FoV with uniform tapering, an additional complexity burden arises on the receive side due to the multichannel monopulse architecture which comprises, for each polarization, the quadruplet sum Σ , delta-elevation Δ_{el} , delta-azimuth Δ_{az} , and guard *grd* channels, each tailored to optimally use a dedicated set of tapering coefficients for beam shaping with a considerable impact on AESA complexity. Accordingly, the amplitude and phase controls of a specific set of T/R modules (feeding radiators which are geometrically displaced on a planar lattice) determine the key characteristics of the AESA directivity in terms of beam-steering, beamwidth, and beamshape. Similar considerations on T/R modules follow on receive, albeit with additional features, constraints, and burdens. That is, echo signals spatially sampled by the AESA radiators are de facto fed (for each H and V polarization) to the T/R modules limiters and Low Noise

Amplifiers (LNAs) (followed by Low Level Amplifiers (LLA) to further increase power dynamics), modulated in amplitude and phase for beam control, and passed through the receive power combiner towards the multichannel downconverter in Fig. 2.2. Indeed, while on transmit a single polarization is deemed sufficient for illuminating the environment for SSA, on receive a dual polarization allows paramount diversity to be further exploited during the debris detection and post-detection processes, especially against gyrotropic effects on signal propagation through plasma slabs as well as electromagnetic scattering from tumbling debris. Fig. 2.7 depicts an AESA radiator (the red-blue square on the left) connected to a T/R module (the transmit branch at the bottom and the receive branches at the top) via a switch (instead of a circulator). The transmit branch (with signal flow from right to left) is characterized by the $\{a_t, \varphi_t\}$, amplitude-phase offsets whereas the receive branches (with signal flow from left to right for both the H and V polarizations) are characterized by the $\{a_\Sigma, \varphi_\Sigma\}$, $\{a_{\Delta el}, \varphi_{\Delta el}\}$, $\{a_{\Delta az}, \varphi_{\Delta az}\}$, $\{a_{\text{grd}}, \varphi_{\text{grd}}\}$, amplitude-phase offsets for the sum, delta-elevation, delta-azimuth, and guard channels, respectively. For the sake of completeness, Fig. 2.7 illustrates the AESA T/R element functional architecture not only for the transmit and receive chains (i.e., radiator elements, active electronics, amplitude and phase modulations) but also in terms of ancillary routings (the brown switches) for mandatory AESA calibration and blanking. Fig. 2.8 completes the functional concept of the monopulse AESA subsystem whereby the whole set of radiators and T/R modules (the red-blue-white rectangles on the left) are linked to the power combiners of the sum, delta-elevation, delta-azimuth, and guard channels (the green rectangles on the right for the V polarization and the beige rectangles on the right for the H polarization), as well as to the power divider of the transmit channel (the orange rectangle on the right).

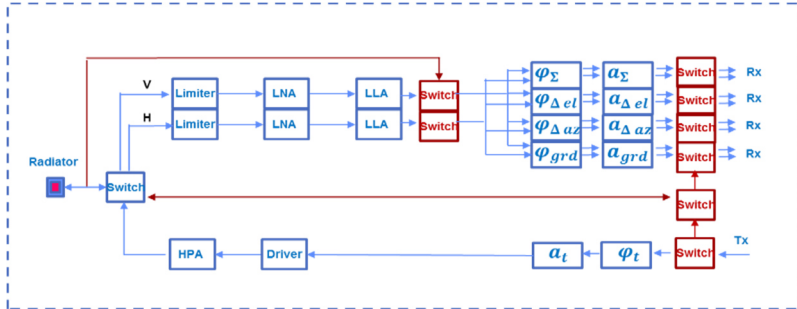


Fig. 2.7. AESA radiator and T/R Element.

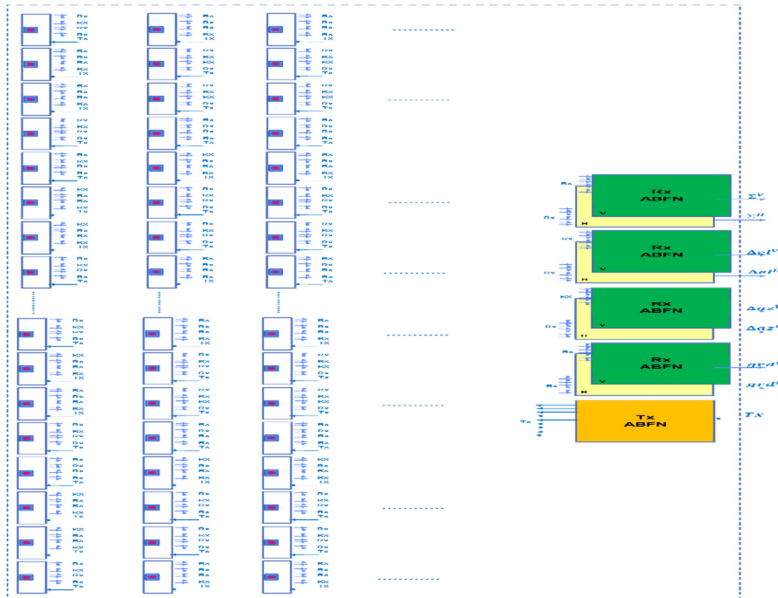


Fig. 2.8. AESA monopulse-based subsystem.

The AESA antenna manufacturing is thus a formidable task per se, as it entails manifold subtleties in terms of electrical, electromagnetic, mechanical, and thermal nuisances which may severely degrade, or rather hamper, the expected beam behaviors

and AESA instrument performance [70,71]. More specifically, the pitch accommodation, the possible mechanical distortion, the amount of mass, the electromagnetic coupling effects, and the heat dispersion combine as a design and development challenge for the radiating elements, the T/R modules, and the ABFN power divider/combiner integration, especially considering the small dimensions linked to the K_a -band operating frequency and the aforementioned demands on the scanning angles. It is also worth mentioning that, albeit the transmit amplifiers operate in slight compression to improve efficiency and avoid arising amplitude modulations, the receive lineup must work linearly to properly exploit Automatic Gain Control (AGC) along the downconversion section in Fig. 2.2 as well as to preserve the superposition of echoes complex envelopes. Furthermore, stacking the AESA radiating elements and feeding two orthogonal polarizations (i.e., H and V in Fig. 2.7) can be based, for example, on a single square horn element radiator with a septum polarizer cascaded with a differential phase shifter implementing an ortho-mode transducer aimed at splitting a signal into two balanced waveguides routes with a reduced cross-polarization coupling [72]. Also, the T/R branches can be based, for instance, on Gallium Nitride (GaN) based Monolithic Microwave Integrated Circuit (MMIC) implementing pseudomorphic High Electron Mobility Transistor (pHEMT) processes with gains roughly more than 30 dB and noise figure of a few dB on the operative bandwidths. Instead of using burdensome circulators, Single-Pole Double-Throw (SPDT) switches can be adopted for signal routing and fast timing control [72]. In addition, the minimum element displacement d on the array lattice has a key influence on the maximum off-broadside scanning angle θ_0 without sprouting grating lobes. For example, let us consider in Fig. 2.9 the geometry of an AESA whose radiating elements appear rectangularly displaced on the \hat{x} , \hat{y} axes with inter-element distance d .

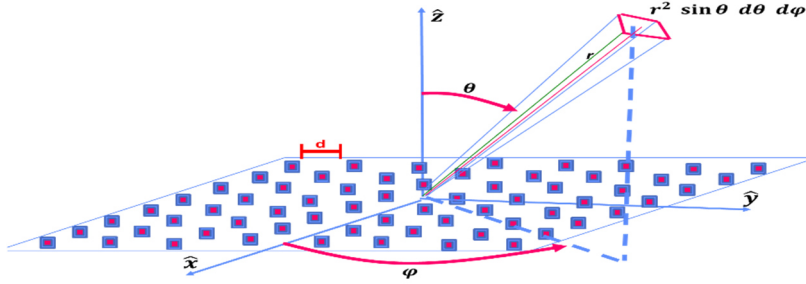


Fig. 2.9. AESA off-broadside angle.

A differential solid angle $d\Omega = \sin \theta d\theta d\varphi$ subtends the differential area $dA = r^2 \sin \theta d\theta d\varphi$ identified by the spherical triplet (r, θ, φ) whereas, in this case, at a given wavelength λ the displacement d limits the ideal off-broadside angle θ_0 from \hat{z} (e.g., excluding degradations due to coupling [70]) as

$$d \leq \frac{\lambda}{1 + \sin \theta_0} \quad (2.3)$$

The bound in eq. (2.3) also cues the scalability of the “*operative angular FoR*” depending on the design and manufacturing of the interelement distance d . In parallel, the scalability of the “*operative range FoR*” depends on the sum of all T/R modules transmit peak power allocated on the AESA. Thus, for a given antenna area one can obtain the SBR total transmit peak power by adding all T/R modules transmit peak powers and, consequently, the directivity and beam solid angle thereof [70]. The plots reported in Figs. 2.10 and 2.11 show the SBR transmit peak power at 35.5 GHz for a set of AESA square-surface areas pertaining to a number of T/R modules (whose lattice interelement spacing attains the upper bound in eq. (2.3) with equality) with respect to several T/R module transmit peak power and maximum off-broadside angle θ_0 without occurrence of grating lobes.

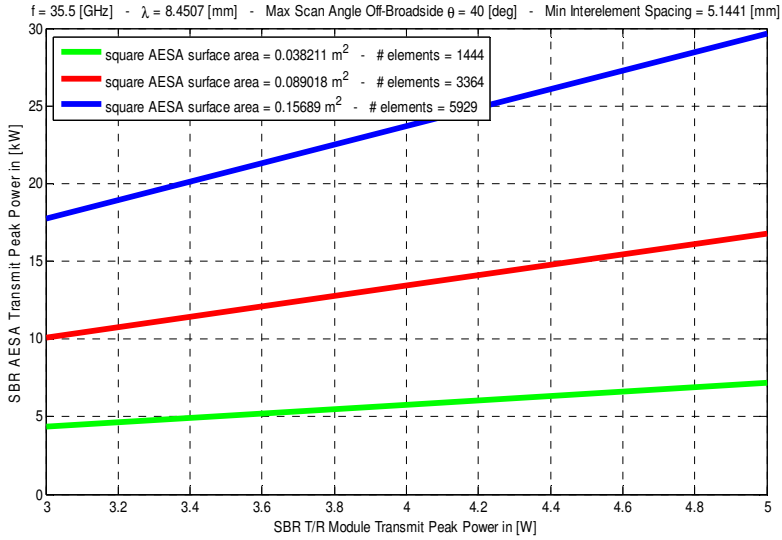


Fig. 2.10. AESA peak power with max off-broadside angle $\theta_0 = 40^\circ$.

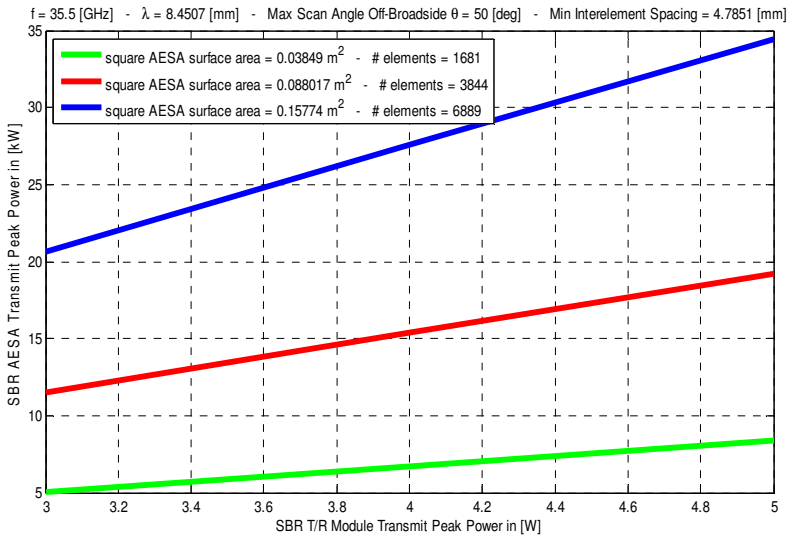


Fig. 2.11. AESA peak power with max off-broadside angle $\theta_0 = 50^\circ$.

Interestingly, Figs. 2.10 and 2.11 highlight several insights on the pros and cons of a K_a -band AESA antenna for debris detection and tracking purposes. Indeed, large operative transmit peak powers could be obtained not by focusing efforts on T/R modules designs with larger and larger transmit peak powers, but rather on tighter inter-element pitch spacing and related T/R modules integration for accommodating an increased number of elements on the lattice (thus relaxing thermal requirements on heat pipes). In this case, a moderate AESA area enlargement would allow for a significantly larger transmit peak power of the SBR whereas smaller element pitch spacing can provide important benefits for the SBR surveillance over larger off-broadside scanning angles without occurrence of grating lobes (e.g., in the aforementioned example a 5.1 mm pitch spacing would allow for a 40° maximum off-broadside angle, whereas a 4.8 mm pitch spacing would allow for a 50° maximum off-broadside angle.) Finally, a dedicated set of complex excitation coefficients for each channel (i.e., each amplitude attenuators and phase shifters addressed as the φ, a cascaded doublet with subscripts in Fig. 2.7) represent a separable (i.e., individual) configurability of the AESA transmit and receive beams ensued from different optimal monopulse radiation patterns (e.g., a uniform tapering on the transmit channel, a Taylor tapering on the receive sum channel, and a Bayliss tapering on the receive difference channels [71]), yet to the detriment of additional AESA complexity. With respect to this latter aspect, modern literature is abundant with unconventional array architectures, topologies, and design methodologies for implementing desired beams with reduced complexities. In general terms, [73] provides a review of clustered, thinned, sparse, and time varying arrays. While legacy monopulse techniques were based on implementing sum and difference channels mostly at RF with a limited number of simultaneous lobing [74], advances in AESA lattice topologies

as well as in array processing in hostile environments have pushed modern monopulse approaches towards digital multichannel adaptive architectures [75]. For ease of design and manufacturing feasibility, the monopulse paradigm proposed in this chapter is framed by the multichannel cardinality in Fig. 2.2 (i.e., 4 RF channels for each receive polarization) whereby simultaneous lobing occurs directly in the K_a -band. From such a standard monopulse scheme at a given CUT, the joint processing of sum and difference channels in the digital domain in Fig. 2.2 is entrenched in Maximum Likelihood Estimation (MLE) (see the covariance-matrix-free estimator in [76, eq. 15] for an individual target which is pulse-to-pulse fluctuating, or see the covariance-matrix-based estimator in [77, eq. 13] for an individual target).

Within this framework, for monopulse radar applications [78] indicates convex-optimization-based approaches aimed at sharing common weights on the periphery of the array while maintaining independent excitations of sum and difference channels in the rest of the array. As a remarkable step forward, [79] proposes a compromise solution which maximizes the directivity of the sum pattern subject to several constraints (including one on the slope of the difference patterns) and sharing the excitation coefficients of the sum and difference patterns. Accordingly, a number of possible AESA layout quadrant lattices layouts boundaries arise as pertaining to monopulse constraints on the AESA amplitude-phase offsets represented by the complex excitation coefficient I_{lm} positioned on the discrete lattice of Fig. 2.9 in the \hat{x}, \hat{y} plane as per the subscript lm . That is, the Array Factor (AF) for a planar AESA centered in the \hat{x}, \hat{y} plane (see Fig. 2.9) with an even number of elements $2L'$ on the \hat{x} axis and $2M'$ on the \hat{y} axis can be written as

$$AF(u, v) = \sum_{l=1}^{2L'} \sum_{m=1}^{2M'} I_{lm} e^{j\frac{2\pi}{\lambda}[(l-L'-\frac{1}{2})d_x u + (m-M'-\frac{1}{2})d_y v]} \quad (2.4)$$

where $u = \sin \theta \cos \varphi$, $v = \sin \theta \sin \varphi$ are the directional cosines; d_x, d_y are the lattice interelement spacing along the \hat{x}, \hat{y} axis, respectively; $I_{lm} = a_{lm} e^{j\varphi_{lm}}$ with a_{lm} and φ_{lm} representing the amplitude and phase of the complex excitation coefficient I_{lm} , respectively, such that, in a nonhostile environment, the φ_{lm} terms are used to set the beam scanning towards the direction (u_0, v_0) as per the phase shifts $\varphi_{lm} = -\frac{2\pi}{\lambda} [(l-1)d_x u_0 + (m-1)d_y v_0]$. Following [78] for instance and considering a square lattice (i.e., $d_x = d_y$, and $L' = M'$), one may then impose quadrant symmetry constraints on the whole set of monopulse-based a_{lm} i.e., $a_{t_{lm}}, a_{\Sigma_{lm}}, a_{\Delta_{el_{lm}}}, a_{\Delta_{az_{lm}}}$, and $a_{\text{grd}_{lm}}$.

2.2.5 RF Downconversion

Another variety of strategies can be adopted for translating the K_a -band LFM radar echo signal from the receive power combiner output (from each H, V polarization and from each $\Sigma, \Delta_{el}, \Delta_{az}, \text{grd}$ monopulse sum, delta-elevation, delta-azimuth, and guard channel, respectively) into the downconverter subsystem in Fig. 2.2 all the way down to a suitable Intermediate Frequency (IF) before feeding the digital section. For example, an interesting multichannel architecture relies on a modular approach where the whole set of monopulse channels can be assigned to work under the shared control of an AGC loop providing the instrument dynamic range with over 50 dB of gain control while the receiver chain applies a double-conversion superheterodyne scheme [80]. The use of a double-conversion configuration is caused by the difficulties of applying an Analog to Digital Converter (ADC) directly at such high frequencies, whereas a single conversion would inevitably hamper image frequency rejection. In addition,

a double-conversion would allow spreading the gain control over larger sections of the receiver. Fig. 2.12 indicates a possible frequency translation relying on a first downconversion stage in C-band (e.g., $f_C \sim 5$ GHz) and a second downconversion in the High Frequency (HF) band (e.g., $f_{HF} \sim 25$ MHz). Without lack of generalization, the proposed frequency plan in Fig. 2.12 assumes a K_a -band BPF centered at 35.515 GHz in order to exploit integer- N PLLs for downconversion to a fixed IF frequency centered at 25 MHz. For the sake of clarification, if compared to the transmit frequency plan centered at 35.5 GHz in Fig. 2.6, the additional 15 MHz is an agile programmable task on the AWG. Moreover, it is worth noting that the IF filter in the HF Band in Fig. 2.12 has a slightly larger percentage of bandpass compared to the other BPFs in order to accommodate variable operative bandwidths, and could be based on Surface Acoustic Waves (SAW) devices implementing anti-aliasing functions before the signal is digitized.

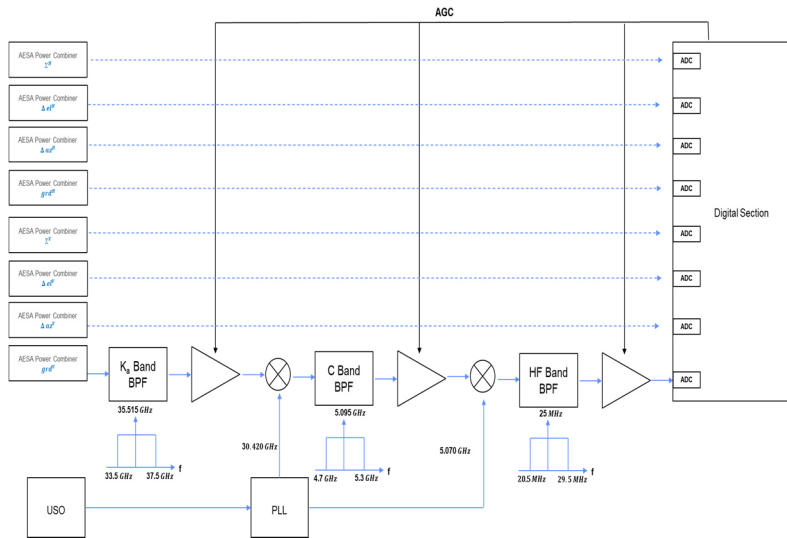


Fig. 2.12. Downconverter frequency plan.

2.2.6 Multichannel Complex Envelope Acquisition

The receive digital section in Fig. 2.2 is based on harmonic-sampling the IF signal using a single ADC for each channel and producing I/Q samples without phase and amplitude imbalances of a quadrature analog demodulator. Considering relative SBR-debris velocities discussed in § 1.4.3, the HF single-pulse (noiseless) echo signal at a given ADC input (see Fig. 2.12) for a point-like target with a τ_r delay as well as with a f_d Doppler offset is fed as input to the digital section as per the following real signal

$$s_{HF}(t) \sim D \cdot \cos \left[2\pi(f_{HF} + f_d)(t - \tau_r) + 2\pi \frac{1}{2} K_0 (t - \tau_r)^2 + \varphi_0 \right] \text{rect} \left(\frac{(t - \tau_r) - \mathcal{T}/2}{\mathcal{T}} \right) \quad (2.5)$$

The single pulse point-like target echo approximation in eq. (2.5) is obtained by neglecting the scaling of the amplitude and the stretching of the time axis by the $\gamma_d = 1 + f_d/f_{Ka}$ factor (see § 1.4.3), and abides by space-time factorability [81]. For the sake of clarification, a brief digression follows for both aspects. As stressed in § 1.4.3, eqs. (1.27)-(1.28) provide key bounds (as per [49] and [50]) for employing either a narrowband or wideband representation of the signal and, consequently, of the signal ambiguity function for estimating range and range-rate parameters in a CUT. During limited time spans on the order of a second, debris detection and tracking can be tackled assuming a NCV model for both the SBR and debris motion models. In this case, with a PRF on the order of a few kHz, a low transmit duty cycle, and a few megahertz of bandwidth \mathcal{B} , the inequalities in eqs. (1.27)-(1.28) are both attained even for extremely fast micrometeoroids. Indeed, $\dot{v} \cong 0$ by the NCV assumption whereas, even by considering a micrometeoroid flying at an imposing 70 km/s relative radial velocity v with respect to the SBR, for a 5-MHz-bandwidth \mathcal{B} and a 50- μ s-pulse-duration \mathcal{T} eq.

(1.27) results in $0.06 \ll 1$. Interestingly, taking into account a 16 km/s relative velocity v with a 2.5-MHz-bandwidth \mathcal{B} eq. (1.27) still holds as $0.27 \ll 1$ when replacing the 50- μ s-pulse-duration \mathcal{T} with a 2 ms CPI. Therefore, the adoption of a narrowband signal model for range and range-rate parameters estimation entails neglecting the γ factor for all Doppler terms pertaining to the received echo analytical representation in (2.5) with the exception of the carrier phase term. In parallel, the additional modeling aspect on the point-like target echo in eq. (2.5) pertains to pondering its space-time factorability [81] (i.e., considering the x, y variables, the x - y factorability of a function $f(x, y)$ results in $f(x, y) = f_1(x)f_2(y)$). For an SBR with an AESA with 1-D dimension L_a (i.e., either along the \hat{x} or, equivalently, the \hat{y} axis in Fig. 2.9), the condition on the uncoupled representation of the temporal and spatial terms in the point-like target echo for analog beamforming within the AESA subsystem would ensue as sufficient condition (see for instance [81, eq. (18)])

$$\frac{L_a}{c} \ll \frac{1}{\mathcal{B}} \quad (2.6)$$

which in our narrowband case holds for an AESA with a 1-D dimension up to several tens of meters (e.g., for a square AESA with 1-D dimension L_a of 3 m and a bandwidth \mathcal{B} of 5 MHz the condition in eq. (2.6) results in $0.05 \ll 1$). Indeed, the condition in eq. (2.6) allows neglecting the use of TTDL (see [81, eq. 19-21]) in favor of phase-shifts. Beside the AESA subsystem, the digression on space-time factorability is in a subtle way still intertwined within eq. (2.5) with profound implications for the possible non ambiguous estimates of parameters embedded within the observables. Indeed, considering the point-like target echo acquired from the AESA main beam, the target range-rate parameter v_{target} would be ambiguously embedded in $f_d = -2v/\lambda$ in eq. (2.5) due to the inherent coupling between the

mutually unknown radial target velocity v_{target} and SBR velocity v_{SBR} , i.e., $v = v_{SBR} - v_{target}$. As a by product, this would imply the lack of factorability of the SBR ambiguity function into separate spatial and temporal ambiguity functions (see [81, eqs. 10 and 48]). For example, Fig. 2.13 depicts three scenarios with ambiguities arising from several mutual AESA and target radial velocities configurations (i.e., purple arrows) leading to the same relative AESA-target radial velocity $v = v_{SBR} - v_{target}$ (i.e., green arrow) whereby an outward target motion is defined as positive (i.e., $v_{target} > 0$).

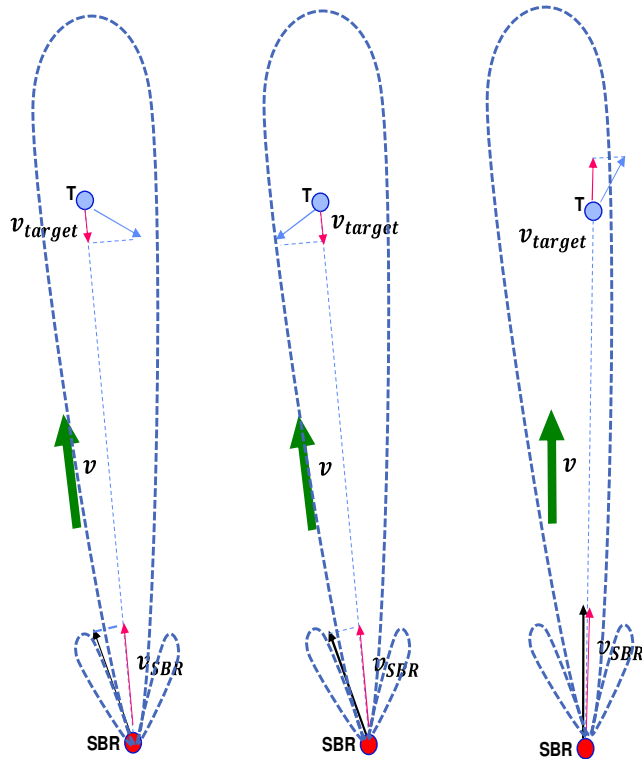


Fig. 2.13. Target range-rate ambiguities embedded in f_d .

By abandoning the intent to design an onboard tracker which bases its inference on target range-rate estimates, it is possible to define a resolution cell for a parameter vector made of range, azimuth angle, elevation angle, and amplitude. In this specific case, depending on the proper design of a low sidelobe radiation pattern as well as on the guard channel radiation pattern lying strictly above the sidelobe pattern, the signal in eq. (2.5) can be modeled as factorable in space-time. Then, the CUT can be factored into its angular components (i.e., azimuth angle and elevation angle) and temporal components (i.e., delay and amplitude). Downstream such a clarification, the parameter D in eq. (2.5) can be factored into an angular component (i.e., the array factor in eq. (2.4)) and its temporal component (i.e., the point-like target echo amplitude occurring at a τ_r delay.)

Now, the separation of I/Q samples from eq. (2.5) can be efficiently obtained by sampling the HF signal centered at 25 MHz with a 20 MHz ADC (thus handling the HF passband in Fig. 2.12) and multiplying the ADC output by the 1,0,-1,0,... sequence and 0,-1,0,1,0,... sequence for the I and Q branches, respectively, followed by an Integrate & Dump (I&D) Low Pass Filter (LPF) [82]. Remarkably, due to the imposing f_d Doppler offset with respect to the required operative bandwidth of a few megahertz, at every range gate s it is possible to deal with the inherent limits of Doppler tolerance of the LFM-based ambiguity function. In particular, a set of filter banks, each bearing a dedicated frequency offset f , allows estimating within-pulse the echo Doppler frequency f_d from the branch with minimum MF magnitude response loss (as cued by the branch with maximum modulus value obtained after the noncoherent combining of a train of echoes at the MF output.) Such a design structure relies on an ADC with at least 14 bits (or, eventually, 16 bits [83] for managing an even larger instantaneous power dynamics) as well as on efficient COordinate Rotational DIgital Computer (CORDIC) [84] for phase rotators driven by Numerically

Controlled Oscillators (NCO) with a frequency offset granularity on the order of 100 kHz. For a given Doppler offset f driving the NCO, and range gate s within the SWL, Fig. 2.14 represents such a bespoke MF which is a key structure to be employed to form the SBR complex data hyper-cube. More specifically, the aforementioned modulus value of the MF output after a suitable noncoherent combining is indicated as $z_{s,f}$ whereas the MF complex output (i.e., $z_{I_{s,f}}$ and $z_{Q_{s,f}}$) can be further processed within the receive digital chain. A proof of concept for the basic onboard processing structure indicated in Fig. 2.14 is shown in Fig. 2.15 through Fig. 2.20. That is, Fig. 2.15 sketches a simulated point-like target echo at ADC output at a given range gate s with a 4-dB SNR and a 1-MHz-bandwidth \mathcal{B} along with a Doppler frequency f_d of roughly 2.5 MHz. In particular, Fig. 2.15 a) and Fig. 2.15 b) represent the temporal and spectral echo behavior, respectively, whereby (without lack of generality) the temporal reference system is centered at the true target delay. After enforcing a suitable Doppler offset f , Fig. 2.16 reports the noncoherent combining output $z_{s,f}$, built upon a burst of 4 echoes with interleaved upchirp-downchirp LFM waveforms, i.e., in Fig. 2.16 a) the linear magnitude on odd pulses; in Fig. 2.16 b) the linear magnitude on even pulses; in Fig. 2.16 c) the dB magnitude on odd pulses; in Fig. 2.16 d) the dB magnitude on even pulses. Clearly, an interleaved upchirp-downchirp LFM waveforms burst-transmit-strategy is enticing per se, as it allows soothing the LFM-inherent range estimation bias and squelching even-time-around echoes, if any.

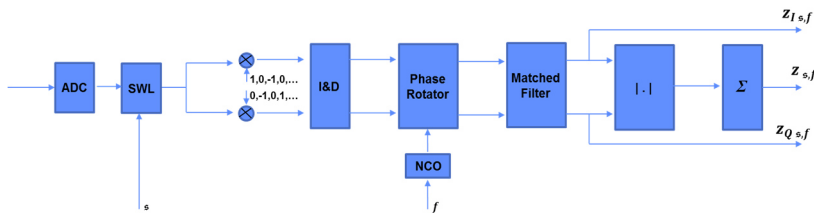


Fig. 2.14. Bespoke MF with Doppler offset f and range gate s .

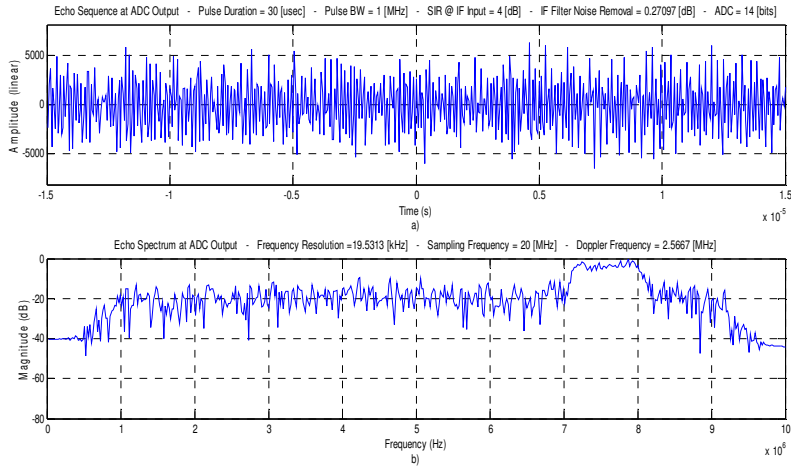


Fig. 2.15. Point-like target echo at ADC output at a given range gate s . a) temporal echo; b) spectral echo.

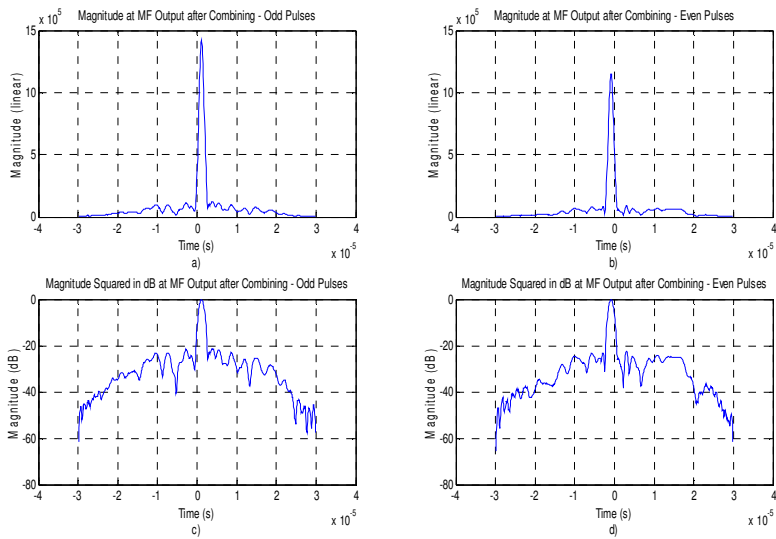


Fig. 2.16. $z_{s,f}$ in case of a negligible residual echo Doppler offset. a) linear magnitude on odd pulses; b) linear magnitude on even pulses; c) normalized dB magnitude on odd pulses; d) normalized dB magnitude on even pulses.

For the sake of clarification of the digital receiver lineup, Fig. 2.17 shows the aforementioned simulated point-like target echo behaviors, i.e., temporal echo in Fig. 2.17 a) and spectral echo in Fig. 2.17 b) at the phase rotator input of Fig. 2.14. Interestingly, the mild echo image at roughly -2.5 MHz also appears (distorted and attenuated) due to digital mixing and I&D transfer function with respect to the useful echo at roughly 2.5 MHz. Figs. 2.18 and 2.19 depict the echo appearance (i.e., temporal echo in Figs. 2.18 a) and 2.19 a) and spectral echo in Figs. 2.18 b) and 2.19 b)) downstream the phase rotator output when either a suitable or unsuitable Doppler offset f is applied, respectively. That is, while in Fig. 2.18 the residual echo Doppler offset appears successfully enforced to fit within a ± 50 kHz frequency span and, therefore, is suitably tolerated by the MF center frequency at 0 Hz, in Fig. 2.19 the residual echo Doppler offset is much larger (i.e., roughly 1.9 MHz) and, therefore, unbearable by the MF.

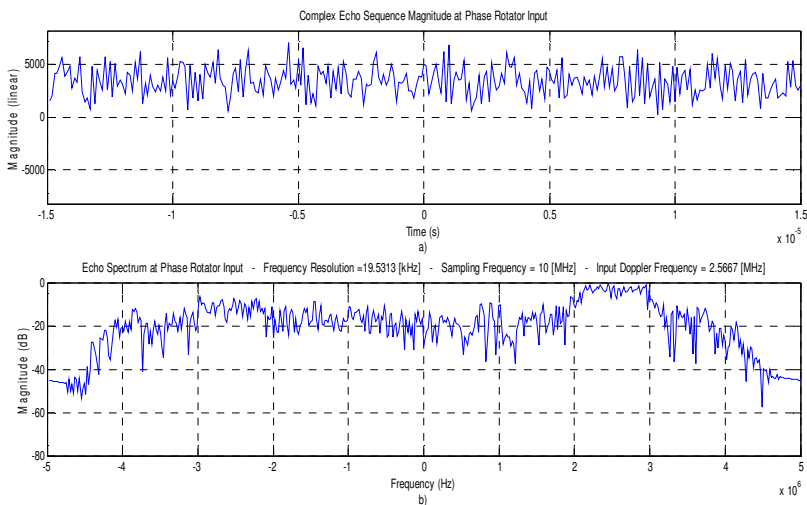


Fig. 2.17. Point-like target echo at phase rotator input. a) temporal echo; b) spectral echo.

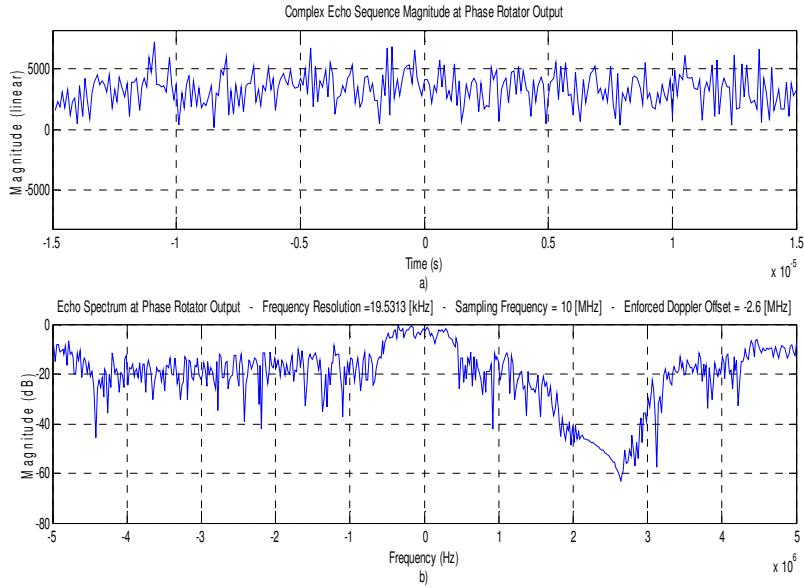


Fig. 2.18. Point-like target echo at phase rotator output (suitable Doppler offset). a) temporal echo; b) spectral echo.

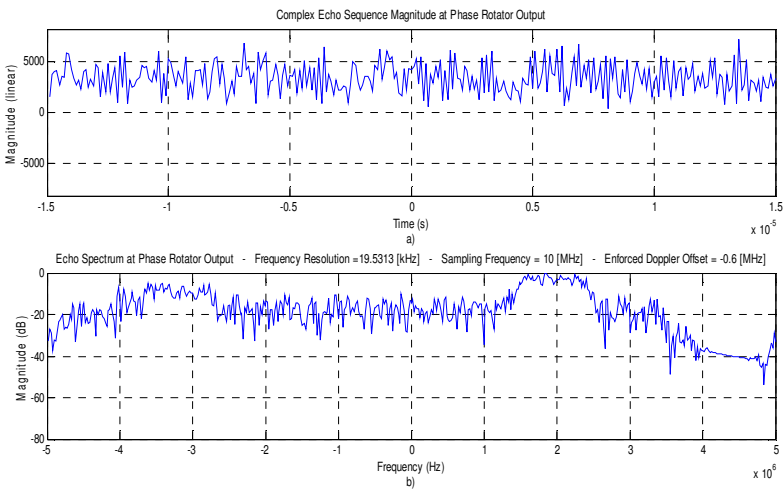


Fig. 2.19. Point-like target echo at phase rotator output (unsuitable Doppler offset). a) temporal echo; b) spectral echo.

Indeed, in case of a significant residual echo Doppler offset, the MF output degradation is evident in Fig. 2.20 (with a residual echo Doppler offset of roughly 1.9 MHz) with respect to the example depicted in Fig. 2.16 (with a residual echo Doppler offset of roughly -30 kHz). Again, Fig. 2.20 reports the noncoherent combining output $z_{s,f}$, built upon a burst of 4 echoes with interleaved upchirp-downchirp LFM waveforms, i.e., in Fig. 2.20 a) the linear magnitude on odd pulses; in Fig. 2.20 b) the linear magnitude on even pulses; in Fig. 2.20 c) the dB magnitude on odd pulses; in Fig. 2.20 d) the dB magnitude on even pulses.

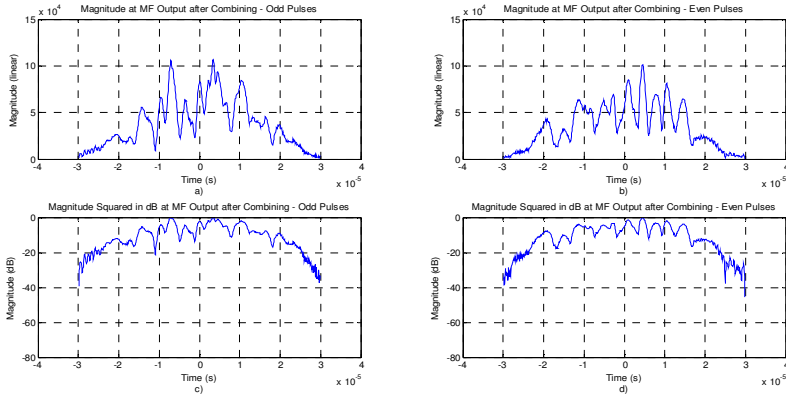


Fig. 2.20. $z_{s,f}$ in case of a significant residual echo Doppler offset. a) linear magnitude on odd pulses; b) linear magnitude on even pulses; c) normalized dB magnitude on odd pulses; d) normalized dB magnitude on even pulses.

The simulation results presented in Figs. 2.15-2.120 are solely aimed at stressing the controllable Doppler tolerance of the transceiver complex envelope acquisition scheme. Thus, further echo acquisition variabilities and inherent degradations due to endogenous (e.g., phase noise [85,86] and numerical quantization [87]) and exogenous (e.g., channel scintillation and target scattering assumptions impairments) are outside the scope of this chapter.

Clearly, the effectiveness of a target echo extraction during a dwell via the signal processing chain in Fig. 2.14 relies on the availability of a suitable Doppler offset f and range gate s . However, these quantities are unknown and, to overcome this shortcoming, the bespoke MF structure in Fig. 2.14 is replicated in Fig. 2.21 for a set of programmable Doppler offsets f (i.e., applied in the horizontal dimension in Fig. 2.21 between the f_{min} and f_{max} values) and a set of range gates s (i.e., applied in the vertical dimension in Fig. 2.21 between the s_{min} and s_{max} values), thus paving the way for target echo extraction within the environmental scenario during a dwell.

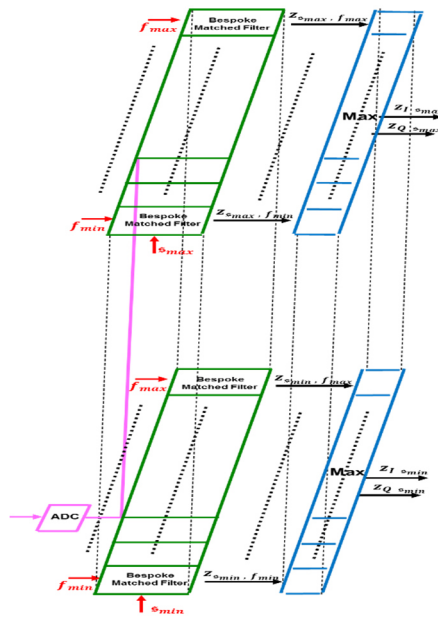


Fig. 2.21. Bespoke MF for all Doppler offsets f and range gates s .

Finally, the 8 monopulse channels implementing the bespoke MF for all Doppler offsets and range gates upstream the CFAR block is depicted in Fig. 2.22.

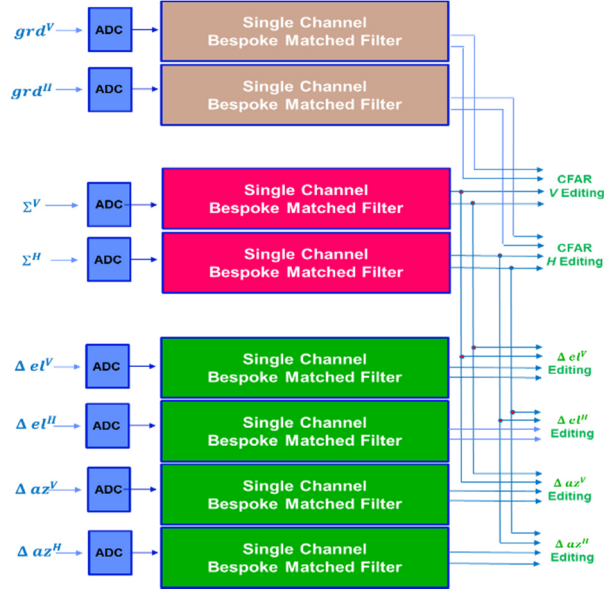


Fig. 2.22. Multi-channel bespoke MF structure.

In this case, for both the H and V polarizations, the grd and the Σ channels are routed to the CFAR-like block. The CFAR-like block in Fig. 2.2 includes a decision rule whose detection threshold for a given false alarm probability is (possibly) independent of the nuisance parameters variability. This is aimed at enforcing robustness in the binary-hypothesis test whereby the probability density function (pdf) under the noise-only hypothesis is independent of nuisance parameters. In our case, beside the target echo Doppler frequency f_d , additional nuisance parameters variability accounts for the system temperature change (in case the antenna radiation pattern is pointed towards either the Sun, the Earth, or the outer space) or the event of an imposing echo return spike from a large clutter discrete (e.g., from an orbital infrastructure).

Interestingly, considering that the building blocks in Fig. 2.14 represent those basic fixed functions that enable the

formation of the complex data hyper-cube, the use of a space qualified 28 nm ASIC [88] appears as an interesting solution for implementing the multichannel structure represented in Fig. 2.22. On the contrary, a programmable FPGA according to possible evolving ameliorations can represent a viable design paradigm for the CFAR-like block as well as for the implementation of dedicated editing functionalities such as the *grd* channel based excision-control-logics.

Finally, the data processor in Fig. 2.2 can be a software-based functionality for tracking purposes, along with support editing transformations such as the target delay-range conversion for the Σ channel, monopulse angular conversion Look Up Tables (LUT) for the Δ_{el} and Δ_{az} channels jointly with the Σ channel for gain normalization, and attributes formation for unresolved detection of closely spaced targets [89,90].

2.2.7 Notes on the Guard Channel

The structure in Fig. 2.2 includes the implementation of editing functionalities in terms of outliers-excision control-logics exploiting the guard-channel for Side Lobe Blanking (SLB). A comparison occurs between the signal from the pencil beam of the sum channel and the signal from the broader beam of the guard channel to discern if the echo derives from a signal in the main beam or from the sidelobes of the sum channel. Ideally, the broad beam pattern of the guard channel should lie above the pencil beam sidelobe pattern of the sum channel. The control-logics for the outliers-excision is outside the scope of this work. In simple terms, when the sum channel decides for a detection in a CUT, the detection is blanked if the guard channel statistic is larger than the sum channel statistic (see [91] and [92]). In this case, chances are that the tentative detection in the sum channel is being triggered by the presence a clutter discrete in the sidelobes.

Chapter 3

Effects of Plasma Media With Weak Scintillation on the Detection Performance of SBRs

As stressed in chapter 1, depending on the solar activity (and considering the scintillation index s_4 [22,27] as a measurable parameter to be exploited in a KA paradigm), an operative SBR for SSA entails propagation of waveforms either through free space vacuum or, alternatively, through both free space vacuum and slabs of turbulent plasma. Within this framework, radar detection schemes for SSA can be adopted relying on the Neyman Pearson (NP) criterion which maximizes the probability of detection P_D as a function of SNR for a given probability of false alarm P_{FA} [40,93-95]. Eventually, when the NP detector is not Uniformly Most Powerful (UMP) [96], the decision problem can be tackled via conventional detectors implementing a Generalized Likelihood Ratio Test (GLRT) [94,95]. In any case, the performance analysis of conventional radar detectors in plasma media is quite limited (e.g., see [27]), especially for SSA from a SBR system perspective. Indeed, most state of the art radar systems for SSA have been contrived as ground-based radars [7,9,97]. Moreover, several efforts on the performance analysis of conventional detectors in plasma media have been dealing with the ionosphere acting as a waveguide in the HF Band, e.g., Over The Horizon (OTH) radars [98]. On the other side, previous analyses for SBR detection performance in plasma media have considered Rayleigh target fluctuation jointly with Rayleigh

plasma scintillation [99,100] and were predominantly based on Monte Carlo methods [101]. Such analyses have been further extended in [102] taking into account decorrelation effects among the pulses whereas [103] summarized Rayleigh scintillation-induced integration losses.

Interestingly, in this work the performance analysis of conventional radar detectors in AWGN for both coherent and noncoherent pulse trains (see [95, Ch. 1 and 2]) is extended to include both Rayleigh and Rice target fluctuations jointly with Rice plasma scintillation as a function of the scintillation index s_4 . Remarkably, such a performance analysis is novel and represents a useful reference framework for tuning the SBR transceiver addressed in chapter 2, thus accounting for debris scattering fluctuations as well as signal propagation in plasma media in case of weak scintillation.

The rest of the chapter is organized as per the following Sections. Section 3.1 resumes physical insights leading to reasonable statistical models for the performance analysis of conventional detectors in SSA operative scenarios (including the Fading Occurrence Probability (FOP) in case of weak scintillation). Section 3.2 deals with analytic expressions for the performance analysis of conventional radar detectors in AWGN for both coherent and noncoherent pulse trains in case of either nonfluctuating, Rayleigh, or Rice target fluctuations. Section 3.3 extends the performance analysis via semi-analytic techniques including Rice plasma scintillation effects on signal propagation as a function of the scintillation index s_4 . Section 3.4 outlines a brief digression on the performance analysis in case of bistatic radar configurations.

3.1 Phenomenology-Based Statistics

In this section, the physical mechanisms inducing channel and target fluctuations are resumed as addressed in chapter 1. In particular, they are pondered in order to introduce suitable statistical models for the performance analysis of conventional radar detectors for SSA in AWGN in case of weak plasma scintillation. The aforementioned reasoning leads to consider Rician statistics for the channel phenomenology along with either Rayleigh or Rician statistics for the target phenomenology. In addition, a sensitivity analysis provides proof for the FOP in case of weak scintillation as a function of the scintillation index s_4 .

3.1.1 Reasonable Statistical Models for Channel-Target Phenomenology

As hinted in chapter 1, plasma media can significantly perturb the propagation of electromagnetic waves, thus affecting radar detection and tracking capabilities for SSA. Specifically, in chapter 1 it was stressed that a weak plasma turbulence allows simplifying the propagation model of an electromagnetic wave through a plasma slab predominantly as a forward scattering mechanism around a small cone with negligible attenuation and backscattering within the cone itself (thus excluding multiple scattering effects in the plasma slab). In this case, it is reasonable to assume a flat-flat channel during a short radar burst on a small bandwidth in which a fixed multiplicative complex term affects the complex envelope of the radar signal (see also [27, Ch. 3]).

To this end, the aforementioned multiplicative complex scintillation process at a given time t has been formulated as per the complex r.v. in eq. (1.7), i.e., $Be^{j\phi}$, where the pdf of B is Rice as per eq. (1.8) with Rice factor $r_b = b_0^2/2\sigma_b^2$, and the pdf of ϕ is uniformly distributed in $(-\pi, \pi]$. Moreover, taking into

account eq. (1.7), it was remarked that by enforcing randomness also on φ_0 as a uniformly distributed r.v. in $(-\pi, \pi]$ and statistically independent of B_R and φ_R , B and φ become statistically independent.

On the other side, for target phenomenology (considering scattering mechanisms at a given λ to occur close to the high-frequency optical region), when the radar transmits an electromagnetic waveform impinging on the external surface of a debris target, the main scattering responses have been assumed to derive chiefly from randomly positioned items. Accordingly, the RCS of a debris target σ_{RCS} has been formulated as per eq. (1.19). To this end, as clarified in chapter 1 the single debris item may possibly induce RCS fluctuations per se depending on the aspect angle (since the coherent reflectivity of a debris is surely influenced by the electromagnetic roughness and relative permittivity of the constituents materials). Nevertheless, additional fluctuations may derive from either a debris cloud or from a single debris (possibly characterized by one or more scattering centers) with peaks and nulls depending on the occurrence of a 0 or π phase offset, respectively, among the relevant scattering items in eq. (1.19).

Clearly, such a reasoning induces the need for statistical modeling of target fluctuations in order to analyze the performance of radar detectors. Indeed, early analyses of radar detection performance from K echo return samples in AWGN comprised nonfluctuating targets with a deterministic RCS (see Marcum [104]) as well as targets with some specific RCS fluctuation laws (see Swerling [105]). Predominantly, the fluctuation of the RCS has been characterized in terms of first order statistics of individual samples along with correlation properties among the K samples. Representative examples of families for first order statistics include the gamma, Rice-square, Weibull, or log-normal distributions (see [40],[93-95], and [106-108]). On the other side, correlation properties among the K

samples comprise fully correlated samples (i.e., scan-to-scan fluctuations), fully uncorrelated samples (i.e., pulse-to-pulse fluctuations), as well as partial correlation thereof ([40],[93-95], and [109-111]). In particular, the well known Swerling models for target fluctuations [105] can be summarized as follows. The Swerling 0 model (also known as the Marcum model [104]) represents a nonfluctuating target. The Swerling I and II models represent first order statistics of the RCS via a central chi-square distribution with 2 degrees of freedom (i.e., an exponential distribution which is a particular case of a gamma distribution) along with scan-to-scan and pulse-to-pulse fluctuations, respectively. The Swerling III and IV models represent first order statistics of the RCS via a central chi-square distribution with 4 degrees of freedom (i.e., once again a particular case of a gamma distribution) along with scan-to-scan and pulse-to-pulse fluctuations, respectively. In fact, modern radar detection performance analysis represents target fluctuation power relying extensively on the gamma distribution [107,112]. For example, a target fluctuation power modeled by a gamma r.v. G with shape parameter $\alpha \geq 0$ and statistical mean Ω (i.e., $\mathbb{E}[G] = \Omega$) via the pdf [31]

$$P_G(g|\alpha, \Omega) = \frac{1}{\left(\frac{\Omega}{\alpha}\right)^\alpha \Gamma(\alpha)} e^{-\frac{g}{\left(\frac{\Omega}{\alpha}\right)}} u(g) \quad (3.1)$$

can be exploited to compute the performance of conventional radar detectors from a temporal burst of K echo sample returns in AWGN for Swerling I-II-III-IV models.

Now, Swerling I and II models can be useful for scenarios assuming that a target RCS is made up of the superposition of scattering responses such that no response is dominant compared to the others. On the contrary, Swerling III and IV models can be

useful approximations [106,108] for scenarios assuming that a target RCS originates from the superposition of scattering responses such that one of them is dominant compared to the other minor contributions (to this end, see also [113] where a chi-square pdf with 4 degrees of freedom is used to model RCS fluctuations whose dominant-to-minor scatterers ratio is $1 + \sqrt{2}$). In this latter scenarios, a Rice squared r.v. G (i.e., $G = D^2$ where the pdf of D is Rice with parameters q and σ^2) characterized by the Rice factor r of D (i.e., $r = q^2/2\sigma^2$) and statistical mean Ω (i.e., $\mathbb{E}[G] = \Omega = q^2 + 2\sigma^2$) provides an exact and more general statistical description of RCS fluctuations [114,115] for targets whose RCS stems from the superposition of a dominant deterministic scattering power, q^2 , and a minor zero-mean stochastic power, $2\sigma^2$. In this case, the pdf of G is

$$P_G(g|r, \Omega) = \frac{1+r}{\Omega} e^{-r} e^{-\frac{(1+r)g}{\Omega}} I_0\left(2\sqrt{\frac{r(1+r)g}{\Omega}}\right) u(g) \quad (3.2)$$

It is also worth mentioning that as $r \rightarrow 0$ the Rice distribution tends to the Rayleigh distribution and, therefore, it allows representing the Swerling I and II models. In addition, as $r \rightarrow \infty$, one obtains the Swerling 0 model as well. Definitely, when the RCS of the dominant non fluctuating component is approximately 75% [115] of the total RCS, the dissimilarity (in the Kullback-Leibler sense) between Swerling III-IV targets and Rice Targets (see [115, eq. (16)]) is minimized.

3.1.2 Sensitivity Analysis and FOP in Case of Weak Scintillation

The aforementioned physical mechanisms inducing channel and target fluctuations pave the way for characterizing the power of a target echo in terms of three multiplicative components, namely,

- a deterministic component pertaining to the radar equation [40] assumed known by suitable radar design and calibration;
- a Rayleigh or, alternatively, a Rice based component accounting for the fluctuation of the RCS [36];
- a Rice based component related to the fluctuation of the two-way channel propagation [19] in a monostatic configuration.

In particular, for a monostatic radar configuration let us consider an antenna with gain G_a at a given λ , radiating a peak power P_T at a distance R in the Fraunhofer region as per eq. (1.20). Accordingly, a backscattered echo power is intercepted by the radar effective antenna area $A_{eff} = G_a \lambda^2 / 4\pi$ such that (including instrument losses L_l) the echo receive power P_R is

$$P_R = \left[\frac{P_T G_a^2 \lambda^2 \overline{\sigma_{nom}}}{(4\pi)^3 L_l R^4} \right] \times \left[\frac{\sigma_{RCS}}{\overline{\sigma_{nom}}} \right] \times [X^4] \triangleq P_{Ro} \times G \times Z \quad (3.3)$$

where $\overline{\sigma_{nom}} = \mathbb{E}[\sigma_{RCS}]$ is the nominal nonfluctuating target RCS, $P_{Ro} = P_T G_a^2 \lambda^2 \overline{\sigma_{nom}} / (4\pi)^3 L_l R^4$ is the deterministic nominal echo receive power (i.e., w.r.t. $\overline{\sigma_{nom}}$), $G = \sigma_{RCS} / \overline{\sigma_{nom}}$ is the normalized RCS r.v. (i.e. w.r.t. $\overline{\sigma_{nom}}$ such that $\mathbb{E}[G] = 1$), and $Z = X^4$ is the power fluctuation r.v. for 2-way propagation such that the pdf of X is Rice for weak scintillation (as a reference see

also [99] and [100] where the pdf of X is assumed Rayleigh for strong scintillation). For the sake of clarification, an alternative expression for the power fluctuation r.v. for 2-way propagation in a monostatic configuration (see Fig. 3.1) is $Z = X^2 X^2$ where the first term, X^2 , accounts for the power fluctuation on the forth-path (i.e., from the radar to the debris target) while the second term, X^2 , is related to the power fluctuation on the back-path (i.e., from the debris target to the radar)⁵.

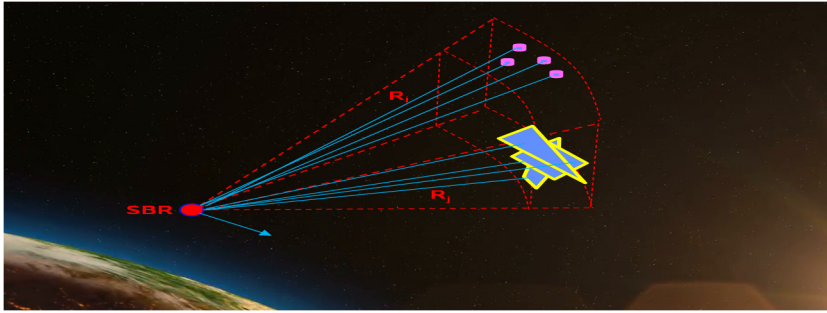


Fig. 3.1. Signal propagation from an orbiting SBR (red dot) towards a debris cloud (purple chunks) and/or a single debris (fragmented yellow shape).

Now, without lack of generality, enforcing $\mathbb{E}[P_R] = P_{R0}$ in eq. (3.3) implies

$$\mathbb{E}[X^4] = 1 \quad (3.4)$$

⁵ Despite the nonreciprocity of general plasma media (see [23, eq. (3.6.19)], the $Z = X^4$ expression entails electromagnetic reciprocity as a reasonable approximation in a monostatic configuration especially in case of weak plasma scintillation at high microwave frequencies, e.g., the K_a -band (see also [23, eq. (3.6.22)]). Viceversa, when the nonreciprocity of plasma media cannot be neglected, the analysis of the power fluctuation for 2-way propagation of monostatic radar configurations should rather follow that of bistatic counterparts in § 3.4.

and allows analyzing the echo receive power at a given polarization as the nominal echo receive power P_{Ro} modulated by the target fluctuation G and channel scintillation Z . Armed with these insights, for a monostatic radar configuration applying the constraint in eq. (3.4) for a r.v. X with a Rice pdf as per eq. (1.8) with parameters b_0^2 and σ_b^2 results in [31]

$$\mathbb{E}[X^4] = b_0^4 + 8\sigma_b^2 b_0^2 + 8\sigma_b^4 = 1 \quad (3.5)$$

Next, the scintillation index s_4 (defined for one-way propagation in eq. (1.6)), can be expressed as

$$s_4 = \sqrt{\frac{\mathbb{E}[X^4] - \mathbb{E}[X^2]^2}{\mathbb{E}[X^2]^2}} = \sqrt{\frac{1 - (b_0^2 + 2\sigma_b^2)^2}{(b_0^2 + 2\sigma_b^2)^2}} \quad (3.6)$$

Combining eqs. (3.5) and (3.6) results in a system of two equations of two unknown variables b_0^2 and σ_b^2 , i.e.,

$$\begin{cases} b_0^2 + 2\sigma_b^2 = (s_4^2 + 1)^{-\frac{1}{2}} \\ b_0^4 + 8\sigma_b^2 b_0^2 + 8\sigma_b^4 = 1 \end{cases} \quad (3.7)$$

which is solved as

$$\begin{cases} b_0^2 = \sqrt{\frac{2}{s_4^2 + 1}} - 1 \\ \sigma_b^2 = \frac{\sqrt{(s_4^2 + 1)^{-1} - b_0^2}}{2} \end{cases} \quad (3.8)$$

and which holds for $1/\sqrt{2} \leq c_s \leq 1$ where $c_s = (s_4^2 + 1)^{-\frac{1}{2}}$, thus framing $0 \leq s_4 \leq 1$. Considering eq. (1.8) and that the pdf

of $Z = X^4$ can be expressed as

$$P_Z(z) = \frac{1}{4\sigma_b^2\sqrt{z}} e^{-\left(\frac{\sqrt{z}+b_0^2}{2\sigma_b^2}\right)} I_0\left(\frac{z^{\frac{1}{4}}b_0}{\sigma_b^2}\right) u(z) \quad (3.9)$$

the pdf of the echo receive power is

$$P_{P_R}(p_R) = \int_{-\infty}^{+\infty} \frac{1}{P_{Ro}} \frac{1}{g} P_Z\left(\frac{p_R}{P_{Ro}} \middle| g\right) P_G(g) dg \quad (3.10)$$

where $P_G(g)$ is the pdf of the normalized RCS G . Consequently, it is possible to elaborate eq. (3.10) for a nonfluctuating target with $P_G(g) = \delta(g - 1)$ (where $\delta(\cdot)$ is the Dirac delta generalized function) to obtain

$$P_{P_{R,nf}}(p_R) = \frac{1}{P_{Ro}} \frac{1}{4\sigma_b^2\sqrt{\frac{p_R}{P_{Ro}}}} e^{-\left(\frac{\sqrt{\frac{p_R}{P_{Ro}}}+b_0^2}{2\sigma_b^2}\right)} I_0\left(\frac{\left(\frac{p_R}{P_{Ro}}\right)^{\frac{1}{4}}b_0}{\sigma_b^2}\right) u(p_R) \quad (3.11)$$

Besides, elaborating on eq. (3.10) for a Rayleigh fluctuating target with $P_G(g) = e^{-g}u(g)$ yields

$$P_{P_{R,Rayleigh}}(p_R) = \int_0^{\infty} \frac{1}{P_{Ro}} \frac{1}{g} \frac{1}{4\sigma_b^2\sqrt{\frac{p_R}{P_{Ro}}}} e^{-\left(\frac{\sqrt{\frac{p_R}{P_{Ro}}g}+b_0^2}{2\sigma_b^2}\right)} I_0\left(\frac{\left(\frac{p_R}{P_{Ro}}g\right)^{\frac{1}{4}}b_0}{\sigma_b^2}\right) e^{-g} dg \quad (3.12)$$

and, similarly, for a Rice fluctuating target with $P_G(g) = (1+r)e^{-r}e^{-(1+r)g}I_0(2\sqrt{r(1+r)g})u(g)$

$$\begin{aligned}
& P_{P_R, \text{Rice}}(p_R) \\
&= \int_0^\infty \frac{1}{P_{Ro}} \frac{1}{g} \frac{1}{4\sigma_b^2 \sqrt{\frac{p_R}{P_{Ro}} g}} e^{-\left(\frac{\sqrt{\frac{p_R}{P_{Ro}} g} + b_0}{2\sigma_b^2}\right)} I_0\left(\frac{\left(\frac{p_R}{P_{Ro}} g\right)^{\frac{1}{4}} b_0}{\sigma_b^2}\right) \\
&\quad \times (1+r) e^{-r} e^{-(1+r)g} I_0(2\sqrt{r(1+r)g}) dg \quad (3.13)
\end{aligned}$$

Remarkably, while the works in [99] and [100] consider a Rayleigh model for strong scintillation (with no explicit dependence on the scintillation index s_4), the FOP computed in [99] and [100] can be extended using eq. (3.8) to a Rice model for weak scintillation as a function of the scintillation index s_4 . In particular, the FOP is defined hereafter as the probability that the radar receive power P_R in eq. (3.3) is less than or equal to v_γ times the nominal radar receive input power P_{Ro} , i.e., via the Cumulative Distribution Function (CDF)

$$F(v_\gamma P_{Ro}) = \int_0^{v_\gamma P_{Ro}} P_{P_R}(p_R) dp_R \quad (3.14)$$

where $P_{P_R}(p_R)$ is given in eqs. (3.11), (3.12), and (3.13) for nonfluctuating, Rayleigh fluctuating, and Rice fluctuating targets, respectively. For the sake of completeness, it is evident that plugging eq. (3.11) in eq. (3.14) results in a closed form expression of the FOP for a nonfluctuating target (see also [116, eq. (2.18)]), i.e.,

$$F_{nf}(v_\gamma) = 1 - Q_1\left(\frac{b_0}{\sigma_b}, \frac{v_\gamma^{\frac{1}{4}}}{\sigma_b}\right) \quad (3.15)$$

where

$$Q_m(a, b) = \int_b^\infty \frac{x^m}{a^{m-1}} e^{-\frac{x^2+a^2}{2}} I_{m-1}(ax) dx \quad (3.16)$$

is the generalized Marcum function of order m [117]. Also, it is worth noting that eq. (3.14) is a function of v_γ solely, since it coincides with the probability that the r.v. P_R/P_{Ro} (or equivalently the r.v. $G \times Z$) is less than or equal to v_γ .

3.1.3 Numerical Integration and Simulation Results for FOP

Considering a SBR in a monostatic configuration (as per Fig. 3.1), the FOP of an echo is reported hereafter for nonfluctuating, Rayleigh, and Rice fluctuating targets jointly with Rice plasma scintillation as a function of the scintillation index s_4 .

Specifically, the plots in Figs. 3.2, 3.3, and 3.4 provide an analysis of eq. (3.14) via both numerical integration methods (solid lines) and MC based (with 10^4 trials) simulation results (dashed lines) for $s_4 = 0.3$, $s_4 = 0.4$, and $s_4 = 0.5$, respectively. The green, blue, magenta, and red curves account for Rayleigh, Rice (with Rice-factor $r_1 = 1$), Rice (with Rice-factor $r_2 = 3$), and nonfluctuating targets, respectively. It appears evident on all plots in Figs. 3.2, 3.3, and 3.4 that the curves pertaining to numerical integration methods are well matched to their MC based counterparts. For the sake of completeness, the closed form expression in eq. (3.15) for $s_4 = 0.3$, $s_4 = 0.4$, and $s_4 = 0.5$ in case of a nonfluctuating target has not been reported since it coincides with the relative numerical integration curve in Figs. 3.2, 3.3, and 3.4, respectively. As expected, for the Rice factor $r_1 = 1$ the Rice target fluctuating model tends to a Rayleigh one (see the proximity of the blue and green curves) whereas, for $r_2 = 3$ the Rice distribution gets closer to the Swerling 0 model (see the closeness of the magenta and red curves). Clearly, the FOP

accounting for $v_\gamma < 1$ in eq. (3.14) for a nonfluctuating target is smaller than that of a Rayleigh target (see the red curves lying beneath the green curves), since in the former case only channel scintillation induces power fluctuations whereas in the latter case both target and channel phenomenology occur. Also, a larger value of the scintillation index s_4 increases the FOP. As a reference, when $s_4 = 0.3$ a 10-dB-loss FOP (i.e., in eq. (3.14) $v_\gamma = 0.1$) is negligible for a nonfluctuating target and accounts for slightly more than a 0.1 probability for a Rayleigh target (as shown in Fig. 3.2). On the other side, when $s_4 = 0.5$ (see Fig. 3.4) a 10-dB-loss FOP for a nonfluctuating target increases to slightly less than a 0.1 probability while it reaches a 0.2 probability for a Rayleigh target. This demonstrates that an SBR for SSA aimed at processing a burst of echoes for detection and tracking schemes is prone to fading losses caused by plasma effects as a function of the scintillation index s_4

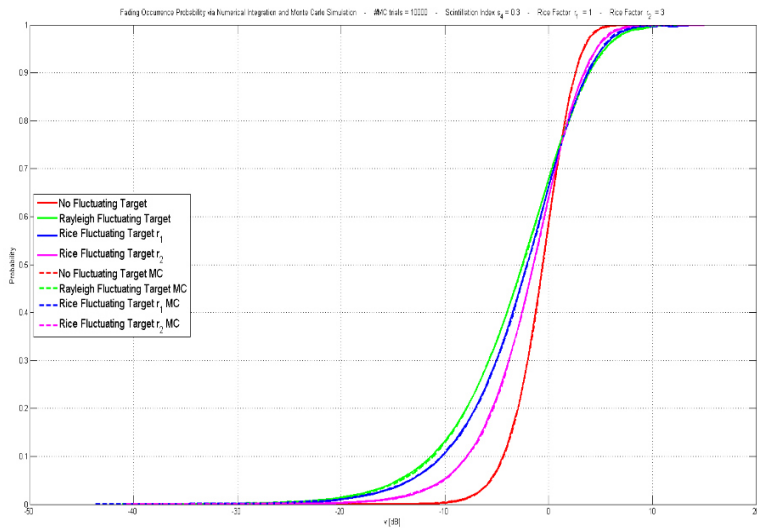


Fig. 3.2. FOP curves for $s_4 = 0.3$.

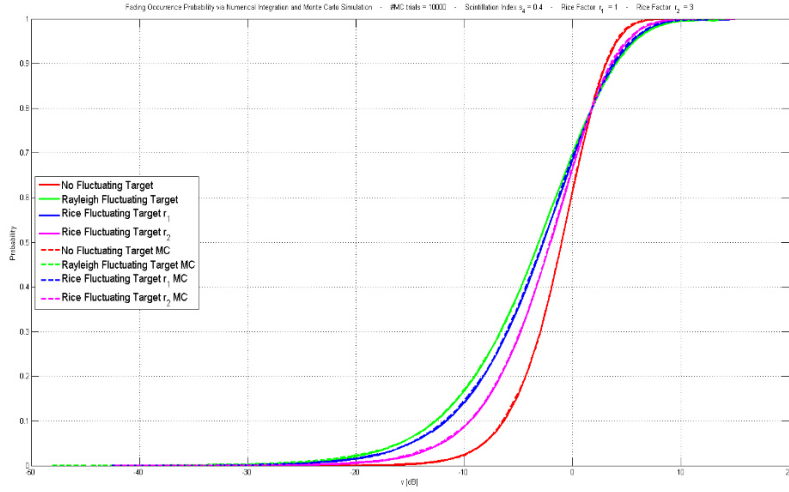


Fig. 3.3. FOP curves for $s_4 = 0.4$.

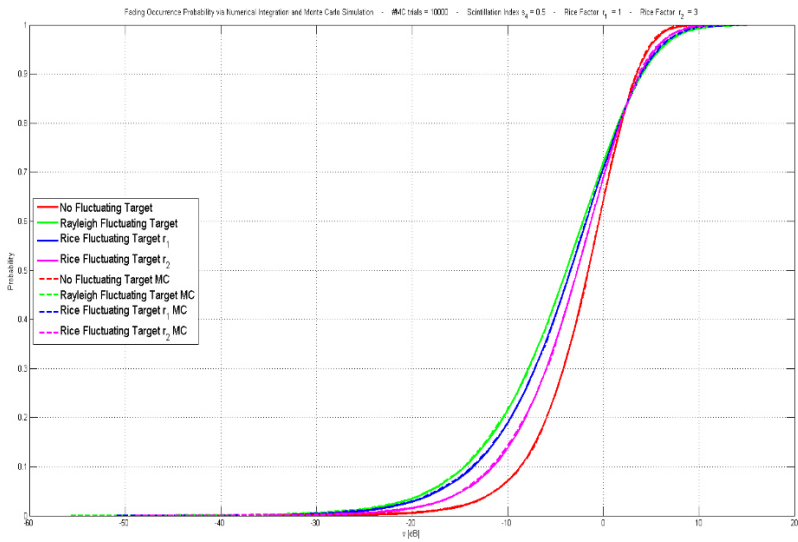


Fig. 3.4. FOP curves for $s_4 = 0.5$.

3.2 Performance analysis of conventional radar detectors for Rayleigh and Rice targets

In this section, the performance analysis of conventional radar detectors in AWGN (see [95, chapters 1 and 2]) is provided in closed form (in terms of P_D as a function of SNR for a given P_{FA}) for nonfluctuating, Rayleigh, and Rice point-like target fluctuations. The reference scenario is that of the pulsed SBR in a monostatic configuration shown in Fig. 3.1 whereby a specific CUT is identified by a given set of range r_χ , elevation θ_χ , and azimuth φ_χ coordinates. Downstream an ideal pulse compression at baseband, a decision statistic \mathfrak{t}_K for a given threshold γ takes into account K pulses to discriminate the null hypothesis H_0 (i.e., $\mathfrak{t}_K < \gamma$) against the alternative hypothesis H_1 (i.e., $\mathfrak{t}_K > \gamma$). The noise samples are Independent Identically Distributed (IID) r.v. (where each sample is a complex circular zero-mean Gaussian r.v. with variance σ_n^2) whereas $A_i e^{j\phi_i}$ is the echo complex amplitude of the i -th pulse (for $i = 0, 1, \dots, K - 1$) embedding unknown parameters pertaining to the radar equation (e.g., related to the radar instrument, RCS, and 2-way channel propagation). Accordingly, for a coherent pulse train (i.e., $A_i e^{j\phi_i} = A e^{j\phi} \forall i$) the GLRT implements the modulus value of a scalar (minimally) sufficient statistic \mathcal{L} (i.e., $\mathfrak{t}_K = |\mathcal{L}|$ as per [95, eq. (2.24)]). For a noncoherent pulse train (i.e., $A_i e^{j\phi_i} \neq A e^{j\phi}$ for $i = 0, 1, \dots, K - 1$), in case all amplitudes are equal to the same value (i.e., $A_i = A \forall i$) the GLRT implements the sum of the modulus value of a vectorial (minimally) sufficient statistic \mathcal{L} (i.e., $\mathfrak{t}_K = \sum_{i=0}^{K-1} |\mathcal{L}(i)|$ as shown in [95, eq. (2.29)]) whereas, otherwise, the GLRT results in the energy (i.e., the sum of the square of the modulus value) of a vectorial (minimally) sufficient statistic \mathcal{L} (i.e., $\mathfrak{t}_K = \sum_{i=0}^{K-1} |\mathcal{L}(i)|^2$ as indicated in [95, eq. (2.32)]). In this work, the performance of the GLRT will be explored solely for the coherent

pulse train case (i.e., for $\mathfrak{t}_K = |\mathcal{L}|$) and square-law noncoherent pulse train case (i.e., for $\mathfrak{t}_K = \sum_{i=0}^{K-1} |\mathcal{L}(i)|^2$). That is, the GLRT performance analysis for the linear noncoherent pulse train case (i.e., for $\mathfrak{t}_K = \sum_{i=0}^{K-1} |\mathcal{L}(i)|$) is outside the scope of this work since it is not available in closed form and (to the author's best knowledge) can be obtained only via Monte Carlo simulations [101] as stressed in [95].

3.2.1 Performance Analysis for Nonfluctuating Targets

Following [95], for the performance analysis with respect to a nonfluctuating (i.e., Swerling 0) target, let us define the single-pulse SNR for the coherent pulse train case as

$$SNR_{coh} = \frac{A^2}{\sigma_n^2} \quad (3.17)$$

and outline for the coherent pulse train case (and coherent GLRT detector)

$$P_{FA} = e^{-\frac{\gamma^2}{K \sigma_n^2}} \quad (3.18)$$

and

$$P_D = Q_1\left(\sqrt{2K SNR_{coh}}, \sqrt{\frac{2\gamma^2}{K \sigma_n^2}}\right) = Q_1\left(\sqrt{2K SNR_{coh}}, \sqrt{-2 \ln P_{FA}}\right) \quad (3.19)$$

On the other side, by defining the average single-pulse SNR for the noncoherent pulse train case as

$$SNR_{ncoh} = \frac{1}{K} \sum_{i=0}^{K-1} \frac{A_i^2}{\sigma_n^2} \quad (3.20)$$

it is possible to write for the noncoherent pulse train case (and square-law noncoherent GLRT detector)

$$P_{FA} = e^{-\frac{\gamma}{\sigma_n^2}} \sum_{i=0}^{K-1} \frac{1}{i!} \left(\frac{\gamma}{\sigma_n^2}\right)^i = \frac{1}{\Gamma(K)} \Gamma_{inc}\left(K, \frac{\gamma}{\sigma_n^2}\right) \quad (3.21)$$

and

$$P_D = Q_K\left(\sqrt{2K SNR_{ncoh}}, \sqrt{2\frac{\gamma}{\sigma_n^2}}\right) \quad (3.22)$$

whereby, for $\zeta \in \mathbb{N} \setminus \{0\}$, $\Gamma(\zeta) = (\zeta - 1)!$ is the Gamma function and

$$\Gamma_{inc}(\zeta, x) = \int_x^\infty t^{\zeta-1} e^{-t} dt \quad (3.23)$$

is the upper incomplete Gamma function [118].

3.2.2 Performance Analysis for Rayleigh Targets

In general terms, it is possible to formulate the performance analysis for Rayleigh targets by averaging the P_D computed for a nonfluctuating target with respect to the ensuing SNR fluctuation laws. For the sake of completeness, such a P_D is, de facto, conditioned to a given value z of the r.v. Z (in simple terms, in this section we will simply assume $z = 1$, thus neglecting fluctuations due to propagation). More specifically, capitalizing on analytic solutions to structured integrals expressed as the Laplace transform of the product of Marcum Q and power functions [119], the performance analysis can be expressed in closed form. In this respect (see also [112]), introducing the Pochhammer symbol [118] defined as

$$(x)_n = \prod_{k=0}^{n-1} (x + k) \quad (3.24)$$

and, for $\mathbb{H} \in \mathbb{N} \setminus \{0\}$, considering a finite sum representation of eq. (3.23) [118], i.e.,

$$\Gamma_{inc}(\mathbb{H}, x) = \Gamma(\mathbb{H})e^{-x} \sum_{k=0}^{\mathbb{H}-1} \frac{x^k}{k!} \quad (3.25)$$

it follows that (see also Appendix A)

$$\begin{aligned} & \int_0^\infty Q_{\mathbb{H}}(\sqrt{2bx}, \sqrt{2T}) \frac{1}{\beta^\alpha} \frac{x^{\alpha-1}}{\Gamma(\alpha)} e^{-\frac{x}{\beta}} dx \\ &= \begin{cases} \sum_{n=0}^{\infty} \frac{(\alpha)_n (b\beta)^n}{(b\beta+1)^{\alpha+n} \Gamma(\mathbb{H}+n)n!} \Gamma_{inc}(\mathbb{H}+n, T), & \alpha > 0 \\ \sum_{n=0}^{\alpha-\mathbb{H}} \binom{\alpha-\mathbb{H}}{n} \frac{(b\beta)^n}{(b\beta+1)^{\alpha-\mathbb{H}} \Gamma(\mathbb{H}+n)} \Gamma_{inc}\left(\mathbb{H}+n, \frac{T}{b\beta+1}\right), & \alpha \geq \mathbb{H} \geq 1, \alpha \in \mathbb{N} \end{cases} \end{aligned} \quad (3.26)$$

Now, for the performance analysis of a Swerling I target the r.v. G assumes a common value, say g , among the K pulses. In this case, let us first define $\overline{SNR} = P_{Ro}/\sigma_n^2$ as the average single-pulse SNR within K pulses and replace SNR_{coh} with the r.v. $\overline{SNR} \times G$, where the pdf of G is given in eq. (3.1) with $\Omega = 1$ and⁶ $\alpha = 1$. For the coherent pulse train case and coherent GLRT detector with scan-to-scan decorrelation (i.e., $A_i = A$ and $\phi_i = \phi$, for $i = 0, 1, \dots, K-1$), one may then substitute in eq. (3.26) $\mathbb{H} = 1$, $b = K$, $T = -\ln P_{FA}$, $\alpha = 1$, and $\beta = \overline{SNR}$ thus yielding

$$P_D = \Gamma_{inc}\left(1, \frac{-\ln P_{FA}}{K \overline{SNR} + 1}\right) = P_{FA}^{\frac{1}{K \overline{SNR} + 1}} \quad (3.27)$$

For the noncoherent pulse train case and square-law noncoherent GLRT detector with scan-to-scan decorrelation (i.e., $A_i = A$, for $i = 0, 1, \dots, K-1$), SNR_{ncoh} is also replaced with the

⁶ For the sake of completeness, $\alpha = 2$ is used for the Swerling III model.

r.v. $\overline{SNR} \times G$, with the pdf of G as per eq. (3.1) with $\Omega = 1$ and $\alpha = 1$. This leads to use eq. (3.26) with $\mathbb{H} = K$, $b = K$, $T = \frac{\gamma}{\sigma_n^2}$, $\alpha = 1$, and $\beta = \overline{SNR}$ to obtain

$$P_D = \sum_{n=0}^{\infty} \frac{(\overline{KSNR})^n}{(\overline{KSNR}+1)^{1+n}\Gamma(K+n)} \Gamma_{inc} \left(K + n, \frac{\gamma}{\sigma_n^2} \right) \quad (3.28)$$

Finally, for the performance analysis of a Swerling II target the r.v. G 's, referred to hereafter as $G(i)$, for $i = 0, 1, \dots, K - 1$, are IID within the K pulses. Clearly, this instance is meaningful only for the noncoherent pulse train case and square-law noncoherent GLRT detector. As a consequence, it is possible to express SNR_{ncoh} as the r.v. $\frac{1}{K} \times \overline{SNR} \times S$, with $S = \sum_{i=0}^{K-1} G(i)$ a central chi square r.v. with $2K$ degrees of freedom and statistical mean $2\sigma^2 K$, which is tantamount (for $2\sigma^2 = 1$ as per [116, eq. (2.32)]) to adopt eq. (3.1) with $\Omega = K$ and⁷ $\alpha = K$. Thus, one may substitute in eq. (3.26) $\mathbb{H} = K$, $b = 1$, $T = \gamma/\sigma_n^2$, $\alpha = K$, $\beta = \overline{SNR}$, and derive

$$P_D = e^{-\frac{\gamma/\sigma_n^2}{1+\overline{SNR}}} \sum_{n=0}^{K-1} \frac{1}{n!} \left(\frac{\gamma/\sigma_n^2}{1+\overline{SNR}} \right)^n \quad (3.29)$$

3.2.3 Performance Analysis for Rician Targets

Similarly to the performance analysis for Rayleigh targets, by assuming $z = 1$ (thus neglecting power fluctuations due to propagation) it is possible to formulate the performance analysis for Rice targets by averaging the P_D computed for a nonfluctuating target with respect to the entailing SNR fluctuation laws. In this case, it appears useful to represent in closed form

⁷ For the sake of completeness, $\alpha = 2K$ applies to the Swerling IV model.

integrals involving the Laplace transform of the product of Marcum Q , Bessel I , and power functions [120], i.e.,

$$In(\alpha, \beta, c, p, \mu_1, \mu_2) = \int_0^\infty e^{-px} Q_{\mu_1}(\alpha\sqrt{x}, \beta) x^{\frac{\mu_2-1}{2}} I_{\mu_2-1}(c\sqrt{x}) dx \quad (3.30)$$

such that, for $\mu_2 \in \mathbb{R}$ and $\mu_1 = \mu_2$

$$In(\alpha, \beta, c, p, \mu_1, \mu_1) = \frac{1}{p} \left(\frac{c}{2p}\right)^{\mu_1-1} e^{\frac{c^2}{4p}} Q_{\mu_1} \left(\frac{\alpha c}{\sqrt{2p\tilde{p}}}, \beta \sqrt{\frac{2p}{\tilde{p}}} \right) \quad (3.31)$$

with $\tilde{p} = 2p + \alpha^2$ while, for $\mu_2 \in \mathbb{R}$, $\mu_2 > -1$, $\mu_1 = \mu_2 + n$, and $n \in \mathbb{N} \setminus \{0\}$

$$\begin{aligned} In(\alpha, \beta, c, p, \mu_2 + n, \mu_2) &= In(\alpha, \beta, c, p, \mu_2, \mu_2) \\ &+ \left\{ \frac{2}{c} \left(-\frac{\alpha^2}{c} \right)^{-\mu_2} e^{-\frac{\beta^2}{2}} \sum_{k=0}^{n-1} \sum_{v=0}^{2k} \left(\frac{\beta^2}{2} \right)^v \left(-\frac{\alpha^2}{\tilde{p}} \right)^{-k+v} \right. \\ &\times \delta_v \left(k+1, \mu_2+k+1, -\frac{\alpha^2\beta^2}{2\tilde{p}}, \frac{\alpha^2\beta^2c^2}{4\tilde{p}^2} \right) \\ &\left. \times \left[1 - Q_{\mu_2+k-v} \left(j \frac{c}{\sqrt{\tilde{p}}}, j \frac{\alpha\beta}{\sqrt{\tilde{p}}} \right) \right] \right\} \end{aligned} \quad (3.32)$$

where

$$\delta_v(b, g, w, z) = \frac{(-1)^{b-1} z^{b-1-v}}{w^{b-1} \Gamma(b)} \sum_{k=0}^{\lfloor \frac{v}{2} \rfloor} \frac{(-1)^k (b-v+k)_{v-k} (g-v-1+k)_{v-2k}}{(v-2k)! k!} z^k \quad (3.33)$$

in which the $\lfloor \zeta \rfloor$ operator accounts for rounding ζ to the nearest integer less than or equal to ζ , j is the imaginary unit [121], and once again $\tilde{p} = 2p + \alpha^2$. For the sake of clarification, in eq. (3.33) $\Gamma(b)$ is the ordinary Gamma function (i.e. $\Gamma_{inc}(b, 0)$ [31]) for $\mathcal{Re}(b) > 0$ whereas in eq. (3.30) $\mu_1, \mu_2, c \in \mathbb{R}$, $p \in \mathbb{R}^+ \cup \{0\}$, α, β are either real or purely imaginary, and $Q_m(j\alpha, j\beta) = \overline{Q_m(\alpha, \beta)}$ is the modified complex generalized Marcum function

of third kind and order m which, for $\alpha = a \in \mathbb{R}$, $\beta = b \in \mathbb{R}$, assumes the simplified expression [117]

$$\overline{Q_m(a, b)} = 1 + e^{j\pi(m-1)} \frac{1}{a^{m-1}} \int_0^b x^m e^{\frac{x^2+a^2}{2}} I_{m-1}(ax) dx \quad (3.34)$$

Armed with this background, it is now possible to outline the performance analysis of a Rice target in case the r.v. G assumes a common value, say g , among the K pulses (i.e., scan-to-scan decorrelation). For the coherent pulse train case and coherent GLRT detector (i.e., $A_i = A$ and $\phi_i = \phi$, for $i = 0, 1, \dots, K-1$), this is tantamount to substitute SNR_{coh} with the r.v. $\overline{SNR} \times G$, where $\overline{SNR} = P_{Ro}/\sigma_n^2$ is the average single-pulse SNR within K pulses, and the pdf of G is expressed as per eq. (3.2) with $\Omega = 1$. Consequently, one may substitute in eq. (3.30) $\mu_1 = 1$, $\mu_2 = 1$, $\alpha = \sqrt{2K\overline{SNR}}$, $\beta = \sqrt{2T}$, $T = -\ln P_{FA}$, $p = 1+r$, and $c = 2\sqrt{r(r+1)}$ which leads to

$$P_D = Q_1 \left(\frac{\sqrt{2rK\overline{SNR}}}{\sqrt{(1+r)+K\overline{SNR}}}, \sqrt{-2\ln P_{FA}} \sqrt{\frac{1+r}{(1+r)+K\overline{SNR}}} \right) \quad (3.35)$$

For the noncoherent pulse train case and square-law noncoherent GLRT detector (i.e., $A_i = A$, for $i = 0, 1, \dots, K-1$), SNR_{ncoh} is again replaced with the r.v. $\overline{SNR} \times G$, with the pdf of G as per eq. (3.2) with $\Omega = 1$. Therefore, substituting in eq. (3.30)

$\mu_1 = \mu_2 + K - 1 = K$, $\mu_2 = 1$, $\alpha = \sqrt{2K\overline{SNR}}$, $\beta = \sqrt{2T}$, $T = \frac{\gamma}{\sigma_n^2}$, $p = 1+r$, and $c = 2\sqrt{r(r+1)}$ results in

$$\begin{aligned}
P_D = & Q_1 \left(\frac{\sqrt{2rK\overline{SNR}}}{\sqrt{(1+r)+K\overline{SNR}}}, \sqrt{2\frac{\gamma}{\sigma_n^2}} \sqrt{\frac{1+r}{(1+r)+K\overline{SNR}}} \right) \\
& + (1+r)e^{-r} \left(-\frac{1}{K\overline{SNR}} \right) e^{-\frac{\gamma}{\sigma_n^2}} \sum_{m=0}^{K-2} \sum_{v=0}^{2m} \left(\frac{\gamma}{\sigma_n^2} \right)^v \left(-\frac{K\overline{SNR}}{(1+r)+K\overline{SNR}} \right)^{-m+v} \times \\
& \delta_v \left(m+1, m+2, -\frac{K\overline{SNR}\frac{\gamma}{\sigma_n^2}}{(1+r)+K\overline{SNR}}, \frac{K\overline{SNR}\frac{\gamma}{\sigma_n^2}r(r+1)}{[(1+r)+K\overline{SNR}]^2} \right) \times \left[1 - \right. \\
& \left. Q_{1+m-v} \left(j\frac{\sqrt{2r(r+1)}}{\sqrt{(1+r)+K\overline{SNR}}}, j\frac{\sqrt{K\overline{SNR}\frac{\gamma}{\sigma_n^2}2}}{\sqrt{(1+r)+K\overline{SNR}}} \right) \right] \quad (3.36)
\end{aligned}$$

Next, the performance analysis of a Rice target follows hereafter when the r.v. G 's (i.e., $G(i)$, for $i = 0, 1, \dots, K-1$) are IID within the K pulses (i.e., pulse-to-pulse fluctuations). Again, this condition is meaningful only for the noncoherent pulse train case and square-law noncoherent GLRT detector. Accordingly, SNR_{ncoh} is replaced with the r.v. $\frac{1}{K} \times \overline{SNR} \times S$, with S a noncentral chi square r.v. with $2K$ degrees of freedom, noncentrality parameter Kq^2 , and (see [116, eq. (2.47)] using [122, eq. (13.1.2)]) statistical mean $K(q^2 + 2\sigma^2)$. In particular, recalling that $\Omega = 1$ the pdf of S can be given as a function of r

$$P_S(s|r) = \frac{(1+r)^{\frac{K+1}{2}} s^{\frac{K-1}{2}}}{(rK)^{\frac{K-1}{2}}} e^{-rK} e^{-(1+r)s} I_{K-1} \left(2\sqrt{Kr(1+r)s} \right) u(s) \quad (3.37)$$

Thus, one may replace in eq. (3.30) $\mu_1 = K$, $\mu_2 = K$, $\alpha = \sqrt{2\overline{SNR}}$, $\beta = \sqrt{2T}$, $T = \frac{\gamma}{\sigma_n^2}$, $p = 1+r$, and $c = 2\sqrt{Kr(r+1)}$ which results in

$$P_D = Q_K \left(\frac{\sqrt{2rK\overline{SNR}}}{\sqrt{(1+r)+\overline{SNR}}}, \sqrt{2\frac{\gamma}{\sigma_n^2}} \sqrt{\frac{1+r}{(1+r)+\overline{SNR}}} \right) \quad (3.38)$$

3.3 Performance analysis for target fluctuations and Rice scintillation

In this section, the performance analysis of conventional radar detectors is extended to include either Rayleigh and Rice target fluctuations jointly with Rice plasma scintillation as a function of the scintillation index s_4 . Notably, the superposition of target fluctuation and weak plasma scintillation as a function of s_4 proves quite demanding from an analytical perspective. This leads to employ semi-analytic techniques for averaging P_D starting from the closed form solutions for target fluctuations obtained in Section 3.2. Accordingly, the averaging of P_D for weak scintillation with respect to the ensuing SNR fluctuations laws is carried out for several target fluctuation cases. Namely:

- Swerling 0 coherent case (SW0-C) (as per eqs. (3.18) and (3.19));
- Swerling 0 noncoherent case (SW0-NC) (as per eqs. (3.21) and (3.22));
- Swerling 1 coherent case (SW1-C) (as per eqs. (3.18) and (3.27));
- Swerling 1 noncoherent case (SW1-NC) (as per eqs. (3.21) and (3.28));
- Swerling 2 noncoherent case (SW2-NC) (as per eqs. (3.21) and (3.29));
- Rice scan-to-scan coherent case (R-S2S-C) (as per eqs. (3.18) and (3.35));
- Rice scan-to-scan noncoherent case (R-S2S-NC) (as per eqs. (3.21) and (3.36));
- Rice pulse-to-pulse noncoherent case (R-P2P-NC) (as per eqs. (3.21) and (3.38)).

More specifically, in the aforementioned closed form expressions for P_D the SNR (taking into account the appropriate definition of SNR in use) is replaced with $SNR \times Z$, with the r.v. $Z = X^4$ such that X is Rice with parameters q^2 and σ^2 , both as a function of s_4 as per eq. (3.8). Consequently, each of the obtained analytic formulations for P_D can be averaged with respect to the distribution of Z , whereby the expectation operator is approximated via Monte Carlo techniques with 1000 trials. Such an expectation operator applied to eqs. (3.19), (3.22), (3.27), (3.28), (3.29), (3.35), (3.36), (3.38) results in the performance curves for weak scintillation addressed hereafter as SW0-C-WS, SW0-NC-WS, SW1-C-WS, SW1-NC-WS, SW2-NC-WS, R-S2S-C-WS, R-S2S-NC-WS, and R-P2P-NC-WS, respectively. All Rician curves (i.e., R-S2S-C, R-S2S-NC, R-P2P-NC, R-S2S-C-WS, R-S2S-NC-WS, and R-P2P-NC-WS) are addressed according to two different values of the Rice factor r , namely, r_1 and r_2 appended as subscripts.

3.3.1 Numerical Results for Coherent Pulse Trains

Figs 3.5-3.6 show numerical results for the performance analysis of the GLRT detector in terms of P_D as a function of single pulse SNR in case of coherent pulse trains. The curves are further characterized by P_{FA} , the scintillation index s_4 , the Rice factor r , and the number of pulses K for the SW0-C, SW1-C, and R-S2S-C cases without weak scintillation, as well as the SW0-C-WS, SW1-C-WS, and R-S2S-C-WS cases with weak scintillation. In particular,

- Fig. 3.5 considers $P_{FA} = 10^{-5}$, $s_4 = 0.1$, $r_1 = 1$ and $r_2 = 8$, $K = 4$;
- Fig. 3.6 accounts for $P_{FA} = 10^{-5}$, $s_4 = 0.4$, $r_1 = 1$ and $r_2 = 8$, $K = 4$.

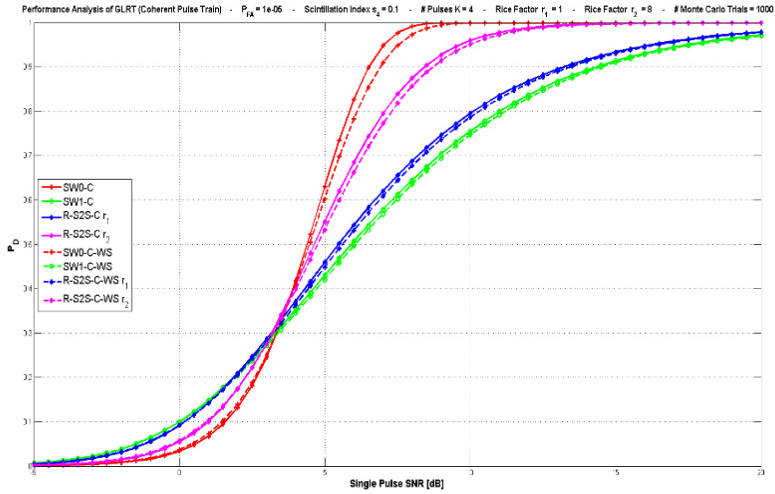


Fig. 3.5. GLRT performance (coherent case) with $P_{FA} = 10^{-5}$, $s_4 = 0.1$, $r_1 = 1$ and $r_2 = 8$, $K = 4$.

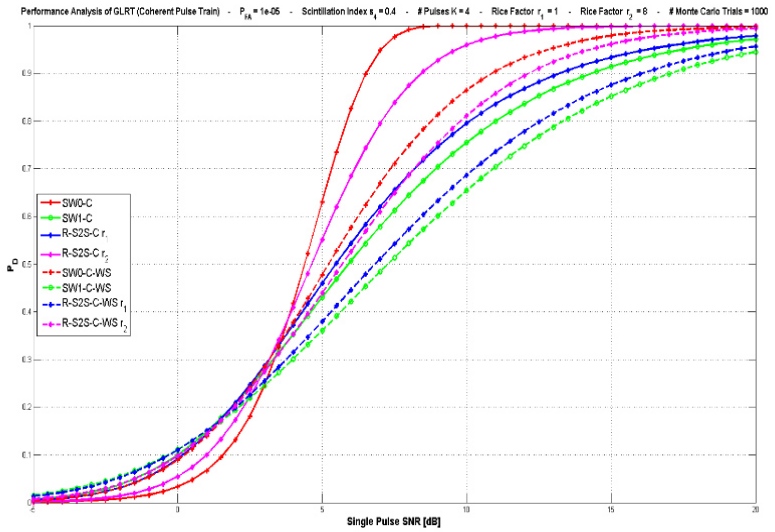


Fig. 3.6. GLRT performance (coherent case) with $P_{FA} = 10^{-5}$, $s_4 = 0.4$, $r_1 = 1$ and $r_2 = 8$, $K = 4$.

At a given P_{FA} and P_D the required single pulse SNR increases when s_4 increases as shown for $K = 4$ in Figs. 3.5 and 3.6 or, alternatively⁸, for $K = 1$ in Figs. 3.7 and 3.9. This is evident for either nonfluctuating targets (see the mutual displacement between the SW0-C case and the SW0-C-WS case when s_4 increases) or fluctuating targets (i.e., see the SW1-C and R-S2S-C cases compared to the SW1-C-WS and R-S2S-C-WS cases, respectively, when s_4 increases). As expected, the required single pulse SNR increases when K decreases [40],[93-95]. This is evident by the leftward shift of the plots in Figs. 3.5 and 3.6 pertaining to $K = 4$ compared to those in Figs. 3.7 and 3.9, respectively, when $K = 1$. As per [105], in Fig. 3.5 and 3.6 for large to moderate P_D (e.g., for $P_D > 0.5$) the SW0 cases (i.e., the SW0-C or, alternatively, the SW0-C-WS) provide the smallest SNR required to obtain a given P_D , while the SW1 cases (i.e., the SW1-C or, alternatively, the SW1-C-WS) entail the largest SNR required to obtain a given P_D among all considered cases. Also, in Fig. 3.5 and 3.6, for $r = 8$ the Rice target fluctuating model tends to a Swerling 0 (see the proximity of the SW0-C with the R-S2S-C r_2 curves or, alternatively, that of the SW0-C-WS with the R-S2S-C-WS r_2 curves) whereas, for $r = 1$ the Rice distribution gets closer to a Rayleigh one (see the closeness of the SW1-C with the R-S2S-C r_1 curves or, alternatively, that of the SW1-C-WS with the R-S2S-C-WS r_1 curves). As shown in Fig. 3.5, when $s_4 = 0.1$ the SNR loss (i.e., the additional SNR required to obtain the same P_D when scintillation occurs compared to the nonscintillating case) is quite limited and definitely less

⁸ For the sake of clarification, the plots in Fig. 3.7 and 3.9 refer to the numerical results for the square-law noncoherent GLRT detector addressed in § 3.3.2 but for $K = 1$ the coherent and noncoherent decision rules are equivalent. In other words, when $K = 1$ the performance of SW0-C, SW1-C, R-S2S-C, SW0-C-WS, SW1-C-WS, and R-S2S-C-WS coincide with those of SW0-NC, SW1-NC, R-S2S-NC, SW0-NC-WS, SW1-NC-WS, and R-S2S-NC-WS, respectively.

than 0.5 dB (see the displacement between the SW0-C and the SW0-C-WS curves as a worst case) and becomes negligible in the other cases (see the SW1-C, R-S2S-C r_1 , R-S2S-C r_2 curves compared to the SW1-C-WS, R-S2S-C-WS r_1 , R-S2S-C-WS r_2 curves, respectively). On the other side, when $s_4 = 0.4$ the SNR loss becomes more significant depending on the P_D as shown in Fig. 3.6 (specific SNR losses at a given reference P_D will be summarized in chapter 5).

3.3.2 Numerical Results for Noncoherent Pulse Trains

Figs. 3.7-3.10 show numerical results for the performance analysis of the GLRT detector in terms of P_D as a function of the single pulse SNR for noncoherent pulse trains with a square-law integrator. Similarly to the coherent pulse train cases, the curves are further characterized by P_{FA} , the scintillation index s_4 , the Rice factor r , and the number of pulses K for the SW0-NC, SW1-NC, SW2-NC, R-S2S-NC, and R-P2P-NC cases without weak scintillation as well as the SW0-NC-WS, SW1-NC-WS, SW2-NC-WS, R-S2S-NC-WS, and R-P2P-NC-WS cases with weak scintillation. In particular,

- Fig. 3.7 reports $P_{FA} = 10^{-5}$, $s_4 = 0.1$, $r_1 = 1$ and $r_2 = 8$, $K = 1$;
- Fig. 3.8 shows $P_{FA} = 10^{-5}$, $s_4 = 0.1$, $r_1 = 1$ and $r_2 = 8$, $K = 4$;
- Fig. 3.9 addresses $P_{FA} = 10^{-5}$, $s_4 = 0.4$, $r_1 = 1$ and $r_2 = 8$, $K = 1$;
- Fig. 3.10 indicates $P_{FA} = 10^{-5}$, $s_4 = 0.4$, $r_1 = 1$ and $r_2 = 8$, $K = 4$.

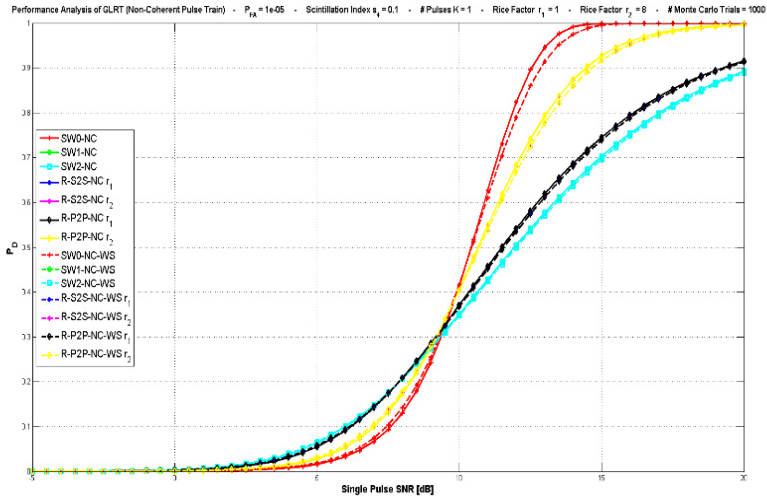


Fig. 3.7. GLRT performance (noncoherent case) with $P_{FA} = 10^{-5}$, $s_4 = 0.1$, $r_1 = 1$ and $r_2 = 8$, $K = 1$.

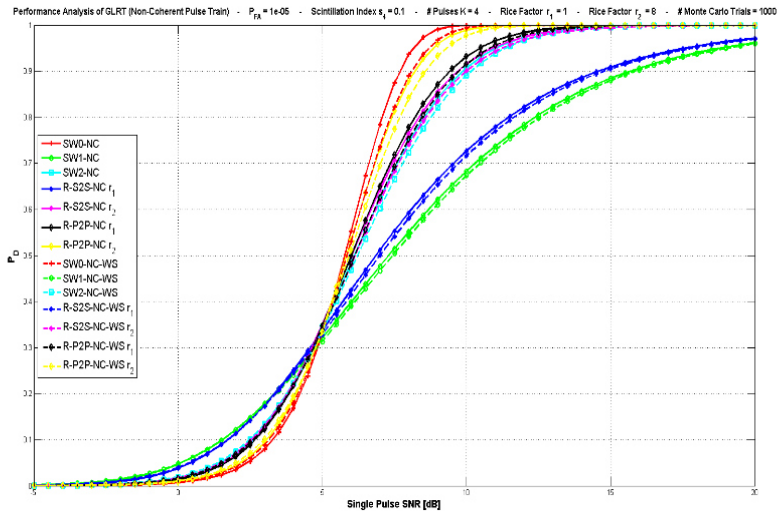


Fig. 3.8. GLRT performance (noncoherent case) with $P_{FA} = 10^{-5}$, $s_4 = 0.1$, $r_1 = 1$ and $r_2 = 8$, $K = 4$.

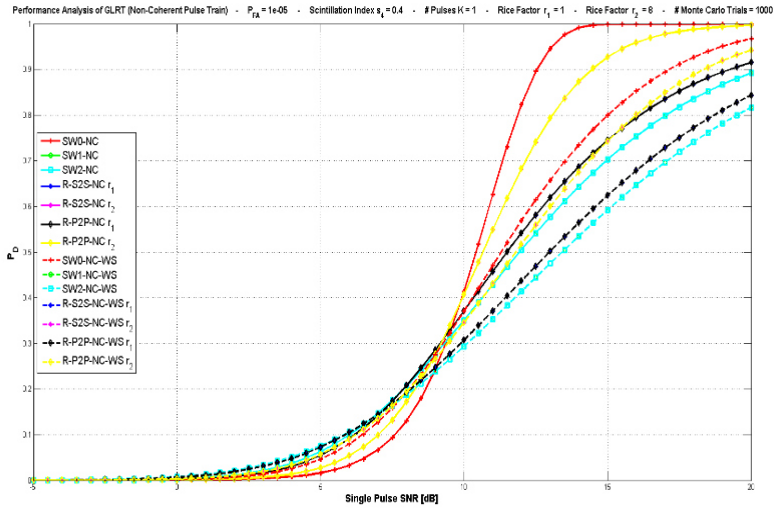


Fig. 3.9. GLRT performance (noncoherent case) with $P_{FA} = 10^{-5}$, $s_4 = 0.4$, $r_1 = 1$ and $r_2 = 8$, $K = 1$.

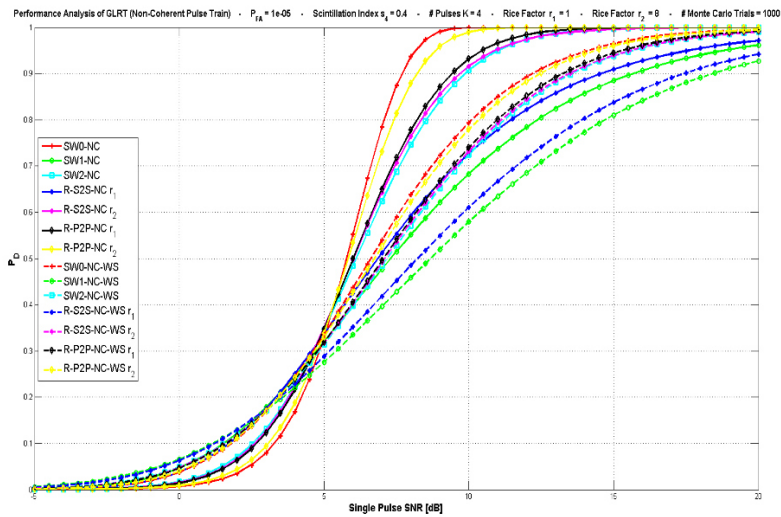


Fig. 3.10. GLRT performance (noncoherent case) with $P_{FA} = 10^{-5}$, $s_4 = 0.4$, $r_1 = 1$ and $r_2 = 8$, $K = 4$.

Again, at a given P_{FA} and P_D the required single pulse SNR increases when K decreases as well as when s_4 increases for either nonfluctuating targets (i.e., the SW0-NC case compared to the SW0-NC-WS case) or fluctuating targets (i.e., the SW1-NC, SW2-NC, R-S2S-NC, and R-P2P-NC cases compared to the SW1-NC-WS, SW2-NC-WS, R-S2S-NC-WS, and R-P2P-NC-WS cases, respectively). Also, in Figs. 3.7 through 3.10 for large to moderate P_D (e.g., for $P_D > 0.5$) the SW0 cases (i.e., the SW0-NC or, alternatively, the SW0-NC-WS) indicate the smallest SNR required to obtain a given P_D , while the SW1 cases (i.e., the SW1-NC or, alternatively, the SW1-NC-WS) cue the largest SNR required to obtain a given P_D among all considered cases. As analytically predicted, in Figs. 3.7 and 3.9 for $K = 1$ the SW1 and SW2 cases coincide while the R-S2S and R-P2P curves also overlap. Again, for $r = 8$ the Rice target fluctuation tends to the Swerling 0 model whereas, for $r = 1$ the Rice and Rayleigh distributions approach one another. Finally, when $s_4 = 0.1$ the SNR loss is very small. Yet, when $s_4 = 0.4$ the SNR loss becomes larger and its value depends on the P_D as shown in Figs. 3.9 and 3.10.

3.4 Extension of the Analysis to Bistatic Configurations

The previous performance analysis of conventional detectors pertaining to monostatic configurations is briefly extended hereafter to a bistatic configuration. For example, Fig. 3.11 represents as red points at a specific instant, a SBR, a debris, and an arbitrary scattering location. In particular, let us consider that a SBR transmits a train of pulses towards a target at a distance R_1 in the Fraunhofer region. Now, the one-way propagation from the SBR to such a target or, equivalently, from the target to an

arbitrary receiver at a distance R_2 in the Fraunhofer region can be analyzed by constraining the average power to abide by the forward scattering assumption in the weak scintillation model [24]. That is, considering either the SBR-debris one-way propagation or the debris-target one-way propagation the mean square value of B in eq. (1.7) can be enforced to be unitary as per eq. (1.9).

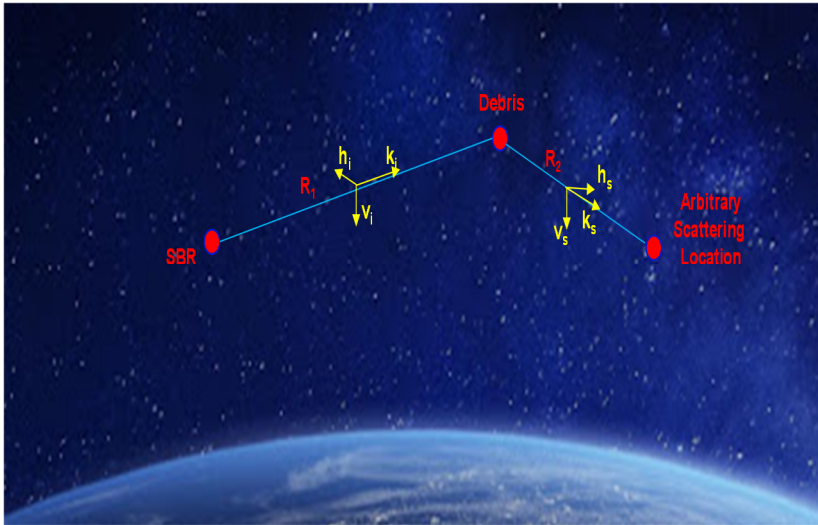


Fig. 3.11. SBR for SSA in a bistatic configuration w.r.t. an arbitrary scattering location.

As shown in [34], for one-way propagation the direct relation between the scintillation index s_4 and the Rice pdf in eq. (1.8) with parameters b_0^2 and σ_b^2 can be written as eq. (1.10). As hinted in chapter 1, combining eqs. (1.9) and (1.10) in terms of the scintillation index s_4 one obtains the liaison between experimental results from plasma radio-physics and one-way propagation in weak scintillation. To this end, eqs. (1.11) and (1.12) which are reported hereafter for convenience as

$$\begin{cases} b_0^2 = \sqrt{1 - s_4^2} \\ \sigma_b^2 = \frac{1 - \sqrt{1 - s_4^2}}{2} \end{cases} \quad (3.39)$$

can be used in radar theory for debris detection and tracking. In this case, the closed form expressions for P_D (i.e., eqs. (3.19), (3.22), (3.27), (3.28), (3.29), (3.35), (3.36), (3.38)) still hold in case of a bistatic configuration. Clearly, in such a configuration the G_a^2 term in eq. (3.3) is factored into a transmit, G_{Tx} , and receive, G_{Rx} , antenna gain (i.e., $G_a^2 = G_{Tx}G_{Rx}$), the R^4 term in eq. (3.3) is split into a forth path term, R_1^2 , and a path term towards the arbitrary scattering location, R_2^2 , i.e., $R^4 = R_1^2R_2^2$, while the nominal non-fluctuating monostatic RCS $\overline{\sigma_{nom}}$ in eq. (3.3) becomes an equivalent bistatic counterpart. Consequently, each of the obtained analytic formulations for P_D in a bistatic configuration can be averaged via Monte Carlo techniques with respect to the entailing fluctuation law of the SNR (provided that the appropriate definition of SNR is in use). Specifically, the SNR is replaced with $SNR \times X_1^2 \times X_2^2$ where X_1 (pertaining to the power fluctuation X_1^2 of the one-way propagation path between the transmitter and the debris) and X_2 (pertaining to the power fluctuation X_2^2 of the one-way propagation path between the debris and the receiver) are eventually Rice r.v., with parameters b_0^2 and σ_b^2 , and both as a function of s_4 as per eq. (3.39). Definitely, the one-way propagation fluctuation from an SBR to a debris can be statistically independent of the one-way propagation fluctuation from a debris to an arbitrary scattering location and not identically distributed. In other words, in a bistatic configuration s_4 on the one-way propagation path between the transmitter and the debris can be different from s_4 on the one-way propagation path between the debris and the receiver.

Chapter 4

MIMO SBR via Code Division Multiplexing for Track While Simultaneous Search

The SBR system architecture described in chapter 2 comprises an AESA subsystem, an RF subsystem, and a digital subsystem, whereby the multichannel diversity is based on a SIMO configuration. In particular, considering either a H or V polarization, at a given *transmit-receive-polarization-pair* (i.e., either $H-H$, $H-V$, $V-H$, or $V-V$), the SIMO SBR is devised with 1 transmit channel and 4 receive channels: Σ , Δ_{el} , Δ_{az} , grd , i.e., sum, delta-elevation, and delta-azimuth channels for monopulse angular estimation, and a guard channel for SLB, respectively. To this end, the SIMO-based archetype hinted in chapter 2 is orchestrated according to a moderate payload complexity and considering a bespoke surveillance mode. More specifically, with such a limited multichannel diversity, the monopulse angular estimation is implemented via classical simultaneous-lobing [74] within the ABFN of the AESA subsystem. Operatively, the SBR raster scans a VoI with a single pencil beam (hopping every few milliseconds) and exploiting the entire transmit peak power of the AESA subsystem. In this case, TWS [123,124] is clearly a formidable task against hyper-velocity target scenarios whereas PWS [63] appears as a promising contacts collection strategy, especially for fine radiometric measurements of a High Value Target (HVT) over a reduced VoI. Definitely, surveillance operations via a SIMO configuration can be further improved

adopting a larger multichannel cardinality on receive (at the cost of an increased onboard payload complexity). For example, the SBR may use a spoiled transmit beam and form several simultaneous pencil beams on receive via a Digital Beam Forming Network (DBFN) (see [125, Fig. 1b]). This approach has a number of benefits, including better target angular resolution along with possible receive adaptivity in hostile environments (provided that a sufficient number of receive channels are available). Yet, surveillance operations relying on a spoiled beam on transmit allows illuminating only a slightly larger volume compared to that subtended by an unspoiled beam. Therefore, even in this case, surveillance operations are constrained to scan a large VoI by hopping still-too-narrow a transmit beam in many sequential time slots (whereby TWS is still a daunting strategy). Alternatively, it is possible to illuminate a large VoI with a single transmit beam during a time slot using only a reduced portion of the AESA surface and (then) form different simultaneous pencil beams on receive via a DBFN (see [125, Fig. 1c]). Albeit in this case TWS tasks become possible, such an approach cannot benefit from a significant Effective Isotropic Radiated Power (EIRP) whereas the DBFN can recover power gain solely via the receive beams. Consequently, in order to overtake the aforementioned difficulties for SSA based on a SIMO SBR operating in TWS, a novel fully-polarimetric superheterodyne transceiver is introduced in this chapter capitalizing on a Multiple Input Multiple Output (MIMO) configuration (to the detriment of an additional onboard payload complexity).

The rest of the chapter is organized as follows. Section 1 presents the MIMO SBR sensor, the data structure, and operative strategies. Section 2 clarifies further details of the MIMO SBR functional architecture, including ancillary notes for critical MIMO aspects. Section 3 provides numerical results for the signal processor.

4.1 MIMO SBR Sensor, Data, and Operative Strategies

This section outlines the MIMO SBR functional architecture along with timing hierarchies in surveillance mode, the complex data hyper-cube structure, and the L-PRF RRRS tailored to Track While Simultaneous Search (TWSS).

4.1.1 Functional Architecture of the MIMO SBR Sensor

A high level functional architecture of the MIMO SBR transceiver is shown in Fig. 4.1 entailing N_T transmit channels at a given polarization q , i.e., TX_s^q (for $s = 1, \dots, N_T$, with $N_T = 16$, and q either H or V) and N_R receive channels per receive-polarization, i.e., RX_g^p (for $g = 1, \dots, N_R$, with $N_R = 4$, and p either H or V). As shown in Fig. 4.1, the architecture includes a reference USO for generating all the required LO frequencies coherently locked to the USO via PLLs, as well as a general purpose RISC fault tolerant μP for SBR management. In simple terms, N_T waveforms are synthesized inside N_T AWGs, upconverted to the K_a -band, and radiated into space via N_T AESA subarrays. On receive, target echoes impinging on N_R AESA subarrays are downconverted to an IF and digitized onto N_R channels for each receive polarization (i.e., 4 channels on H and V , respectively). The complex envelope extraction process for the $2N_R$ channels is assembled into a complex data hyper-cube within an echo digitizer whereby each sample is represented by the I/Q components (see the I/Q functional block scheme in Fig. 4.1). Hence, the acquired complex samples from the $2N_R$ channels are jointly processed through a digital chain made of phase rotators cascaded with a set of MFs, a MIMO-based DBFN, and a CFAR-

like detection block. Finally, the data stream is fed to the data-processor for tracking purposes. For onboard tracking in limited time spans on the order of hundreds of milliseconds, specific parameter estimates pave the way for further Bayesian inference on small-size debris dynamic states [59] as well as on RCS-related signatures [36] (namely, the target range parameter r , the target elevation and azimuth angles parameters θ and φ , respectively, and the target RCS parameter σ_{RCS}). Further details on Fig. 4.1 will be addressed in Section 4.2.

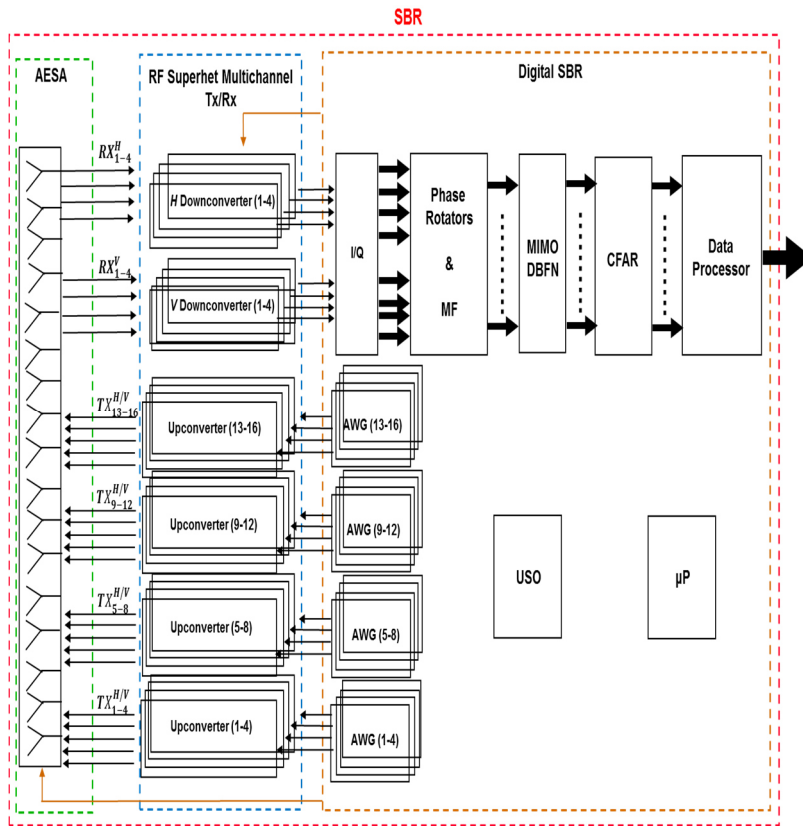


Fig. 4.1. MIMO SBR functional architecture.

4.1.2 Time Hierarchies and Complex Data Hyper-Cube

Considering a surveillance mode, an orbiting SBR (i.e., the red dot moving in the direction of the blue arrow in Fig. 4.2) raster-scans a VoI (i.e., the black dashed box in Fig. 4.2) during a frame interval. In particular, a frame is parsed into consecutive dwells, whereby at each dwell the SBR illuminates with a broad beam a large portion of the VoI referred to as a Sub-VoI (see the Sub-VoI beam in Fig. 4.2).

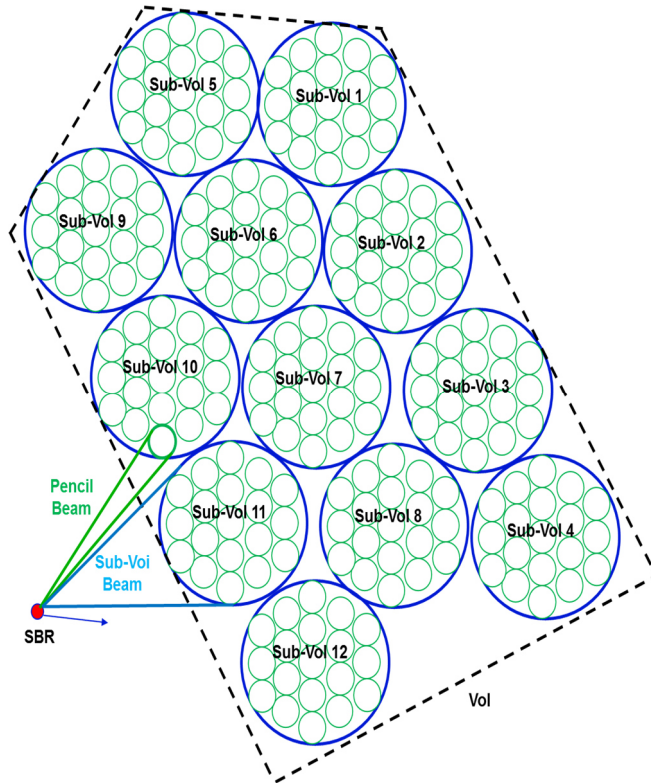


Fig. 4.2. MIMO SBR VoI, Sub-VoIs, and pencil beams.

For example, in Fig. 4.2 the SBR raster-scans the entire VoI during a frame made of 12 consecutive dwells by hopping the Sub-VoI beam on transmit from Sub-VoI 1 (during dwell 1), to Sub-VoI 2 (during dwell 2), and so on until reaching Sub-VoI 12 (during dwell 12). The surveillance of a given Sub-VoI during a dwell pertains to the formation of a number of multiple (simultaneous) narrow pencil beams synthesized via MIMO processing inside the Sub-VoI (see the green shapes inside each Sub-VoI in Fig. 4.2).

Accordingly, during a dwell spanning a few PRIs, the SBR illuminates a specific Sub-VoI (identified by a given θ_{sub} , φ_{sub} direction) with N_T (pseudo-orthogonal) transmit waveforms (temporally and spatially overlapped) and retrieves echoes from the Sub-VoI on $2N_R$ channels. Consequently, the set of I/Q components extracted from the $2N_R$ channels can be represented as a 4-D complex data hyper-cube (Fig. 4.3) comprising the following dimensions:

- a) The fast-time dimension, ξ_{fast} , which pertains to the complex samples acquired within a PRI.
- b) The slow-time dimension, ξ_{slow} , which indicates the number of PRIs (and therefore the number of transmitted pulses).
- c) The MIMO receive spatial dimension, $\xi_{MIMO-RX}$, which describes the RX_g^p channels for $g = 1, \dots, N_R$ (at a given receive polarization p).
- d) The receive polarization dimension, ξ_{pol} , which refers to $p = H$ and $p = V$.

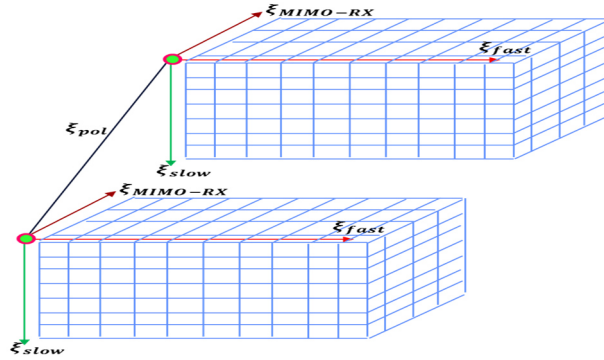


Fig. 4.3. MIMO SBR complex data hyper-cube during a dwell related to a specific Sub-VoI downstream the I/Q extraction block.

For the sake of clarification, the uppermost and lowermost drawings in Fig. 4.3 account for the complex data hyper-cube in the ξ_{fast} , ξ_{slow} , and $\xi_{MIMO-RX}$ dimensions with ξ_{pol} pertaining to $p=H$ and $p=V$, respectively. Also, the 4-D complex data hyper-cube shown in Fig. 4.3 represents raw data of the MIMO SBR downstream the I/Q extraction block⁹.

4.1.3 L-PRF RRRS and TWSS Strategy

The L-PRF RRRS has been detailed in chapter 2 for the SIMO SBR and will be further tailored hereafter to the MIMO SBR. That is, during a dwell on the order of a few milliseconds (say, 2 or 4 ms), a specific Sub-VoI is illuminated with a number of pulses (say, 2 or 4 pulses) at a L-PRF (e.g., 1 or 2 kHz) and a medium transmit duty-cycle. On receive, each of the aforementioned pencil beams formed within a Sub-VoI envelopes a set of range-gates cascaded in slant range. As clarified in chapter

⁹ For comparison, Fig. 2.4 represents the 5-D complex data hyper-cube of the SIMO SBR upstream the MF, thus including ξ_{Dop} (while the $\xi_{MIMO-RX}$ dimension is renamed as ξ_{mon}).

2, in this case a target is range non-ambiguous in the fast-time, and highly Doppler ambiguous in the slow-time. Accordingly, a bank of frequency offsets is applied directly in the fast-time to a group of MFs in parallel. This is equivalent to a filter bank in the fast-time with a group of Doppler frequency offsets not for estimating a target radial velocity but rather as a means to enforce Doppler tolerance on the PC scheme. After properly combining the available echo diversities (i.e., relying on waveform-based and spatial coherent-combining, temporal noncoherent-combining, and polarimetric noncoherent-combining), the frequency-offset at a given range-gate inducing the minimum residual-Doppler-frequency (and, therefore, the minimum MF loss) cues an estimate of the echo-range-rate (embedding the relative radial velocity between the SBR and the debris). The aforementioned scheme is defined as L-PRF RRRS applied to a MIMO SBR for SSA.

Within each pencil beam formed within a Sub-VoI, the L-PRF RRRS allows framing a set of CUTs where each CUT is identified by the triplet r, θ, φ . This, in turn, allows pondering whether or not a debris (or debris cloud) might be present inside the CUT as a binary hypothesis test. Accordingly, the TWSS contacts collection strategy (based on L-PRF RRRS) provides a detection map of all CUTs pertaining to all pencil beams formed within a Sub-VoI during a dwell (and, eventually, within all Sub-VoIs during a frame). On top of that, at every frame the onboard Bayesian tracker can process measurements either as thresholded or unthresholded data for MTT [59] of debris clouds in the VoI.

Thus, with a MIMO SBR there is no need for a PWS contact collection strategy since every Sub-VoI is frequently revisited in a round-robin fashion (being the number of Sub-VoIs limited by design). Also, in a MIMO SBR the entire transmit power resources of the AESA subsystem are fully exploited for illuminating a Sub-VoI (since the entire AESA surface is parsed into N_T transmit-subarrays). Finally, compared to the available

degrees of freedom of a SIMO configuration with N_R receive channels, a MIMO framework (with N_T and N_R transmit and receive channels, respectively) allows for better angular resolution, targets identifiability, and interference rejection capabilities, [126-129] (provided that a sufficient number of transmit-receive channels are available).

4.2 Details on the MIMO SBR Functional Architecture

Further details of the MIMO SBR functional architecture are addressed hereafter, predominantly via key comparisons with the SIMO SBR proposed in chapter 2. In addition, ancillary notes take into account MIMO radar theory (e.g., [126-129]) and ponder MIMO-related critical aspects (e.g., [125, 130-132]).

4.2.1 AWGs and Upconversions

The MIMO SBR functional architecture shown in Fig. 4.1 depicts N_T transmit channels fed by N_T independent AWGs. Each AWG generates a (pseudo-orthogonal) transmit waveform based on DDS [66] whereby different waveform types can be flexibly programmed. To this end, Code Division Multiplexing (CDM) represents a design option to generate (pseudo-orthogonal) transmit waveforms whereby the transceiver bandwidth is framed by the Direct-Sequence Spread-Spectrum (DS-SS) scheme [133]. Indeed, considering a coherent MIMO SBR (whose detection capabilities for SSA can rely solely on few pulses during a dwell), a CDM-based paradigm (whereby the N_T transmit channels occupy the same frequency support) allows limiting the receiver Noise Figure (NF) and frequency-selectivity in case of plasma turbulence.

Interestingly, the methodology to select MIMO waveforms is quite variable in literature. For example, several works deal with the synthesis of a desired transmit beampattern by first identifying a waveform correlation matrix and then finding a set of waveforms abiding by such correlations [134-137]. Information-theoretic approaches for MIMO waveform design are covered for example in [138] and [139]. Optimization techniques for MIMO waveform design are addressed in [140] to maximize the Signal to Interference plus Noise Ratio (SINR). Other works focus directly on devising waveforms based on Non Linear-Frequency-Modulation (N-LFM) [141] or TanSec Frequency Modulation (TSFM) [142]. These latter efforts are tailored mostly to automotive applications whereas very limited results appear in case of a significant Doppler stress on the MIMO receiver scheme [143]. Now, the selection of a specific class of waveforms for the CDM-based MIMO SBR is outside the scope of this chapter. In fact, the intent of this chapter is to conceive a programmable architecture for a CDM-based MIMO SBR which is independent of the class of waveforms. Indeed, as novel waveform families emerge, the SBR AWGs can be reprogrammed while the parallelization required in the digital receiver can be scaled (as it will be further clarified in § 4.2.3 and § 4.3). In particular, the approach adopted in this article relies on a reference benchmark based on synthesizing (on each of the 16 AWGs) LFM pulses (including LFM-unmodulated pulses i.e., with no LFM slope) with a medium transmit duty-cycle. Each LFM waveform is further phase-modulated (within pulse) by a specific code [144]. Within this context, one may note that with roughly 100 μs of pulse duration on transmit the minimum operative slant range from the SBR is roughly 15 km (thus well within the Fraunhofer region in the K_a -band with an AESA area on the order of 1 m^2). Accordingly, it is possible to generate a code period $P = 2^7 - 1$ with a chip time $T_c = 1 \mu\text{s}$ (i.e., with a DS-SS roughly over a bandwidth $\mathcal{B} = 1 \text{ MHz}$). Alternatively,

one can adopt a $\mathcal{T}_c = 0.5 \mu\text{s}$ over a bandwidth $\mathcal{B} = 2 \text{ MHz}$ to synthesize a code period $P = 2^8 - 1$. The synthesis of such waveforms can be easily obtained with high spectral purity and accuracy via an efficient waveform descriptor related to P code symbols and four parameters, i.e., start phase φ_0 , start frequency f_{UHF} , LFM slope K_0 , and pulse duration \mathcal{T} (the amplitude parameter \mathcal{A} can be programmed as well). Specifically, the s th AWG (for $s = 1, \dots, N_T$) generates a single-pulse waveform in time (t) directly on a carrier in the UHF band (e.g., $f_{UHF} \sim 500 \text{ MHz}$), i.e.,

$$s_{UHF,s}(t) = \mathcal{A} \cdot \cos \left[2\pi f_{UHF}t + 2\pi \frac{1}{2} K_0 t^2 + \varphi_0 + \pi c_s(t) \right] \cdot \text{rect} \left(\frac{t - \mathcal{T}/2}{\mathcal{T}} \right) \quad (4.1)$$

with

$$c_s(t) = \sum_{\eta=1}^P c_{s,\eta} \text{rect} \left(\frac{t - (\eta-1)\mathcal{T}_c - \frac{\mathcal{T}_c}{2}}{\mathcal{T}_c} \right) \quad (4.2)$$

where $c_s(t)$ is the s th code waveform, $c_{s,\eta} \in \{0,1\}$ (for $\eta = 1, \dots, P$) is the η th symbol of the s th code waveform, and $\mathcal{T} = P\mathcal{T}_c$. Downstream the waveform synthesis in the UHF Band, the RF upconversion chain for each of the N_T transmit waveforms translates the UHF waveform to the K_α -band. Fig. 4.4 hints a possible frequency translation of the s th transmit channel based on PLLs relying on a first upconversion stage in the \mathcal{C} -band (e.g., $f_C \sim 5.5 \text{ GHz}$) and a second upconversion stage in the K_α -band (e.g., $f_{K\alpha} \sim 35.5 \text{ GHz}$). Consequently, the s th single-pulse signal fed to the AESA subsystem can be written as

$$s_{K\alpha,s}(t) = \mathcal{A}_1 \cdot \cos \left[2\pi f_{K\alpha}t + 2\pi \frac{1}{2} K_0 t^2 + \varphi_0 + \pi c_s(t) \right] \cdot \text{rect} \left(\frac{t - \mathcal{T}/2}{\mathcal{T}} \right) \quad (4.3)$$

where the \mathcal{A}_1 parameter also accounts for the tunable output power to properly drive the AESA subsystem input.

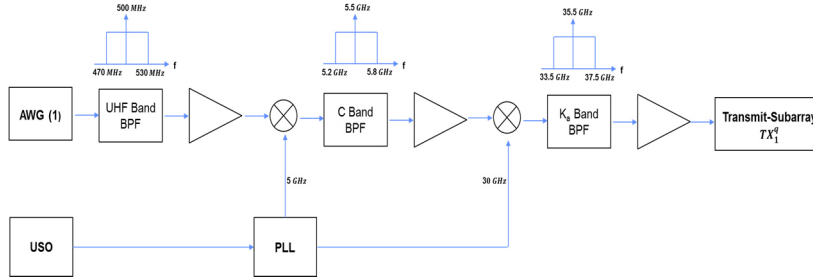


Fig. 4.4. Upconverter frequency plan for the s th channel.

The structure of the upconversion chain in Fig. 4.4 has not changed with respect to the SIMO counterpart outlined in chapter 2 (albeit the number of transmit channels of the MIMO SBR has increased from 1 to N_T). Interestingly, this paves the way for a flexible SBR payload, possibly switching between TWSS and PWS operations. Indeed, (using the same RF subsystem) in the former case the N_T AWGs would transmit independent waveforms towards N_T independent transmit-subarrays within the AESA subsystem (as per a nominal MIMO configuration). In the latter case, the N_T AWGs would transmit (coherently) the same waveform towards the N_T transmit-subarrays (as per a SIMO configuration).

4.2.2 AESA Subsystem

After upconversion to the K_a -band, the s th transmit waveform (for $s = 1, \dots, N_T$) is distributed via a power-divider towards the radiating elements of the s th transmit-subarray within the AESA subsystem. On the receive side, the radiating elements of the g th receive-subarray (for $g = 1, \dots, N_R$) interface 2 receive-power-combiners (i.e., 1 for the H and 1 for the V polarization, respectively) conveyed towards 2 RF downconverters, respectively (thus, resulting in $2N_R$ RF receive channels in total).

As hinted in chapter 2, paramount electrical, electromagnetic, mechanical, and thermal aspects need to be faced with such an AESA subsystem. To begin with, the quad-pol characteristics of the MIMO SBR can be implemented relying on radiating elements supporting both H and V polarizations. In order to illuminate a specific Sub-VoI (located in a given θ_{Sub} , φ_{Sub} direction), the narrowband assumption of the waveforms spectrum (i.e., a few megahertz) allows for an ABFN at subarray-level based on phase-shifters instead of TTDL. Besides, each subarray comprises several solid state HPAs on transmit and LNAs on receive integrated within T/R modules. It appears from public proceedings that remote sensing applications with space qualified T/R modules in the K_a -band are still limited (e.g., see [145] and [146]) while the TRL of GaN-based MMIC devices moves steadily forward [147, 148]. To this end, fruitful SBR operations for SSA are expected to rely on sufficient EIRP over (say roughly) 100 km of slant range with maximum beam-steering angles of (say roughly) 50° with respect to broadside. This drives once again the design of one T/R module for each radiating element (as per the SIMO SBR in chapter 2). Hence, pitch accommodation, mechanical distortion, displacement of mass, electromagnetic coupling effects, heat dispersion, and ABFN integration must be thoroughly pondered. In particular, the minimum inter-element displacement on a regular array lattice has a key influence on the maximum off-broadside scanning angle without sprouting grating lobes. Interestingly, for a K_a -band AESA on a regular array topology the transmit peak power can be significantly increased with a slight augmentation of either T/R module peak power or antenna area (see Figs. 2.10 and 2.11). Therefore, in order to cope with thermal requirements and proper allocation of heat pipes [149], a scalable design of the instrument FoV can be obtained by a reasonable trade-off between slightly enlarging the AESA lattice

area (say, roughly on the order of 1 m^2) and increasing T/R modules transmit peak power.

On top of these insights, requirements against grating lobes for a subarray-based MIMO AESA affect not only inter-element distances within a subarray but also inter-subarray distances within the AESA [150]. In other words, for a MIMO SBR the general functional requirements on beam directivity (e.g., beamsteering, beamwidth, and beamshape) must be conceived on a two-level beam-forming hierarchy. The first one pertains to the ABFN at subarray level (i.e., N_T ABFNs for forming the N_T transmit beams and $2N_R$ ABFNs for generating N_R receive beams on H and V , respectively). The second level is related to the MIMO DBFN (i.e., the DBFNs acting on the so-called MIMO super-array of size $N_T N_R$ [150] for generating multiple transmit-receive narrow beams within a Sub-VoI). De facto, manufacturing efforts strive for reducing the inter-element distance within a subarray regular lattice as close as possible to $\lambda/2$. Thus, adjacent (noncoincident) phase-centers of the MIMO super-array are likely to lie at a distance much larger than $\lambda/2$. Therefore, in order to avoid grating lobes at super-array level, one must enforce the removal of a Vandermonde structure on the super-array manifold by breaking any periodicity of the super-array lattice. This aspect is not trivial (see for instance [150]) and can be tackled considering unconventional array architectures [73]. For example, the ELRA multichannel AESA subsystem [150,151] relies on irregularly thinned subarrays of variable size and shape. In [152] a subarray surface is assembled via different polyomino-based tiles. Also, [153] describes arrays based on polygon-tiles of variable orientation with a number of elements regularly displaced on the tile. Other works (e.g., [154] and [155]) pursue packing-optimization-strategies on regular lattices based on domino-tiles, viz., 2 radiating elements belonging to either a Vertical (\mathcal{V}) or Horizontal (\mathcal{H}) domino-tile (where each element of a tile is excited by the same complex coefficient).

Interestingly, in a MIMO AESA one can form irregularities among the positions of the phase-centers of the MIMO super-array manifold, starting from a bespoke assembly of domino-tiles at subarray level. To this end, let us first consider the geometry of a tile-based subarray (either a transmit-subarray or a receive-subarray) whose radiating elements are regularly displaced with mutual distance d on a plane spanned by the \hat{x} and \hat{y} axes with broadside direction located on the \hat{z} axis (see Fig. 4.5).

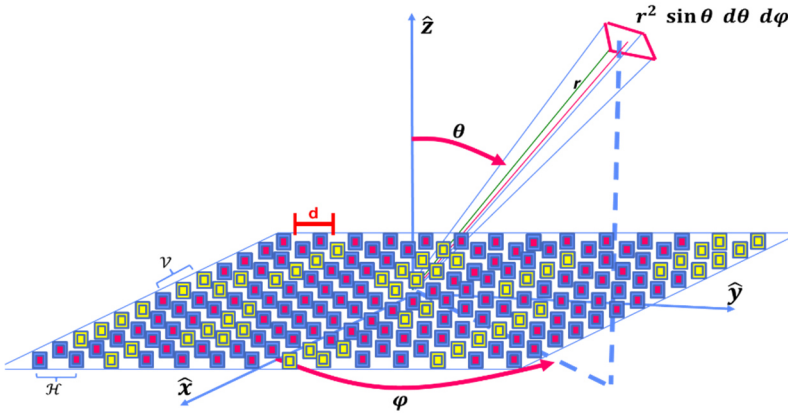


Fig. 4.5. Pictorial representation of a tile-based subarray. \mathcal{V} and \mathcal{H} domino-tiles depicted in yellow and purple color, respectively.

In particular, the domino-tiles are pictorially represented as an assembly of couples-of-yellow-dots along the \hat{x} axis (i.e., \mathcal{V} domino-tiles) and couples-of-purple-dots along the \hat{y} axis (i.e., \mathcal{H} domino-tiles). For the sake of clarification, Fig. 4.5 also shows a differential solid angle $d\Omega = \sin \theta d\theta d\varphi$ subtending the differential area $dA = r^2 \sin \theta d\theta d\varphi$ identified by the spherical triplet (r, θ, φ) with respect to a given subarray-phase-center reference. Remarkably, for a required subarray radiation pattern an optimum assembly of domino-tiles (along with the related complex coefficients excitation) can be computed by solving a

so-called “*domino tiled array synthesis problem*” via so-called Enumerative Tiling Methods (ETM) or Optimization Tiling Methods (OTM) [154,155]. Considering a 2-D array of $L \times M$ radiating elements (where the location of the (l, m) -th element is at (x_l, y_m) , $l = 1, \dots, L$, $m = 1, \dots, M$, on the \hat{x} and \hat{y} axes, respectively) a given assembly of Q domino-tiles can be characterized by a specific *tile-clustering-set* $\mathbf{b} = \{b_{lm} \in [1, \dots, Q] | l = 1, \dots, L, m = 1, \dots, M\}$ and a *tile-complex-set* $\mathbf{w} = \{w_q \in \mathbb{C} | q = 1, \dots, Q\}$ indicating the complex coefficients of the radiating elements of the Q tiles. For instance, in Fig. 4.5 $L = 13$, $M = 14$, and $Q = 91$ whereby the bottom line-set of radiating elements along the \hat{y} axis encompasses 9 domino-tiles (i.e., from left to right: $\mathcal{H}, \mathcal{V}, \mathcal{H}, \mathcal{H}, \mathcal{V}, \mathcal{V}, \mathcal{H}, \mathcal{V}, \mathcal{H}$) whose radiating elements are identified by a component of \mathbf{b} and \mathbf{w} . In this case, the radiating elements of the bottom line-set are identified (for example) as 1, 1, 2, 3, 3, 4, 4, 5, 6, 7, 7, 8, 9, 9, for \mathbf{b} and $w_1, w_1, w_2, w_3, w_3, w_4, w_4, w_5, w_6, w_7, w_7, w_8, w_9, w_9$, for \mathbf{w} , respectively. Accordingly, a domino-tile-based array factor can be written as a function of a specific \mathbf{b} , \mathbf{w} , and direction cosines $u = \sin \theta \cos \varphi$, $v = \sin \theta \sin \varphi$ with respect to the subarray direction cosines u_{sub}, v_{sub} (see also [155, eq. (1)]), i.e.,

$$AF_{\mathbf{b}, \mathbf{w}, u_{sub}, v_{sub}}(u, v) = \sum_{l=1}^L \sum_{m=1}^M \sum_{q=1}^Q w_q \times \delta_{b_{lm}q} e^{jk[x_l(u-u_{sub})+y_m(v-v_{sub})]} \quad (4.4)$$

where $k = 2\pi/\lambda$ is the wavenumber and $\delta_{\alpha\beta}$ is the Kronecker delta, i.e., $\delta_{\alpha\beta} = 1$ for $\alpha = \beta$, and $\delta_{\alpha\beta} = 0$ for $\alpha \neq \beta$. Considering a general phase center analysis for an AESA [150, 156] and taking into account operations in the Fraunhofer region, an approximation of the phase-center of a subarray characterized by \mathbf{b} and \mathbf{w} (namely, $\rho_{\mathbf{b}, \mathbf{w}, x}$ and $\rho_{\mathbf{b}, \mathbf{w}, y}$ on the \hat{x} and \hat{y} axes,

respectively) can be computed as the centroid of the element positions weighted by the modulus value of the complex excitation coefficients (see also [156, eq. (5)] in case of linear phased arrays), i.e.,

$$\rho_{\mathbf{b},\mathbf{w},x} = \frac{\sum_{l=1}^L \sum_{m=1}^M \sum_{q=1}^Q |w_q \delta_{b_{lmq}}| x_l}{\sum_{l=1}^L \sum_{m=1}^M \sum_{q=1}^Q |w_q \delta_{b_{lmq}}|} \quad (4.5)$$

$$\rho_{\mathbf{b},\mathbf{w},y} = \frac{\sum_{l=1}^L \sum_{m=1}^M \sum_{q=1}^Q |w_q \delta_{b_{lmq}}| y_m}{\sum_{l=1}^L \sum_{m=1}^M \sum_{q=1}^Q |w_q \delta_{b_{lmq}}|} \quad (4.6)$$

Interestingly, for a given (u_{sub}, v_{sub}) pair, different combinations of \mathbf{b} and \mathbf{w} provide a means to exert a variability of $\rho_{\mathbf{b},\mathbf{w},x}$ and $\rho_{\mathbf{b},\mathbf{w},y}$. Such a variability can be applied (independently) to the phase-center of each of the N_T transmit-subarrays and N_R receive-subarrays of the MIMO AESA subsystem while illuminating a specific Sub-VoI.

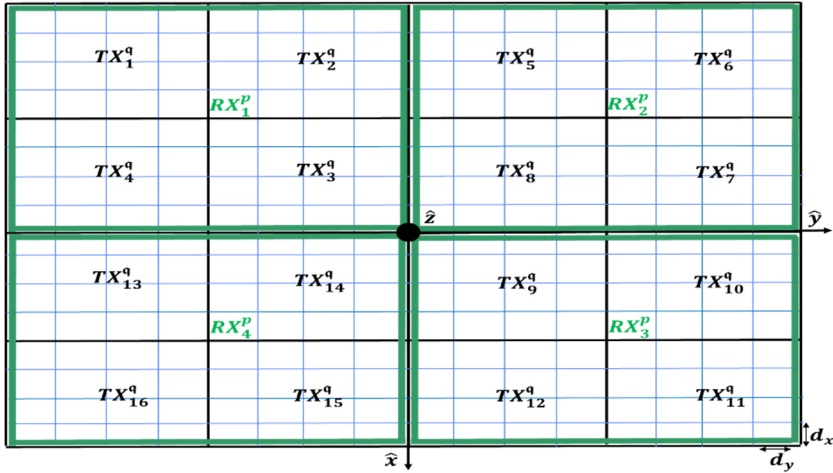


Fig. 4.6. MIMO AESA based on subarrays (transmit-subarrays labeled by TX_s^q , for $s = 1, \dots, 16$; receive-subarrays labeled by RX_g^p , for $g = 1, \dots, 4$).

To this end, Fig. 4.6 depicts a possible partitioning of the AESA surface into specific transmit and receive subarrays shapes. Specifically, the perimeters of the transmit-subarrays (i.e., TX_s^q , for $s = 1, \dots, 16$) are represented by black rectangles while those of the receive-subarrays (i.e., RX_g^p , for $g = 1, \dots, 4$) by green rectangles. As shown in Fig. 4.6, the perimeters of the aforementioned subarrays follow a regular pattern on the \hat{x} and \hat{y} axes of the AESA surface centered on the \hat{z} axis. Namely, the transmit and receive subarray perimeters are superimposed on a regular grid whose units of measure are d_x and d_y along the \hat{x} and \hat{y} axes, respectively. Each transmit and receive subarray area is $16d_x d_y$ and $64d_x d_y$, respectively, whereas the areas of the transmit-subarrays as well as those of the receive-subarrays are nonoverlapped to aid manufacturing, decrease coupling, and avoid intermodulations on transmit. Consequently, the phase-centers of the transmit and receive subarrays with respect to the AESA center can be written as

$$\zeta_{\mathbf{b}_s, \mathbf{w}_s, x}^{TX} = \rho_{\mathbf{b}_s, \mathbf{w}_s, x}^{TX} + h_{s,x}^{TX}; \quad \zeta_{\mathbf{b}_g, \mathbf{w}_g, x}^{RX} = \rho_{\mathbf{b}_g, \mathbf{w}_g, x}^{RX} + h_{g,x}^{RX} \quad (4.7)$$

for the coordinates on the \hat{x} axis and as

$$\zeta_{\mathbf{b}_s, \mathbf{w}_s, y}^{TX} = \rho_{\mathbf{b}_s, \mathbf{w}_s, y}^{TX} + h_{s,y}^{TX}; \quad \zeta_{\mathbf{b}_g, \mathbf{w}_g, y}^{RX} = \rho_{\mathbf{b}_g, \mathbf{w}_g, y}^{RX} + h_{g,y}^{RX} \quad (4.8)$$

for those on the \hat{y} axis. In this case, the $(h_{s,x}^{TX}, h_{s,y}^{TX})$ pair indicates the coordinates of the s th transmit-subarray reference (e.g., its center) with respect to the AESA center while the $(\rho_{\mathbf{b}_s, \mathbf{w}_s, x}^{TX}, \rho_{\mathbf{b}_s, \mathbf{w}_s, y}^{TX})$ pair represents the coordinates of the s th transmit-subarray phase-center with respect to the $(h_{s,x}^{TX}, h_{s,y}^{TX})$ pair (similar definitions apply to the phase-centers of the receive-subarrays). As an example, in Fig. 4.6 for the TX_8^q transmit-subarray $h_{8,x}^{TX} = -2d_x$ and $h_{8,y}^{TX} = 2d_y$ whereas (taking into

account a given \mathbf{b}_8^{TX} and \mathbf{w}_8^{TX} $\rho_{\mathbf{b}_8, \mathbf{w}_8, x}^{TX}$ and $\rho_{\mathbf{b}_8, \mathbf{w}_8, y}^{TX}$ are computed by eqs. (4.5) and (4.6), respectively. Now, let us consider all transmit and receive subarrays pointing towards a common Sub-VoI cued by a (u_{sub}, v_{sub}) pair. Accordingly, let us define the *AESA-tile-clustering-set* as $\mathbf{B}_{u_{sub}, v_{sub}} = \{\mathbf{b}_{u_{sub}, v_{sub}, s}^{TX} | s = 1, \dots, N_T\} \cup \{\mathbf{b}_{u_{sub}, v_{sub}, g}^{RX} | g = 1, \dots, N_R\}$ in which $\mathbf{b}_{u_{sub}, v_{sub}, s}^{TX}$ and $\mathbf{b}_{u_{sub}, v_{sub}, g}^{RX}$ are the relative *tile-clustering-set* of the s th transmit-subarray and g th receive-subarray, respectively. Similarly, let us address the *AESA-tile-complex-set* as $\mathbf{W}_{u_{sub}, v_{sub}} = \{\mathbf{w}_{u_{sub}, v_{sub}, s}^{TX} | s = 1, \dots, N_T\} \cup \{\mathbf{w}_{u_{sub}, v_{sub}, g}^{RX} | g = 1, \dots, N_R\}$ such that $\mathbf{w}_{u_{sub}, v_{sub}, s}^{TX}$ and $\mathbf{w}_{u_{sub}, v_{sub}, g}^{RX}$ account for the relative *tile-complex-set* of the s th transmit-subarray and g th receive-subarray, respectively. Besides, let us express $\mathcal{X}_{sub} = \mathbf{B}_{u_{sub}, v_{sub}} \cup \mathbf{W}_{u_{sub}, v_{sub}}$. Also, for a given $\mathbf{b}_{u_{sub}, v_{sub}, s}^{TX}$ and $\mathbf{w}_{u_{sub}, v_{sub}, s}^{TX}$ let us represent the phase-center of the s th transmit-subarray (with respect to the AESA center) as the $(\zeta_{\mathbf{b}_{u_{sub}, v_{sub}, s}^{TX}, \mathbf{w}_{u_{sub}, v_{sub}, s}^{TX}}}^{TX}, \zeta_{\mathbf{b}_{u_{sub}, v_{sub}, s}^{TX}, \mathbf{w}_{u_{sub}, v_{sub}, s}^{TX}}}^{TX})$ pair (similar definitions apply to the phase-center of the g th receive-subarray). Consequently, for a given \mathcal{X}_{sub} the array factor of the *MIMO-super-array* (see also [150, eq. (1.22)]) can be formulated as a function of the direction cosines (u, v) with respect to the pencil beam direction cosines (u_0, v_0) generated within the Sub-VoI cued by the (u_{sub}, v_{sub}) pair, i.e.,

$$AF_{u_{sub}, v_{sub}, u_0, v_0}(u, v) = \sum_{s=1}^{N_T} \sum_{g=1}^{N_R} \zeta_{u_{sub}, v_{sub}, u_0, v_0, s, g}^* \times e^{j2k[u \zeta_{u_{sub}, v_{sub}, s, g, x} + v \zeta_{u_{sub}, v_{sub}, s, g, y}]} \quad (4.9)$$

whereby (for a given $u_{sub}, v_{sub}, u_0, v_0$ and considering $s = 1, \dots, N_T, g = 1, \dots, N_R$), $\zeta_{u_{sub}, v_{sub}, u_0, v_0, s, g} \in \mathbb{C}$ is the MIMO super-

array complex weight coefficient, $(\cdot)^*$ indicates complex conjugation, and

$$\zeta_{u_{sub},v_{sub},s,g,x} = \frac{\zeta_{b_{sub},v_{sub},s,w_{sub},v_{sub},s,x}^{TX} + \zeta_{b_{sub},v_{sub},s,w_{sub},v_{sub},g,x}^{RX}}{2} \quad (4.10)$$

$$\zeta_{u_{sub},v_{sub},s,g,y} = \frac{\zeta_{b_{sub},v_{sub},s,w_{sub},v_{sub},s,y}^{TX} + \zeta_{b_{sub},v_{sub},s,w_{sub},v_{sub},g,y}^{RX}}{2} \quad (4.11)$$

are the position of MIMO super-array phase-centers on the \hat{x} and \hat{y} axes, respectively (see also [128]). Within this framework, the MIMO super-array complex weight vector for Direct Subarray Weighting (DSW) [150] is $\zeta_{u_{sub},v_{sub},u_0,v_0} = [\zeta_{u_{sub},v_{sub},u_0,v_0,1,1}, \dots, \zeta_{u_{sub},v_{sub},u_0,v_0,N_T,N_R}]^T \in \mathbb{C}^\Gamma$ in which $[\cdot]^T$ indicates matrix transpose and $\Gamma = N_T N_R$. Γ is the keystone which entails (potentially) significant degrees of freedom for array processing and a high angular resolution of each pencil beam within a Sub-VoI (provided that d_x and d_y are sufficiently large). Further insights on the subarray-based AESA follow next.

First of all, if the phase-center of each subarray were exactly at the center of its own circumscribing rectangle (see the blue dots and the green dots in Fig. 4.7 for the transmit and receive subarrays, respectively), the Γ phase-centers of the *MIMO-super-array* would be regularly displaced within the interior of the AESA surface (see the red dots shown in Fig. 4.7). Moreover, this specific case would include a number of over-represented (i.e., coincident) phase-centers (e.g., see the 1, 2, and 4 numbers pictorially inscribed within the red dots in Fig. 4.7 to cue a single, two-fold, and four-fold phase-centers over-representation, respectively). In fact, under the approximation leading to eqs. (4.5) and (4.6) and considering eqs. (4.10)-(4.11), the phase-centers of the *MIMO-super-array* are still guaranteed

to belong to the interior of the AESA surface, yet displacing their position (thus, potentially breaking any over-representation and introducing an irregularity on the lattice). To this end, the irregularity of the Equivalent Linear Array (ELA) pertaining to different AESA cuts as a function of χ_{sub} , d_x , d_y represents a possible AESA design criterion to break any periodicity of the super-array lattice and avoid grating lobes at super-array level (see [150, § 1.3.3]).

Second, the subarrays depicted in Fig. 4.6 use the entire set of AESA T/R modules, with important benefits for AESA manufacturing as well as for subarray gain performance. Being the area of each receive-subarray overlapped onto 4 symmetrically-displaced transmit-subarrays (as shown in Fig. 4.6), the transmit-subarray beamwidth is nominally twice as large as that of the receive-subarray beamwidth. Yet, considering that transmit-subarrays are untapered (for power efficiency) while receive subarrays are tapered (for sidelobe control), it is possible to conceive surveillance operations based on transmit and receive subarrays with similar beamwidths.

Finally, it is worth pondering power demands and sensitivity taking into account [125] and [130]. In [125], the benefit of a MIMO paradigm with respect to a classical SIMO-based beamforming is stressed considering several aspects (mostly from a ship-based perspective), including Low Probability of Intercept (LPI), ubiquitous search over a large VoI, as well as operations against imposing mainbeam clutter returns over littoral regions without saturating the receiver. Notwithstanding such general MIMO benefits, [125] also comments that: *“Since the transmitted waveforms do not combine coherently in space, there is a loss in sensitivity equal to the loss in transmit array gain. This reduced sensitivity can be restored by integrating longer.”* Unfortunately, a MIMO SBR for SSA cannot leverage longer integration times in the slow-time, since targets hyper-velocity would inevitably induce range migration

on the MF scheme. Certainly, in a MIMO SBR for SSA one may slightly augment the transmit duty-cycle to improve detection performance (especially in case of low-RCS hyper-velocity targets). But upstream any possible detection inference, the main issue is to let an echo stimulate the receiver Analog to Digital Converter (ADC) above the Least Significant Bit (LSB). This can be tackled by increasing transmit subarray EIRP along with receive subarray gain. For this reason, in line with the concerns highlighted in [130], thermal conditioning is a paramount aspect in a MIMO SBR entailing an increase of T/R modules peak power capabilities and subarray lattice areas (to this end, Figs. 2.10 and 2.11 provide straightforward hints thereabout).

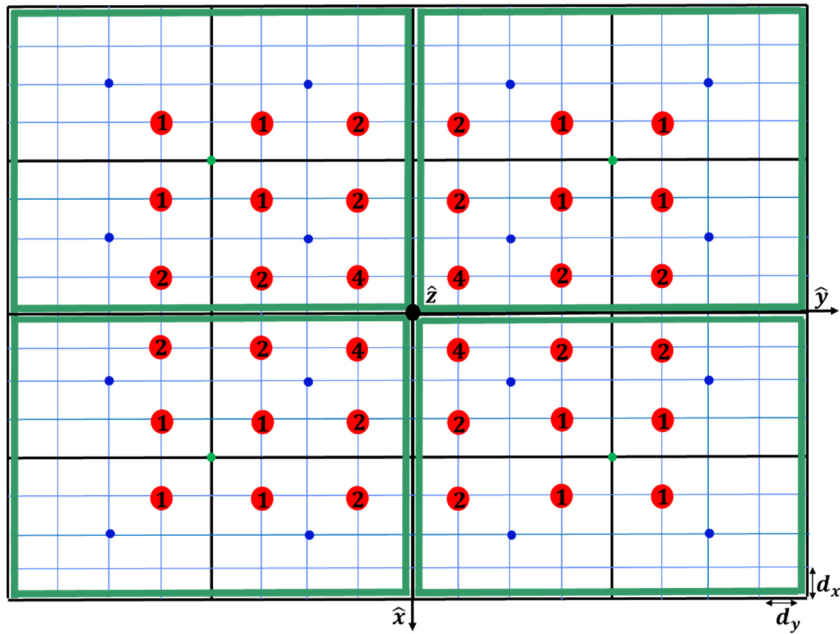


Fig. 4.7. Phase-centers single representation (1 inscribed within a red dot) and over-representation (2 or 4 inscribed within a red dot) of the MIMO-superarray (if the phase-center of each subarray were exactly at the center of its own circumscribing rectangle).

4.2.3 Downconversions and Complex Envelope Acquisition

Similarly to the RF architecture of the SIMO SBR addressed in chapter 2, the $2N_R$ downconverter chains translate the K_a -band echo signal from the $2N_R$ receive-subarray power combiners of the AESA subsystem down to a suitable IF towards the digital section. Again, the whole set of receive channels operates under the shared control of an AGC loop providing the instrument dynamic range with over 50 dB of gain control while the receiver chain applies a double-conversion superheterodyne scheme [80]. Fig. 4.8 indicates a possible frequency translation relying on a first downconversion stage in C Band and a second one in the High Frequency (HF) Band. In particular, the frequency plan assumes a Band Pass Filter (BPF) in the K_a -band centered at 35.515 GHz, a BPF in the C-band centered at 5.095 GHz, and a BPF in the HF Band centered at 25 MHz before the signal is digitized. As discussed in chapter 2, considering relative SBR-debris velocities up to 16 km/s, the Doppler effect on the received echoes at 36 GHz would result in a Doppler frequency shift f_d around 3.8 MHz. For this reason, the IF band pass is 10 MHz wide.

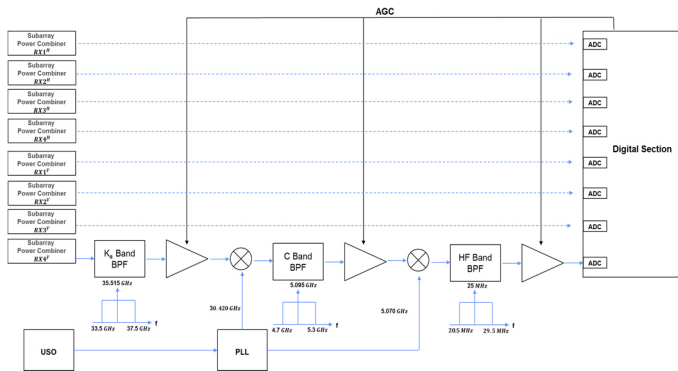


Fig. 4.8. Downconverter frequency plan for $2N_R$ receive channels.

The receive digital section is based on harmonic-sampling for each of the $2N_R$ IF signals using a single ADC for each channel (i.e., 8 ADCs as shown in Fig. 4.8), thus producing I/Q samples for each channel without phase and amplitude imbalances of a quadrature analog demodulator. Unlike SAR applications with distributed targets (to this end, see [132] for further insights on MIMO SAR), the SSA environmental scenario outlined in chapter 1 mainly cues the occurrence of point-like targets (namely, individual debris or debris clouds). In particular, from the SBR perspective a point-like target at Cartesian position \mathbf{p} within a CUT is identified by the spherical triplet r, θ, φ whereas the target velocity $\dot{\mathbf{p}}$ induces an echo Doppler frequency shift f_d . Accordingly, due to the narrowband assumption and considering that the SBR is a coherent colocated MIMO radar (see [157]), let us define $\tau_r = 2r/c$ as the target delay from the AESA center, D^p and φ_0^p as the target amplitude and phase, respectively (pertaining to RCS and signal propagation effects at receive-polarization p), $\mathbf{u}(\varphi, \theta) = [\cos \varphi \sin \theta, \sin \varphi \sin \theta, \cos \theta]^T$ as the unit direction vector (expressed as a function of φ and θ from the AESA center to the target), and $\boldsymbol{\zeta}_{u_{sub}, v_{sub}, s, g} = [\zeta_{u_{sub}, v_{sub}, s, g, x}, \zeta_{u_{sub}, v_{sub}, s, g, y}, 0]^T$. Consequently, the (noiseless) single-pulse echo of a point-like target on the RX_g^p channel (for $g = 1, \dots, N_R$, and $p = H, V$) can be approximated at ADC input as

$$z_{HF, g}^p(t) \cong \sum_{s=1}^{N_T} D^p \cos \left[2\pi(f_{HF} + f_d)t + \varphi_0^p + 2\pi \frac{1}{2} K_0 (t - \tau_r)^2 + \pi c_s (t - \tau_r) + 4\pi f_{Ka} \frac{\mathbf{u}^T(\varphi, \theta) \boldsymbol{\zeta}_{u_{sub}, v_{sub}, s, g}}{c} \right] \text{rect} \left(\frac{t - \tau_r - T/2}{T} \right) \quad (4.12)$$

Each addend in eq. (4.12) accounts for the point-like target echo from the s th transmit-subarray (for $s = 1, \dots, N_T$) to the g th receive-subarray at receive-polarization p . As clarified in chapters 1 and 2, $f_d = -2v/\lambda$ affects only the carrier of the echo whereby v cues the echo range-rate for all transmit-receive

subarrays pairs (i.e., independent of s and g). Notably, $v = \pm|\mathbf{v}|$ embedding the mutually unknown radial target-velocity (i.e., v_{target}) and SBR-velocity (i.e., v_{SBR}), i.e., $v = v_{SBR} - v_{target}$, such that an outward target motion is defined as positive (see also Fig. 2.13). Interestingly, the complex envelope of each of the N_T addends in eq. (4.12) is factorable in space-time (see [81] and [158-159]), namely, the angular components (i.e., θ and φ) and the temporal components (i.e., τ_r and f_D), respectively.

A description of the processing lineup from the $2N_R$ ADCs to the CFAR-like detection block input follows next (see Fig. 4.9). While the SBR illuminates a given Sub-VoI cued by a (u_{sub}, v_{sub}) pair during a dwell made of N_S PRIs, the $2N_R$ ADCs acquire at each PRI a number of samples pertaining to a SWL in the fast-time. The separation of the I/Q samples for each of the $2N_R$ ADCs is obtained by sampling at 20 MHz the HF signal centered at 25 MHz. Each ADC output is multiplied by a 1,0,-1,0,... sequence and 0,-1,0,1,0,... sequence for the I and Q branches, respectively, followed by an I&D LPF as per chapter 2. The aforementioned samples account for the complex data hypercube shown in Fig. 4.3. As clarified in chapter 2, the imposing value of f_d in eq. (4.12) is likely to induce significant losses on a MF magnitude response (depending on the waveform ambiguity function). For this reason, a suitable Doppler-frequency-offset f provides a means to reduce the residual-Doppler-frequency f_{res} (i.e., $f_{res} = f_d - f$) of the echo before a MF is applied in the fast-time. Accordingly, at the i -th PRI (for $i = 1, \dots, N_S$) the (g, p) -th I&D LPF output (for $g = 1, \dots, N_R$ and $p = H, V$) can be expressed as an $IQ_{i,g,p}[n]$ complex sequence in the fast-time (where $n = 1, \dots, SWL$ indicates the fast-time index). Thence, at any (i, g, p) triplet the $IQ_{i,g,p}[n]$ complex sequence is passed through a bank of phase rotators driven by NCOs, inducing (in parallel) in the fast-time a set of Doppler-frequency-offsets $f \in \{f_{min}, \dots, f_{max}\}$. Consequently, at any

(i, g, p, f) quadruplet the complex sequence at phase rotator output can be written as $Y_{i,g,p,f}[n] = IQ_{i,g,p}[n]e^{-j2\pi fTn}$ with T indicating the sampling time. Then, at any (i, g, p, f) quadruplet, the $Y_{i,g,p,f}[n]$ complex sequence is fed (in parallel) to N_T MFs (where the s th MF, $s = 1, \dots, N_T$, is matched to the complex envelope of the s th transmit waveform). Next, for every (i, p, f) triplet it is straightforward to group the Γ MF outputs as a function of n (for $n = 1, \dots, SWL$) into a complex matrix $\mathbf{\Omega}_{i,p,f} \in \mathbb{C}^{\Gamma \times SWL}$ which is eventually routed to the DBFN. The DBFN forms (in parallel) a set of ζ pencil beams within the Sub-VoI, i.e., $\{(\varphi_0, \theta_0)\}$ with $(\varphi_0, \theta_0) \in \{(\varphi_1, \theta_1), \dots, (\varphi_\zeta, \theta_\zeta)\}$. To this end, at each $(i, p, f, \varphi_0, \theta_0)$ quintuplet the MIMO DBFN output can be formulated as a complex sequence in the fast-time (i.e., $\mathbf{\Psi}_{i,p,f,\varphi_0,\theta_0} \in \mathbb{C}^{1 \times SWL}$) via the Hermitian product of the complex spatial steering vector with respect to φ_0, θ_0 , namely, $\mathbf{\zeta}_{\varphi_0,\theta_0} \in \mathbb{C}^{\Gamma \times 1}$ and $\mathbf{\Omega}_{i,p,f}$, i.e.,

$$\mathbf{\Psi}_{i,p,f,\varphi_0,\theta_0} = \mathbf{\zeta}_{\varphi_0,\theta_0}^H \mathbf{\Omega}_{i,p,f} \quad (4.13)$$

with $(\cdot)^H$ indicating the Hermitian matrix operator. Consequently, at every (f, φ_0, θ_0) triplet the input to the CFAR-like detection block is a real sequence in the fast-time $\mathbf{\Lambda}_{f,\varphi_0,\theta_0} \in \mathbb{R}^{1 \times SWL}$ which is obtained by passing $\mathbf{\Psi}_{i,p,f,\varphi_0,\theta_0}$ for $p = H, V$ through a modulus value operator elevated to the a power with $a = 1, 2$ ($|\cdot|^a$ in Fig. 4.9), a noncoherent combiner for the N_S PRIs within the dwell, and a noncoherent combiner for the H and V polarizations on receive (Σ in Fig. 4.9), i.e.,

$$\mathbf{\Lambda}_{f,\varphi_0,\theta_0} = \sum_{i=1}^{N_S} [|\mathbf{\Psi}_{i,H,f,\varphi_0,\theta_0}|^a + |\mathbf{\Psi}_{i,V,f,\varphi_0,\theta_0}|^a] \quad (4.14)$$

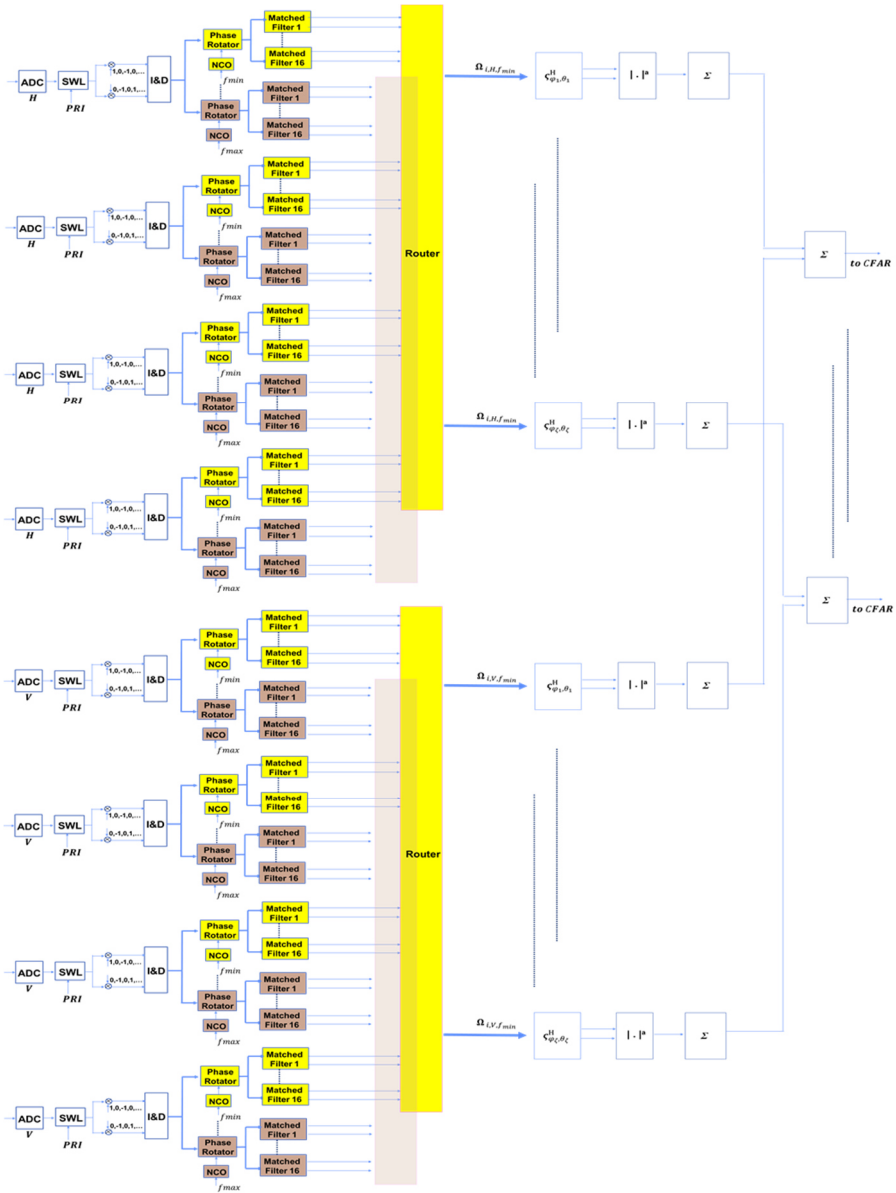


Fig. 4.9. MIMO SBR digital receiver lineup upstream CFAR-like detection block.

Notably, such an approach proves useful in a congested scenario for SSA (i.e., in case a CUT hosts more than one debris). Alternatively, assuming that a pencil beam generated within a Sub-VoI hosts at most one target in a CUT (an assumption held for example in chapter 2), only the branch of optimal Doppler offsets f_{opt} (i.e., the one which induces the maximum of the MF magnitude response) is fed as input to the CFAR-like detection block. Clearly, the digital subsystem of the MIMO SBR upstream the CFAR-like detection block presents a higher complexity with respect to that of the SIMO SBR in chapter 2. Moreover, the MIMO DBFN based on DSW may implement different kinds of beams within the Sub-VoI, including Σ , Δ_{el} , and Δ_{az} , for monopulse angular estimation as well as grd for SLB. For this reason, while bespoke high-speed signal processing tasks could be implemented on space-qualified FPGA (e.g., waveform generation and complex envelope extraction), the remaining workloads could be carried out on advanced many-core firmware (e.g., [65]).

4.3 Numerical Results

As a proof of concept for the signal processor sketched in Fig. 4.9, some numerical results follow hereafter. Accordingly, a reference operative scenario comprises an SBR orbiting at 7 km/s with an AESA in forward-looking configuration and 2 point-like targets moving at 7 km/s head-on towards the SBR. In this case, $v = 14$ km/s and both targets' DOA coincides with the AESA boresight. The 2 targets are 15 km far from one another (in particular, the leading target and the trailing target appear at 50 μ s and 150 μ s, respectively, from the SWL start time). Considering a dwell made of 4 PRIs, a simulation implements the

onboard processing lineup from the 8 ADC inputs to the CFAR-like detection block input (as per Fig. 4.9). The adopted point-like target echo model is that of eq. (4.12) along with AWGN with a 4 dB SNR for each addend in eq. (4.12) (i.e., $4 = 20 \log(D^p / \sigma\sqrt{2})$ with σ^2 accounting for noise power over the ADC sampling frequency). The simulation is aimed at highlighting the peak of the signal fed to the CFAR-like detection block as a function of the fast-time sample n within the SWL at boresight, i.e., $(u_{sub}, v_{sub}) = (0,0)$ and $(\varphi_0, \theta_0) = (0,0)$, when either a significant or negligible f_{res} affects the MFs input. At each PRI, each ADC is sampled at 20 MHz considering the superposition of 16 LFM pulses for each target, with each chirp spanning a 1 MHz bandwidth for a 127.5 μ s pulse duration with a Doppler frequency offset of -3.267 MHz pertaining to the echo range-rate. Moreover, each of the 16 LFM pulses is phase modulated by a dedicated Kasami code with binary symbols of period $P = 255$ with a 0.5 μ s chip time (this is an entire period of the selected Kasami codes from the small-set family [144]). For the sake of clarification, the selected Kasami codes have a number of features: the periodic auto and cross correlation properties of the codes are known by design and attain Welch's lower bound on the Peak to Side Lobe Ratio (PSLR) of the auto and cross correlation [144], the code synthesis is efficient via simple operations starting from an 8-bit Linear Feedback Shift Register (LFSR), and the number of available codes based on $P = 255$ is sufficient for the MIMO diversity conceived in this work. Fig. 4.10 shows as a reference the echo downstream one of the eight 16-bit ADCs (namely, that corresponding to $g = 1$ and $p = H$). In particular, Fig. 4.10 a) and b) represent the temporal and spectral echo behavior, respectively. As expected, the DS-SS appears shifted by the Doppler frequency offset from 1/4 of the sampling frequency (i.e., 5 MHz).

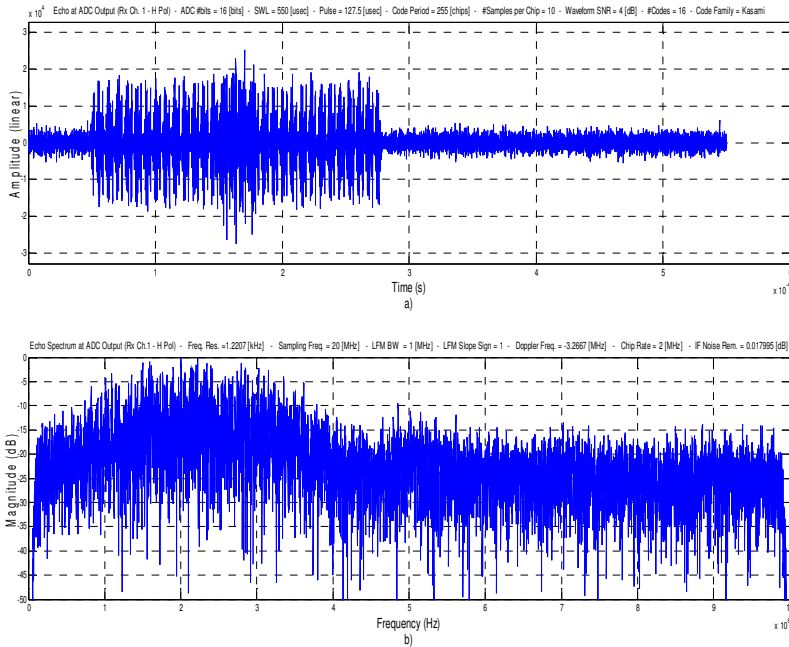


Fig. 4.10. Echo of targets 1 and 2 at ADC output ($g = 1$ and $p = H$) at a given PRI with $SWL = 550 \mu\text{s}$. a) temporal echo; b) spectral echo.

In general terms, considering a CDM-based MIMO SBR for SSA, it is desirable to employ transmit waveforms such that the MF magnitude response decreases monotonically and smoothly, and introduces a limited range bias with respect to the residual Doppler frequency of the input signals. Indeed, in this case the required amount of parallelization needed in the digital receiver to distribute a set of tentative Doppler-frequency-offsets can be reduced. In other words, adopting transmit waveforms with a high Doppler tolerance allows reducing the number of phase rotators and NCOs. For example, the well-known highly-Doppler-tolerant LFM waveform adopted in the SIMO SBR in chapter 2 spans the same bandwidth of the MIMO SBR proposed

in this chapter whereas its MFs can cope with an f_{res} of hundreds of kHz. On the other side, a pulsed waveform modulated in phase by an LFM with a Kasami code superimposed has a reduced Doppler tolerance. This is evident by the ambiguity function of such a waveform in Fig. 4.11. In this case, despite a slight inclined ridge does appear in the ambiguity function (due to the LFM component), a MF can cope with an f_{res} of approximately ± 6 kHz before the MF magnitude response decreases significantly. Consequently, a large set of tentative $\{f | f = f_{min}, \dots, f_{max}\}$ must be implemented in the receiver in case of pulsed waveforms modulated in phase by an LFM with a Kasami code superimposed.

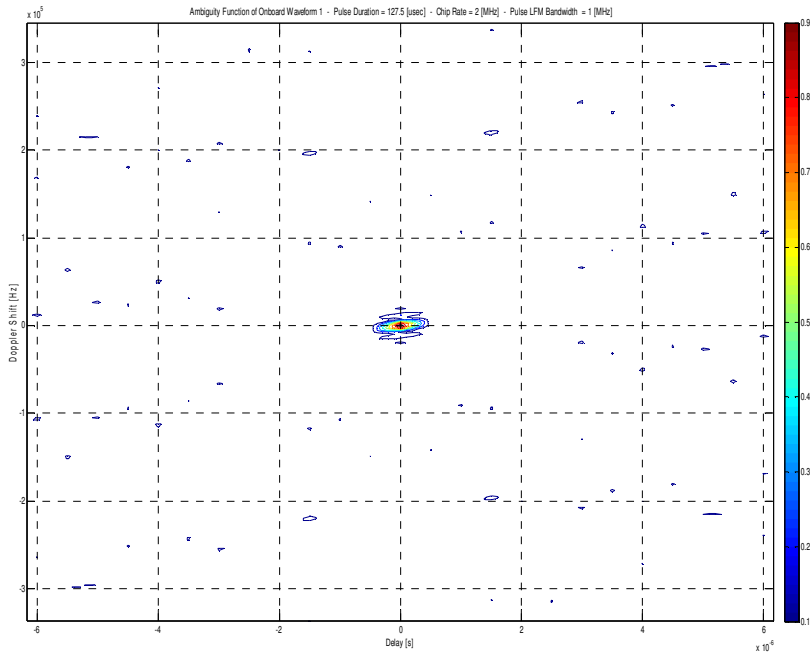


Fig. 4.11. Ambiguity function of transmit waveform (Kasami codes). $K_0 = 7.85 \times 10^9$ Hz/s, $T = 127.5 \mu\text{s}$, $T_c = 0.5 \mu\text{s}$, $P = 255$ chips.

For the sake of comparison at the same range resolution, replacing Kasami codes (for example) with Gold codes [144] of period $P = 127$ with a $0.5 \mu\text{s}$ chip time (while spanning the 1 MHz LFM bandwidth during $63.5 \mu\text{s}$) would not ameliorate the Doppler tolerance of the ambiguity function but rather introduce different interference features in terms of ambiguity function sidelobes (see Fig. 4.12).

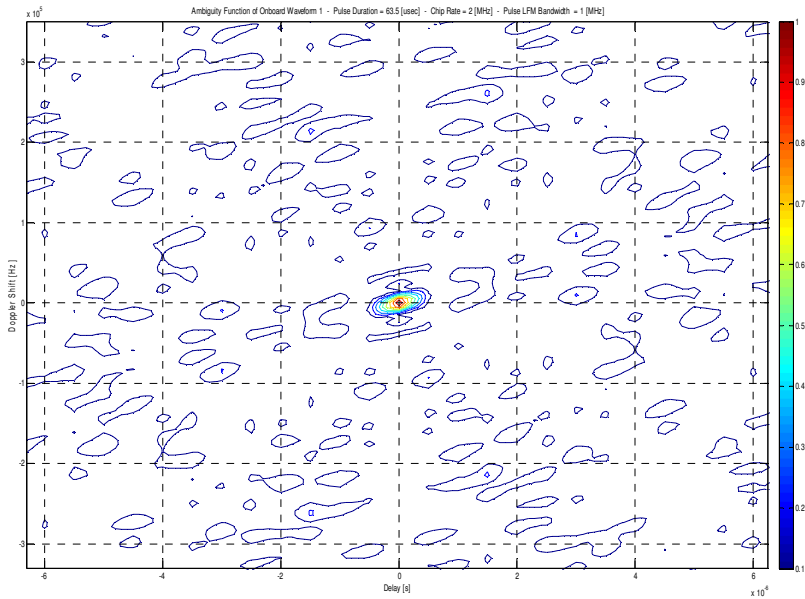


Fig. 4.12. Ambiguity function of transmit waveform (Gold codes). $K_0 = 1.575 \times 10^{10}$ Hz/s, $T = 63.5 \mu\text{s}$, $T_c = 0.5 \mu\text{s}$, $P = 127$ chips.

After applying the coherent MIMO DBFN cascaded with noncoherent combining in both the ξ_{slow} and ξ_{pol} dimensions, Figs. 4.13 and 4.14 report the peaks of targets 1 and 2 as a function of n at the input of the CFAR-like detection block for two cases. In particular, Fig. 4.13 accounts for a negligible residual-Doppler-frequency (namely, $f_{res} = 3$ kHz). In this case,

the 2 targets peaks are evident on the magnitude plot at 50 μ s and 150 μ s, respectively. On the contrary, Fig. 4.14 pertains to a significant residual-Doppler-frequency (i.e., $f_{res} = 23$ kHz) whereby no peak appears markedly evident for any target.

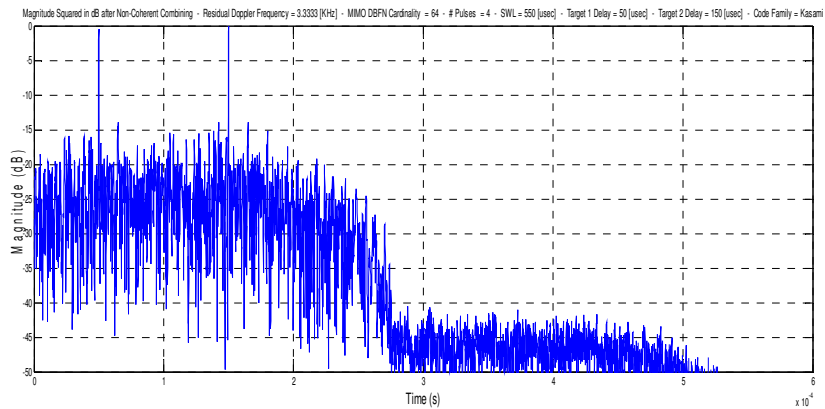


Fig. 4.13. Normalized magnitude of targets peaks evident at CFAR-like detection block input ($f_{res} = 3$ kHz).

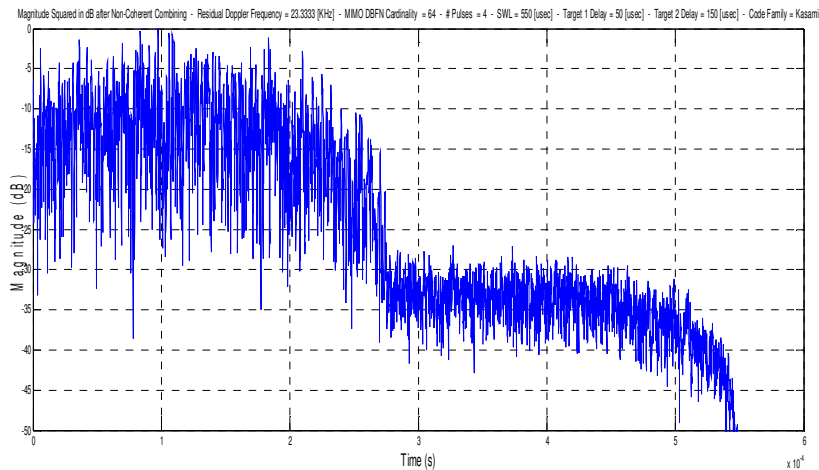


Fig. 4.14. Normalized magnitude of targets peaks not evident at CFAR-like detection block input ($f_{res} = 23$ kHz).

The benefit of using the LFM modulation within the pulsed waveform (in addition to the Kasami code superimposed) is addressed next. First of all, the LFM waveform can be activated at ease on transmit by simply programming a suitable slope (i.e., the K_0 parameter) in eq. (4.1). Consequently, an interleaved upchirp-downchirp LFM pulse train on consecutive PRIs during a dwell (as discussed in chapter 2) allows squelching even-time-around echoes, if any, in case of a negligible residual-Doppler-frequency. For instance, in Fig. 4.15 a degradation of the MF magnitude response occurs (i.e., no peak is markedly evident) when the onboard and echo waveforms have opposite LFM slope for $f_{res} = 3$ kHz.

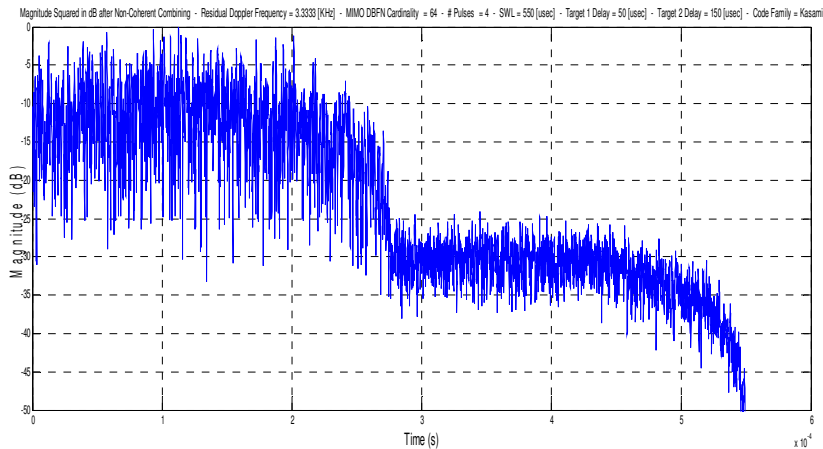


Fig. 4.15. Normalized magnitude of targets peaks not evident at CFAR-like detection block input ($f_{res} = 3$ kHz) for onboard and echo waveforms with opposite LFM slope.

Further echo acquisition variabilities and detection performance degradations due to endogenous (e.g., phase noise, numerical quantization, multichannel impairments) and exogenous (e.g., plasma scintillation, target scattering) impairments are outside the scope of this work.

Chapter 5

Conclusions Towards Cognitive-Based Bayesian Multi Target Tracking

Based on the SBR concept discussed so far for SSA, a critical reflection follows in this concluding chapter. In particular, a number of questions (and comments thereof) arise from a variety of perspectives. First and foremost, let us recall the leitmotiv question of this Ph.D work which has been stressed in chapter 1:

Q1) How can a SBR for SSA be designed to estimate at a given time epoch t_0 at least an initial condition $\{\mathbf{p}(t_0), \dot{\mathbf{p}}(t_0)\}$ of one (or more than one) debris crossing the SBR FoV?"

In order to cope with Q1), as hinted in chapters 2-4, such an SBR has been contrived to operate as a fully-polarimetric active instrument in the K_a -band with a focus on detection and tracking of small-size debris (thus complementing ground-based assets for SSA). To this end, it is paramount to stress that this SBR concept entails a scalable FoV (see Fig. 1.10) which depends on the performance of the enabling technology embarked on the SBR. Specifically, the FoV scalability pertains to the available transmit peak power (see Figs. 1.5) and thermal conditioning thereof, SIMO and MIMO multichannel diversity (see Figs. 2.2 and 4.1, respectively), and AESA steering capabilities (see Figs. 2.9-11). Beside *Q1*), which is clearly tailored to SSA, another possible use

of such an SBR relies on its exploitability for research on planetary ionospheres, atmospheres, surfaces, particles distribution of rings, and the like. That is, the following questions could be pondered:

Q2) Could the SBR transceiver, originally designed for SSA, be exploited to augment in-situ a-priori knowledge on interplanetary spacecraft housing dedicated instruments for RSE [22,160]?

Q3) Alternatively, could it be adopted as a novel radar-based instrument for RSE [22]? For example, could legacy Continuous Wave (CW) scattering investigations (historically based on distant interplanetary bistatic configurations [38][161]) be extended with novel pulse-based measurements for On-Board Radio Science (OBRAS) [162] from shorter backscattering distances?

Definitely, *Q2)* and *Q3)* introduce a potential liaison between SBRs and space-based radioscience and, therefore, are worth to be mentioned for the benefit of space agencies, e.g., [1,163], (albeit further digressions thereof are outside the scope of this work). On the other side, *Q4)* highlights the potential dual-use (i.e., civil-military) of a SBR envisaged for SSA:

Q4) Could an SBR for SSA be tailored to detect and track stealth, hyper-velocity HVTs?

That is, an hostile low-RCS HVT moving at hyper-velocity represent a threat to the HP and critical assets in space. In simple terms, *Q4)* is worth to be posed for the benefit of Space Domain Awareness (SDA) [164] in line with the Strategic Compass for Security and Defense [165] (clearly, a thorough discussion on *Q4)* is outside the scope of this work). Other questions to be discussed more openly in the conclusions of this thesis, are presented

hereafter. In particular, *Q5*) takes into account the SBR processor indicated in Figs. 2.2 and 4.1 for tracking purposes:

Q5) What "kind" of debris tracking data can be envisaged such that current SSA can be improved?

Interestingly, the answer to *Q5*) may hinge on the cross-disciplinary tracking wisdom summarized in [166] to support aerospace communities in their thriving efforts for debris cataloging. Next, *Q6*) identifies further research endeavors sprouting from this Ph.D. work:

Q6) Considering the Ph.D. work addressed in chapter 1-4, what lines of research appear as a promising way forward?

Indeed, by posing new questions in radar-theory, *Q6*) embodies a profound scientific value for SSA and frames the follow-on research activities of this Ph.D. work. Last but by no means least, *Q7*) represents a paramount question (in terms of safety) for future space-based navigation:

Q7) Could an SBR payload for SSA be embarked onboard future spacecraft in an early warning mode for autonomous collision avoidance maneuvering?

Remarkably, the answer to *Q7*) has been investigated by Robert Briskman [167], relying on observables provided by different onboard instruments, namely, optical and radar sensors.

Downstream this discernment, the rest of the chapter is organized as follows. Section 5.1 tackles *Q5*) paving the way for a cognitive-based SBR tailored to Bayesian MTT. Section 5.2 focuses on research avenues emerging from the findings of this Ph.D. work in line with *Q6*). Finally, Section 5.3 addresses *Q7*) making provision to harmonize the SBR payload with the onboard debris avoidance system concept proposed in [167].

5.1 Towards Cognitive-Based Bayesian MTT

Following the discussion on the SBR functional architecture for the SIMO and MIMO configurations, a digression on a cognitive-based Bayesian tracker is presented hereafter as the reference paradigm downstream the CFAR-like detection block. Within this framework, the SBR comprises a signal sensor, a data processor, as well as a controller (Fig. 5.1). Specifically, considering one (or more than one) debris appearing within the SBR FoV (see also Fig. 1.10), the primary task of the SBR sensor is to collect observables whereas the primary objective of the SBR processor is to estimate the state of each debris.

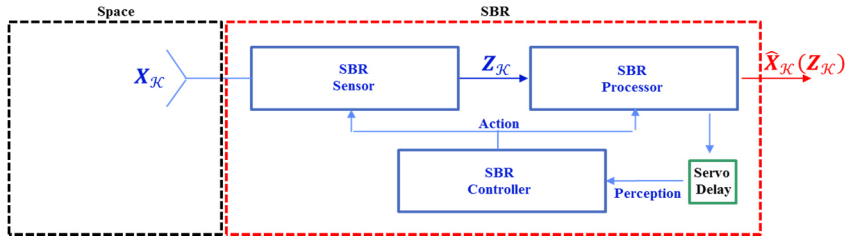


Fig. 5.1. SBR perception action cycle.

That is, let us first recall that the modeling keystone for debris tracking via a SBR is the approximation of debris motions along straight lines in 3-D at constant hyper-velocities with no maneuvering and considering “automatic tracking” [168] in limited time spans on the order of seconds (in which a debris might, or might not, cross the SBR FoR). To this end, a neat definition of a “track” and related “automatic tracking” proves useful as given by [168]: “A *track* represents the belief that a ...target is present and has actually been detected by the radar. An automatic tracking radar system forms a track when enough radar detections are made in a believable enough pattern to indicate a target is actually present...and when enough time has passed to

allow accurate calculation of the target's kinematic state... Thus, the goal of tracking is to transform a (time-lapse) detection picture into a track picture... The result of the automatic tracking process is a track file that contains a track state for each target detected by the radar." Armed with such "track" and "tracking" definitions, let us assume that reliable "debris-tracks-estimates" (i.e., the $\widehat{\mathbf{X}}_{\mathcal{K}}(\mathbf{Z}_{\mathcal{K}})$ tracklets in Fig. 5.1) are suitably inferred by a SBR via a posterior probability distribution on target state. In particular, $\mathbf{Z}_{\mathcal{K}} \triangleq \{\mathbf{z}_1, \dots, \mathbf{z}_{\mathcal{K}}\}$ is defined as a set of " \mathcal{K} -instants-SBR-measurements" and the state $\mathbf{X}_{\mathcal{K}} \triangleq \{\mathbf{x}_1, \dots, \mathbf{x}_{\mathcal{K}}\}$ is defined as a set of " \mathcal{K} -instants-debris-states" of one (or more than one) debris from the time instant t_1 to the time instant $t_{\mathcal{K}}$. Within such an elapse time, $\mathbf{x}_i = \{\mathbf{p}_{i,w}\}_{w=1}^{W_i}$ is the "ith-instant-debris-state-vector" (for $i = 1, \dots, \mathcal{K}$), which includes a number W_i of "debris-entity-state-vectors" (i.e., the cardinality of the debris-entity-state-vector set is possibly variable during the $[t_1, t_{\mathcal{K}}]$ elapse time), each identified by a 3-D cartesian position $\mathbf{p}_{i,w}$, and representing (in the most general sense) either an individual debris or a point of a debris cloud. Moreover, $\mathbf{z}_i = \{\mathbf{z}_{i,w}\}_{w=1}^{W_i'}$ is the "ith-instant-debris-measurement-vector" (for $i = 1, \dots, \mathcal{K}$), which includes a number W_i' of "debris-singleton-measurement-vectors" $\mathbf{z}_{i,w}$ (i.e., the cardinality of the debris-singleton-measurement-vector set is possibly variable during the $[t_1, t_{\mathcal{K}}]$ elapse time). Accordingly, \mathbf{z}_i can be processed by the Bayesian tracker (either as thresholded or unthresholded data [59]), as per the following structure of the debris-singleton-measurement-vector

$$\mathbf{z}_{i,w} = \left[\hat{\mathbf{r}}_{i,w}^T, \hat{\boldsymbol{\alpha}}_{el_{i,w}}^T, \hat{\boldsymbol{\alpha}}_{az_{i,w}}^T, [\text{vec}\{\mathbf{Z}_{MF_{i,w}}\}]^T \right]^T \quad (5.1)$$

where $\text{vec}\{\cdot\}$ is the matrix column stacking operator and the

remaining terms are clarified hereafter. Specifically, at the i th time instant for the w th debris-entity (i.e., at $i = 1, \dots, \mathcal{K}$, for $w = 1, \dots, W_i'$), $\hat{\mathbf{r}}_{i,w} \in \mathbb{R}^{2 \times 1}$ is the range estimation for the H and V polarizations, respectively, $\hat{\boldsymbol{\alpha}}_{el_{i,w}} \in \mathbb{R}^{2 \times 1}$ is the centroid elevation angle estimation for the H and V polarizations, respectively, $\hat{\boldsymbol{\alpha}}_{az_{i,w}} \in \mathbb{R}^{2 \times 1}$ is the centroid azimuth angle estimation for the H and V polarizations, respectively, and $\mathbf{Z}_{MF_{i,w}} \in \mathbb{C}^{\mathfrak{d}_i \times N_i}$ is a complex matrix whose entries represent the set of complex MF outputs (extracted during a dwell at a selected Doppler offset and range gate) for \mathfrak{d}_i channels¹⁰ and N_i pulses available at the i th measurement time. At the i th time instant for the w th debris-entity (at $i = 1, \dots, \mathcal{K}$, for $w = 1, \dots, W_i'$), $\mathbf{Z}_{MF_{i,w}}$ can provide the onboard tracker with further insights. For example, in the SIMO configuration the complex MF outputs of the Σ , Δ_{el} , and Δ_{az} channels embody additional attribute measurements [89,90] useful to the onboard tracker. These attributes are related to the possible unresolved detection of closely spaced targets within the CUT in terms of joint centroid-extent estimation (see [89, footnote of page 131] and [77, Fig. 11]). As hinted in chapter 1, considering limited time spans on the order of a second, it is possible to enforce a NCV model on $\hat{\mathbf{X}}_{\mathcal{K}}(\mathbf{Z}_{\mathcal{K}})$. Thus, from each tracklet cued by the position set $\{\mathbf{p}_{i,w}\}$ within $\hat{\mathbf{X}}_{\mathcal{K}}(\mathbf{Z}_{\mathcal{K}})$ whose w index occurs during a sufficient elapse time $[t_w \text{ initial}, t_w \text{ end}]$, i.e., pertaining to the time instants $i \in [t_w \text{ initial}, t_w \text{ end}] \subseteq [t_1, t_{\mathcal{K}}]$, it is possible to estimate $\{\mathbf{p}_w(t_0), \dot{\mathbf{p}}_w(t_0)\}$ at a given time instant $t_0 \in [t_w \text{ initial}, t_w \text{ end}]$ and, consequently, estimate a complete set of ephemerides at t_0 .

¹⁰ Considering the i th measurement time, for the SIMO SBR configuration $\mathfrak{d}_i = 6$ (due to the Σ , Δ_{el} , and Δ_{az} channels, each bearing the H and V polarizations); for the MIMO SBR configuration $\mathfrak{d}_i = 2\Gamma$ (accounting for Γ channels, each bearing the H and V polarizations).

Additional comments cue further insights on the envisaged SBR tracker. First of all, space objects maneuvering [169] can be neglected, thus abandoning the need for banks of parallel tracking filters or Interacting Multiple Models (IMM) [60]. As stressed in chapter 1, the debris motion relying on the linear CWNA model allows representing the NCV scenario for debris crossing the SBR FoR. Moreover, by properly constraining the CWNA model parameters it is possible to characterize mild changes in debris velocity components during an observation interval (see footnote 2 in § 1.5.3). Also, a Bayesian MTT functionality [59] can be contrived in case of a multitude of debris appearing within the instantaneous SBR FoV (see Fig. 1.10). In this case, it is possible to consider approaches relying either on Measurement to Track Associations (MTA) as tailored to multiple *individual debris* or on point process models as tailored to *debris clouds*.

Now, in the specific case of a SBR aimed at SSA via Bayesian inference, the objective of the SBR may coincide with estimating the tracklets $\hat{\mathbf{X}}_{\mathcal{K}}$ from a MTT perspective and according to a Bayesian formulation of the inference problem. Namely, allowing for the capability to exploit a-priori distributions for environmental debris density, target motion models, and interference; the capability to form a suitable likelihood-function based on the SBR sensor data acquisition; and finally the capability to combine the a-priori distributions and likelihood-functions into a suitable posterior distribution on target state [59]. Traditionally, the MTT-based state estimate could be accomplished by a, so called, feed-forward chain. According to the feed-forward paradigm, the SBR, after transmitting electromagnetic waveforms in the environment, acquires in its sensor possible scattered signals from debris present in the environmental scene, and then feeds the processor input with the sensor output information $\mathbf{Z}_{\mathcal{K}}$ in cascade (see Fig. 5.1). An

advanced, and more complex, approach would allow the processor decisions to be supported by an additional controller, which perceives feedbacks data from the processor itself and, by virtue of a constrained optimization framework, performs in closed loop a retroaction on both the sensor and processor future behavior in terms of transmit waveform and radiation pattern (see Fig. 5.1). The foregoing tracking concept based on message passing and feedback between the sensor and processor has been hinted in [89] with clear ties to modern radar lines of research [170-172] relying on the so called Perception-Action-Cycle (PAC). The PAC for target tracking is inspired by the cognitivity of the human brain as well as by sonar echolocating capabilities of several mammals. Both feedforward and feedback based paradigms can be implemented via the SBR functional architecture hinted in Figs. 2.2 and 4.1. Both configurations allow for Bayesian inference capabilities on small-size debris dynamic states and time series analysis on scattering signatures pertaining to the RCS. The system architecture needed to implement the archetype sketched in Fig. 5.1 makes provision for a cognitive capability of the SBR to interact within the geophysical environment. In particular, *cognitivity* is a feature of a modern radar transceiver (see [170-172]) characterized by:

- A PAC entailing a feedback between the receive and transmit sections.
- An onboard memory to store, update, and predict information.
- An attention manager allocating priorities amongst concurrent tasks and resources.

- An intelligence (interpreted as a decision capability relying on manifold layers of abstractions) taking into account observable states on receive, actions undertaken over the environment on transmit, as well as optimum policies for pondering costs.

To this end, the enabling-technology for implementing such functionalities on a SBR relies on miniaturization (in terms of system-on-chip and system-on-package policies) as well as on advanced performance keystones. Namely, large mass memories housing functional a-priori as part of an onboard KA design comprising endogenous (i.e., transceiver related) and exogenous (i.e., environmental related) databases; high speed interfaces, e.g., [173]; as well as distributed High-Performance-Extreme-Computing (HPEC) digital architectures, e.g., [65]. Such HPEC digital architectures are aimed either at job-level parallelism via multiple processors running independent activities, i.e., Multiple-Instructions-Multiple-Data (MIMD) or at parallel processing via multiple processors running simultaneously the same activity, i.e., Single-Instruction-Multiple-Data (SIMD).

5.2 Research Avenues

A number of research avenues may sprout from this Ph.D. work. Specifically, chapter 1 has provided an ontological framework for radars aimed at supporting SSA. After reasonable insights on space physics and debris fluxes, several assumptions have been outlined not only based on radar heritages but also on astrodynamics, space-based radio science, as well as general remote sensing experimental legacies. Remarkably, the result of this reasoning has pinpointed several comparisons between GBR and SBR measurements. A specific focus has been dedicated to clarify the benefit of adopting a novel SBR in the K_a -band as a *gedankenexperiment* to infer key debris features. Interestingly, in-situ measurements from an SBR would not be affected by possible neutral atmospheric nuisances whereas, using higher frequency bands such as the K_a -band, electromagnetic propagation would suffer from milder degradations. A transmit peak power on the order of kilowatts and an AESA represent key paradigms for such a novel SBR archetype. In this case, fully polarimetric capabilities and a wide and adaptively programmable receiver power dynamics represent key architectural designs. Moreover, employing signals with small bandwidths and spanning the sun only via the ARP sidelobes are valid operative configurations for framing suitable SNR regimes within signal processing schemes. Also, considering limited time spans on the orders of a second for debris detection and tracking in a small FoV (e.g., roughly a 100-km instantaneous-range from an orbiting SBR), it appears fruitful to model both debris and SBRs with an NCV motion. Such onboard processing schemes can be tailored not only to the general tasks of detection and MTT in the SBR FoR, but also to time series analysis on RCS signatures. As a by-product, this would endorse abandoning the intuitive and ambitious (yet intrinsically ambiguous) SEM. The

idea is to nurture current debris catalogs for SSA with a novel (less immediate but more realistic) unit of measure related to RCS signatures provided by the SBR onboard processing schemes.

Chapter 2 has outlined a novel SBR payload functional architecture for SSA as a bespoke fully-polarimetric monopulse-based pulsed radar in the K_a -band taking into account state-of-the-art space-qualified technologies in both digital and RF domains. Indeed, unlike a classical airborne pulse Doppler radar [63, 174] (which estimates an echo range-rate nominally via a discrete Fourier transform in the slow-time), the SBR deals with hyper-velocity targets and very few pulses in the slow-time (e.g., say 4 pulses) since additional pulses would inevitably induce range migration on the target detection scheme. In this case, a target is range non-ambiguous in the fast-time, and highly Doppler ambiguous in the slow-time. Accordingly, a bank of frequency offsets is applied directly in the fast-time to a group of MFs in parallel. This is equivalent to a filter bank in the fast-time with a group of Doppler frequency offsets not for estimating a target radial velocity (due to the inherent ambiguity of the echo range-rate in cueing the debris range-rate) but rather as a means to enforce Doppler tolerance on the PC scheme and avoid straddle losses. To this end, the envisaged monopulse-based functional architecture in Fig. 2.2 is aimed at acquiring a complex data hyper-cube while searching for targets based on the L-PRF RRRS scheme. The adaptivity of such an architecture allows including robust and selective debris detection schemes tailored to CFAR-like paradigms. Moreover, specific parameter estimates from a burst of pulse echoes make provision for further Bayesian inference capabilities on small-size debris dynamic states as well as RCS-related signatures via time series analysis. Now, the acquisition of echoes related to the motion of a debris for an elapse time up to several hundreds of milliseconds could be operatively extended to a few seconds, thus augmenting the time on target with additional measurement and gauging perspectives.

By selecting an optimal transceiver configuration such that the SBR AESA transmit beam points the debris target minimizing a cost function (for example, as per a joint waveform and beam control optimization with ties to [175]), it would be possible to refine radiometric signatures insights.

Chapter 3 has discussed the performance analysis of conventional radar detectors in AWGN for a monostatic configuration accounting for either Rayleigh or Rice fluctuating targets, and considering plasma media with weak scintillation. Additional hints have also been outlined to extend the analysis to bistatic configurations. Finally, numerical results have cued a paramount framework to characterize the influence of plasma media in weak scintillation on SBR performance as a function of the scintillation index s_4 . Remarkably, the analysis of the FOP for a SBR in a monostatic configuration has demonstrated that a SBR for SSA aimed at processing a burst of echoes for detection and tracking schemes is prone to fading losses caused by plasma effects as a function of the scintillation index s_4 . Also, the FOP curves provide a conceptual framework (which is novel from a radar perspective) to empirically estimate the scintillation index s_4 by fitting (e.g., via least squares) a sufficient number of available echo returns from reference targets in a monostatic radar configuration. As already stressed in [99,100,102], the detection performance of a SBR can be seriously degraded if the effects of turbulence in plasma media are not taken into account. The analysis in this work is novel since it highlights from a theoretical perspective such a degradation as a function of a measurable parameter, namely, the scintillation index s_4 . In other words, this work demonstrate that debris inferences from a SBR aimed at supporting SSA can be affected not only by target fluctuations but also by channel scintillations. As a useful reference, it is worth comparing the required single pulse SNR in order to obtain a $P_D = 0.9$ at $P_{FA} = 10^{-5}$ for $K = 4$ with and without plasma scintillation. More specifically, Table 5.1

summarizes the required single pulse SNR for SW0-C, SW1-C, SW0-NC, and SW1-NC cases in the aforementioned reference example based on Figs. 3.5, 3.6, 3.8, and 3.10.

	$s_4 = 0$	$s_4 = 0.1$	$s_4 = 0.4$
SW0-C	6.5 dB	6.7 dB	10.5 dB
SW0-NC	7.5 dB	7.8 dB	12 dB
SW1-C	14 dB	14.1 dB	17 dB
SW1-NC	15.5 dB	15.6 dB	18 dB

Table 5.1. Required single pulse SNR in order to obtain a $P_D = 0.9$ at $P_{FA} = 10^{-5}$ for $K = 4$ at different values of s_4 .

Accordingly, a negligible increase of the required single pulse SNR appears for very mild plasma scintillation (i.e., $s_4 = 0.1$) whereas a much larger single pulse SNR emerges for weak scintillation (i.e., $s_4 = 0.4$). Interestingly, without plasma scintillation (i.e., $s_4 = 0$) the SW0 and SW1 target models require the minimum (i.e., 6.5 dB for the coherent pulse train case and 7.5 dB for the noncoherent pulse train case) and maximum (i.e., 14 dB for the coherent pulse train case and 15.5 dB for the noncoherent pulse train case) single pulse SNR, respectively. However, when weak plasma scintillation occurs (e.g., $s_4 = 0.4$) to maintain the same performance the SW0 target model requires a larger augmentation of single pulse SNR (i.e., roughly 4 dB more for the coherent pulse train case and 4.5 dB more for the noncoherent pulse train case) compared to that of the SW1 target model (i.e., roughly 3 dB more for the coherent pulse train case and 2.5 dB more for the noncoherent pulse train case). Also, the chapter capitalizes on analytic solutions to structured integrals expressed as the Laplace transform of the product of Marcum Q and power functions for eq. (3.26) and the Laplace transform of the product of Marcum Q, Bessel I, and power functions for eqs. (3.30-3.33). The closed form analytical expression computed in

this work for the performance analysis of conventional radar detectors in case of Rayleigh targets (namely, eqs. (3.27-3.29) based on eq. (3.26) are well known in literature [112]. On the other side, the closed form analytical expressions computed for the performance analysis of conventional radar detectors in case of Rice targets namely, eqs. (3.35, 3.36, and 3.38) are novel and rely on the support of eqs. (3.30-3.33) which appear in [120]. The value of such theoretical findings is significant. Previously, the use of a Rician distribution for fluctuating targets did not allow for closed form analytical expressions for the performance analysis of conventional radar detectors and, for this reason, Swerling III/IV target fluctuating models were adopted as an approximation for Rician target fluctuating models [114, 115]. A few additional comments follow in order to stimulate further lines of research. First of all, considering gyrotropics effects in magnetized plasma media [23], the original polarization of a general propagating Transverse Electromagnetic Mode (TEM) is affected by Faraday rotation angles (see for instance [176]). This drives the mandatory design of state of the art radar systems for SSA encompassing polarimetric architectures [9] and, therefore, related detection and tracking performance analyses thereof. A second comment provides insights on the limit of applicability of the Rice distribution when weak scintillation is no longer a valid assumption. Apparently, for a turbulent plasma (e.g., $s_4 \rightarrow 1$), one might be tempted to assume the Rice distribution to become a Rayleigh distribution [99,100]. However, for $s_4 \rightarrow 1$ the weak scattering assumption on propagation is unlikely to hold (i.e., the Rytov solution [24, eqs. (3.24) and (3.25)] is no longer reasonable). Interestingly, for a turbulent plasma several hints in [24] cue to the occurrence of a compound process pertaining to the co-existence of slow refractive effects (derived from large plasma irregularities) superimposed on fast diffractive effects (derived from small plasma irregularities). In this case, a more structured composite fading distribution may deem appropriate

[177-179] whereas further performance analysis might benefit from analytic expressions derived from applications in communication theory [180]. Eventually, it is also reasonable to ponder if the slowly decorrelating component of such a compound process can be assumed as a random constant during the timescales of the coherence-time of the channel or (if smaller) during a radar burst, thus modeling the scintillation process as a Spherically Invariant Random Process (SIRP) [181-183]. Third, the scintillation index s_4 has been adopted as a measurable parameter to estimate the state of the channel in weak plasma scintillation (as stressed in chapter 1 based on [22] and [24]). Yet, it is worth reminding that s_4 is a function of the intensity of the electric field measured at a specific wavelength in a given location and temporal window. In particular, the computation of s_4 does not rely on a thorough knowledge of the medium via a joint temporal-spatial spectrum. To this end, in this work a condition of stationarity and isotropy of the medium was inherently assumed during the measurement of s_4 . In addition, a flat-flat channel and a planar wavefront impinging on the antenna surface was also assumed during a short radar burst on a small bandwidth within the K_a -band. Future works could analyze the effects of the spectral structure of the medium (as per [24] and [184]) on SBR performance. For instance, a specific line of research could investigate the fluctuations of the G_a term in eq. (3.3) via mutual intensity functions (see [185, eq. (8)]) applied to the spatial extent of the antenna surface. A fourth comment stresses the exploitability of the scintillation index s_4 as a useful proxy-parameter (as clarified in chapter 1) to be measured either by bespoke probes directly in-situ (e.g., [186]) or indirectly from data (see [187]) to sustain a KA design of a modern radar architecture for SSA. In particular, in case of significant plasma turbulence, radar systems for SSA might have to temporarily interrupt detection and tracking operations or, at least, optimize the radar mode or transceiver configuration. Last but by no means

least, future works could extend the performance analysis of conventional radar detectors in plasma media with weak scintillation in case of bistatic configurations.

Finally, chapter 4 has outlined the archetype of a novel SBR in the K_a -band for SSA as a CDM-based MIMO payload transceiver. The functional architecture of the fully-polarimetric pulsed radar has been described including key comparisons with chapter 2 based on SIMO diversities. SBR operations have been clarified via timing hierarchies in surveillance mode, the complex data hyper-cube structure, and a L-PRF RRRS entailing a TWSS contacts collection strategy. Ancillary details on the SBR functional architecture have addressed paramount insights to ponder critical MIMO aspects. Finally, numerical results have provided a proof of concept for the signal processor upstream the CFAR-like detection block relying on waveform-based, spatial, temporal, and polarimetric echo diversities. Downstream this summary, the MIMO SBR paradigm has been conceived at the cost of an augmented onboard complexity with respect to the SIMO counterpart in chapter 2. This includes tasks implemented on space-qualified FPGAs and advanced many-core firmware (e.g., [65]) along with mandatory calibration procedures to deal with multichannel nonidealities [131]. Definitely, the flexibility of a SBR payload switching between SIMO and MIMO configurations represents a paramount operative capability to possibly swap TWSS and PWS strategies. To this end, while the digital section requires an increased level of parallelization of atomic processing schemes [188], the design and development of the AESA subsystem represents a major challenge from an electrical and mechanical engineering perspective (including the burden for the microwave bulk of the subarrays power combiners and dividers). Further lines of research are briefly summarized hereafter. First of all, an interesting line of research addresses the analysis of an optimum assembly of domino-tiles (i.e., a domino-tiled-array-synthesis-problem) on a subarray-based AESA with

the additional constraint of irregularity of the ELA pertaining to different AESA cuts (see [150, §1.3.3]). A second valuable research avenue is based on analyzing detection and angular estimation techniques [189], including SLB [190, 191] with a MIMO SBR. Third, in the MIMO SBR configuration the amplitude and phase terms in eq. (4.12) (i.e., D^p and φ_0^p , respectively) are modeled as constant with respect to an (s, g) pair. This represents an approximation which may not hold in case of plasma scintillation. An interesting line of research can be tailored to investigate the effects of plasma media with weak scintillation on the detection performance of a MIMO SBR as a function of the scintillation index s_4 as well as the spectral structure of the medium. Finally, it appears mandatory to devote further research efforts on novel CDM-based waveforms with improved Doppler tolerance.

5.3 Onboard-based debris avoidance system

Autonomous collision avoidance operations have been contrived by Robert Briskman in [167] (see the green blocks in Fig. A.1) in order to bypass ground-based collision avoidance operations (see [15] as an example). More specifically, let us assume that an SBR can collect the observable $\mathbf{Z}_{\mathcal{K}}$ and be able to provide reliable debris tracks estimates $\hat{\mathbf{X}}_{\mathcal{K}}$ (i.e. the 101 block in [167]). Based on $\hat{\mathbf{X}}_{\mathcal{K}}$ (see the upper red arrow in Fig. A.1), future spacecraft computing capabilities are envisaged to carry out a cascade of operations, namely, debris orbit determination (i.e. the 102 block in [167]), debris ephemerides generation (i.e. the 103 block in [167]) (jointly with spacecraft ephemerides generation aided by ancillary onboard sensors and available data from the ground), followed by a debris-spacecraft collision calculation (i.e. the 104 block in [167]), a decision branch for act store or reset (i.e. the 105, 106, 107 blocks respectively in [167]), a spacecraft

avoidance orbit processing (i.e. the 108 block in [167]), and finally, if need be, commands (i.e. the 109 block in [167]) for autonomous spacecraft thrusters firings and attitude control (i.e. the 110 block in [167]).

Interestingly, the operative concept proposed in [167] is based on a wise policy of interoperability (and therefore backward compatibility) with legacy ground-based systems which can provide the spacecraft with both debris and spacecraft orbital ephemerides (i.e., see the ancillary lower input in Fig. A.1 feeding the 103 block).

Nevertheless, it is worth stressing that the aforementioned set of cascaded operations for autonomous collision avoidance represent the set of operations currently devised on ground [15] (exploiting all available ground-based and in-situ measurements) in order to maneuver a spacecraft. Within this framework, a SBR for SSA can provide ground stations with its tracklets, thus enlarging the set of available in-situ assets to support ground-based operations for SSA (see the lower red arrow in Fig. A.1).

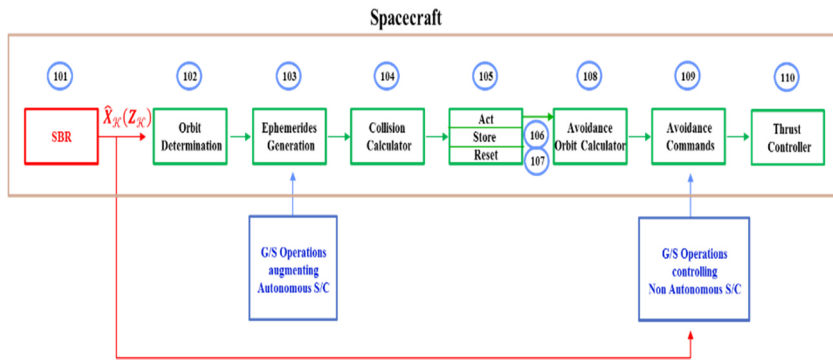


Fig. A.1: Onboard-based Debris Avoidance System Concept (green blocks from [167]).

Appendix A

Analytic Solutions to Structured Integrals Expressed as the Laplace Transform of the Product of Marcum Q and Power Functions

In chapter 3, eq. (3.26) was exploited to formulate the performance analysis of conventional radar detectors in case of Rayleigh targets. Eq. (3.26) is a structured integral expressed as the Laplace transform of the product of Marcum Q and power functions. For convenience, its closed form solutions are reported in this appendix as eq. (A.1), i.e.,

$$\int_0^{\infty} Q_{\mathbb{H}}(\sqrt{2bx}, \sqrt{2T}) \frac{1}{\beta^{\alpha}} \frac{x^{\alpha-1}}{\Gamma(\alpha)} e^{-\frac{x}{\beta}} dx$$

$$= \begin{cases} \sum_{n=0}^{\infty} \frac{(\alpha)_n (b\beta)^n}{(b\beta + 1)^{\alpha+n} \Gamma(\mathbb{H} + n) n!} \Gamma_{inc}(\mathbb{H} + n, T), & \alpha > 0 \\ \sum_{n=0}^{\alpha - \mathbb{H}} \binom{\alpha - \mathbb{H}}{n} \frac{(b\beta)^n}{(b\beta + 1)^{\alpha - \mathbb{H}} \Gamma(\mathbb{H} + n)} \Gamma_{inc}\left(\mathbb{H} + n, \frac{T}{b\beta + 1}\right), & \alpha \geq \mathbb{H} \geq 1, \alpha \in \mathbb{N} \end{cases} \quad (\text{A.1})$$

and its derivation proceeds as follows. Considering the generalized Marcum function of order \mathbb{H} [117] in eq. (A.1), and recalling that $I_n(b)$ is the modified Bessel function of the first

kind and n -th order, let us elaborate for $\alpha > 0$ the left-hand side of eq. (A.1) as

$$\begin{aligned}
& \int_0^\infty Q_{\mathbb{H}}(\sqrt{2bx}, \sqrt{2T}) \frac{1}{\beta^\alpha \Gamma(\alpha)} x^{\alpha-1} e^{-\frac{x}{\beta}} dx \\
&= \int_0^\infty \int_{\sqrt{2T}}^\infty \frac{y^{\mathbb{H}}}{(\sqrt{2bx})^{\mathbb{H}-1}} e^{-\frac{y^2+2bx}{2}} I_{\mathbb{H}-1}(y\sqrt{2bx}) dy \frac{x^{\alpha-1}}{\beta^\alpha \Gamma(\alpha)} e^{-\frac{x}{\beta}} dx \\
&= \frac{1}{\beta^\alpha \Gamma(\alpha) (\sqrt{2b})^{\mathbb{H}-1}} \int_{\sqrt{2T}}^\infty \int_0^\infty x^{\frac{2\alpha-\mathbb{H}-1}{2}} e^{-\left(\frac{b\beta+1}{\beta}\right)x} I_{\mathbb{H}-1}(y\sqrt{2bx}) dx y^{\mathbb{H}} e^{-\frac{y^2}{2}} dy \quad (\text{A.2})
\end{aligned}$$

Introducing the variable $z = \sqrt{x}$, and expressing

$$I_n(x) = e^{-j\frac{\pi}{2}n} J_n\left(x e^{j\frac{\pi}{2}}\right) \quad (\text{A.3})$$

where $J_n(x)$ is the Bessel function of the first kind and n -th order [118, eq. (8.406-1)], eq. (A.2) can be formulated as

$$\begin{aligned}
& \frac{1}{\beta^\alpha \Gamma(\alpha) (\sqrt{2b})^{\mathbb{H}-1}} \int_{\sqrt{2T}}^\infty \int_0^\infty x^{\frac{2\alpha-\mathbb{H}-1}{2}} e^{-\left(\frac{b\beta+1}{\beta}\right)x} I_{\mathbb{H}-1}(y\sqrt{2bx}) dx y^{\mathbb{H}} e^{-\frac{y^2}{2}} dy \\
&= \frac{2 e^{-j\frac{\pi}{2}(\mathbb{H}-1)}}{\beta^\alpha \Gamma(\alpha) (\sqrt{2b})^{\mathbb{H}-1}} \int_{\sqrt{2T}}^\infty \int_0^\infty z^{2\alpha-\mathbb{H}} e^{-cz^2} J_{\mathbb{H}-1}(gz) dz y^{\mathbb{H}} e^{-\frac{y^2}{2}} dy \quad (\text{A.4})
\end{aligned}$$

where $u = 2\alpha - \mathbb{H}$, $g = y\sqrt{2b} e^{j\frac{\pi}{2}}$, and $c = (b\beta + 1)/\beta$. Using [118, eq. (6.631-1)] on the inner integral of the right-hand side of eq. (A.4), one may further develop eq. (A.4) as

$$\begin{aligned}
& \frac{2 e^{-j\frac{\pi}{2}(\mathbb{H}-1)}}{\beta^\alpha \Gamma(\alpha) (\sqrt{2b})^{\mathbb{H}-1}} \int_{\sqrt{2T}}^{\infty} \int_0^{\infty} z^{\mathbb{H}} e^{-cz^2} J_{\mathbb{H}-1}(\varrho z) dz y^{\mathbb{H}} e^{-\frac{y^2}{2}} dy \\
&= \frac{2 e^{-j\frac{\pi}{2}(\mathbb{H}-1)}}{\beta^\alpha \Gamma(\alpha) (\sqrt{2b})^{\mathbb{H}-1}} \int_{\sqrt{2T}}^{\infty} y^{\mathbb{H}} e^{-\frac{y^2}{2}} \frac{\varrho^{(\mathbb{H}-1)} \Gamma\left(\frac{\mathbb{H}+\mathbb{H}}{2}\right)}{2^{\mathbb{H}} c^{\frac{(\mathbb{H}+\mathbb{H})}{2}} \Gamma(\mathbb{H})} {}_1F_1\left[\frac{\mathbb{H}+\mathbb{H}}{2}; \mathbb{H}; -\frac{\varrho^2}{4c}\right] dy \\
&= \frac{1}{2^{\mathbb{H}-1} (b\beta + 1)^\alpha \Gamma(\mathbb{H})} \int_{\sqrt{2T}}^{\infty} y^{2\mathbb{H}-1} e^{-\frac{y^2}{2}} {}_1F_1\left[\alpha; \mathbb{H}; \frac{1}{2\left(\frac{b\beta + 1}{b\beta}\right)} y^2\right] dy
\end{aligned} \tag{A.5}$$

where ${}_1F_1[\alpha; \gamma; z]$ is the confluent hypergeometric function [118, eq. (9.210-1)] holding in general for $\Re((b\beta + 1)/\beta) > 0$ and $\Re(2\alpha - 1) > -1$ (with $\Re(\cdot)$ indicating the real part of a complex number [121]) which is satisfied in eq. (A.5). Consequently, eq. (A.5) can be further elaborated introducing the variable $\mathfrak{s} = y/\sqrt{2T}$, thus resulting in

$$\begin{aligned}
& \frac{1}{2^{\mathbb{H}-1} (b\beta + 1)^\alpha \Gamma(\mathbb{H})} \int_{\sqrt{2T}}^{\infty} y^{2\mathbb{H}-1} e^{-\frac{y^2}{2}} {}_1F_1\left[\alpha; \mathbb{H}; \frac{1}{2\left(\frac{b\beta + 1}{b\beta}\right)} y^2\right] dy \\
&= \frac{2 T^{\mathbb{H}}}{(b\beta + 1)^\alpha \Gamma(\mathbb{H})} \int_1^{\infty} \mathfrak{s}^{2\mathbb{H}-1} e^{-T \mathfrak{s}^2} {}_1F_1\left[\alpha; \mathbb{H}; \frac{b\beta T}{b\beta + 1} \mathfrak{s}^2\right] d\mathfrak{s} \\
&= \frac{2 T^{\mathbb{H}}}{(b\beta + 1)^\alpha \Gamma(\mathbb{H})} \int_1^{\infty} \mathfrak{s}^{2\mathbb{H}-1} e^{-T \mathfrak{s}^2} \sum_{k=0}^{\infty} \left(\frac{b\beta T}{b\beta + 1}\right)^k \mathfrak{s}^{2k} \frac{(\alpha)_k}{(\mathbb{H})_k k!} d\mathfrak{s}
\end{aligned} \tag{A.6}$$

where the last equality derives from using the Pochhammer symbol defined in eq. (3.24) in the expression [118, eq. (9.210-1)]. Now, let us have a brief detour and recall that the upper incomplete Gamma function $\Gamma_{inc}(\zeta, x)$ represented in eq. (3.23) is generally valid for $\Re(\zeta) > 0$ (see [118, eq. (8.350-2)]) but can also be represented as [118, eq. (8.352-4)], i.e.,

$$\Gamma_{inc}(\zeta, x) = \Gamma(\zeta) e^{-x} \sum_{m=0}^{\zeta-1} \frac{x^m}{m!} \quad (\text{A.7})$$

when $\zeta \in \mathbb{N} \setminus \{0\}$. Consequently, moving the discrete sum outside the integral in eq. (A.6) it is straightforward to show that eq. (A.6) can be further reduced to

$$\begin{aligned} & \frac{2 T^{\mathbb{H}}}{(b\beta + 1)^\alpha \Gamma(\mathbb{H})} \int_1^\infty \mathbb{S}^{2\mathbb{H}-1} e^{-T \mathbb{S}^2} \sum_{k=0}^\infty \left(\frac{b\beta T}{b\beta + 1} \right)^k \mathbb{S}^{2k} \frac{(\alpha)_k}{(\mathbb{H})_k k!} d\mathbb{S} \\ & = \sum_{k=0}^\infty \frac{b\beta^k (\alpha)_k 2T^{k+\mathbb{H}}}{(b\beta + 1)^{\alpha+k} \Gamma(\mathbb{H}+k) k!} \int_1^\infty \mathbb{S}^{2k+2\mathbb{H}-1} e^{-T \mathbb{S}^2} d\mathbb{S} \quad (\text{A.8}) \end{aligned}$$

To this end, the integral on the right-hand side of eq. (A.8) has a closed form solution, i.e.,

$$\int_1^\infty \mathbb{S}^{2k+2\mathbb{H}-1} e^{-T \mathbb{S}^2} d\mathbb{S} = \frac{\Gamma_{inc}(k+\mathbb{H}, T)}{2T^{k+\mathbb{H}}} \quad (\text{A.9})$$

as per [118, eq. (3.381-9)]. Consequently, as per the upper term on the right-hand side of eq. (A.1)

$$\sum_{k=0}^\infty \frac{b\beta^k (\alpha)_k 2T^{k+\mathbb{H}}}{(b\beta + 1)^{\alpha+k} \Gamma(\mathbb{H} + k) k!} \int_1^\infty \mathbb{S}^{2k+2\mathbb{H}-1} e^{-T \mathbb{S}^2} d\mathbb{S}$$

$$= \sum_{k=0}^{\infty} \frac{b\beta^k (\alpha)_k}{(b\beta+1)^{\alpha+k} \Gamma(\mathbb{H}+k) k!} \Gamma_{inc}(k + \mathbb{H}, T) \quad (\text{A.10})$$

This completes the demonstration of eq. (A.1) for $\alpha > 0$, i.e., for the upper term on the right-hand side of eq. (A.1). The lower term on the right-hand side of eq. (A.1) can be demonstrated (for $\alpha \geq \mathbb{H} \geq 1, \alpha \in \mathbb{N}$) as follows. To begin with, it is worth noting [192, page 81] that

$$\begin{aligned} & {}_1F_1 \left[\mathcal{N} + \mathcal{L}; \mathcal{N} + m + 1; \frac{\mathcal{C} \mathfrak{a}}{1 + \mathcal{C}} \right] \\ &= e^{\frac{\mathcal{C} \mathfrak{a}}{1 + \mathcal{C}}} \sum_{l=0}^{\mathcal{L}-1-m} \frac{1}{l!} \frac{(\mathcal{L} - 1 - m)! (\mathcal{N} + m)!}{(\mathcal{L} - 1 - m - l)! (\mathcal{N} + m + l)!} \left(\frac{\mathcal{C} \mathfrak{a}}{1 + \mathcal{C}} \right)^l \end{aligned} \quad (\text{A.11})$$

Thus, for $\mathcal{N} + \mathcal{L} = \alpha$, $\mathcal{N} + m + 1 = \mathbb{H}$, $\mathcal{C} = b\beta$, and $\mathfrak{a} = T\mathbb{S}^2$, the mid term of eq. (A.6) can be rewritten as

$$\begin{aligned} & \frac{2 T^{\mathbb{H}}}{(b\beta + 1)^{\alpha} \Gamma(\mathbb{H})} \int_1^{\infty} \mathbb{S}^{2\mathbb{H}-1} e^{-T \mathbb{S}^2} {}_1F_1 \left[\alpha; \mathbb{H}; \frac{b\beta T}{b\beta + 1} \mathbb{S}^2 \right] d\mathbb{S} \\ &= \frac{2 T^{\mathbb{H}}}{(b\beta + 1)^{\alpha} \Gamma(\mathbb{H})} \int_1^{\infty} \mathbb{S}^{2\mathbb{H}-1} e^{-T \mathbb{S}^2} e^{\frac{b\beta T}{b\beta + 1} \mathbb{S}^2} \\ & \quad \times \sum_{l=0}^{\alpha-\mathbb{H}} \frac{(\alpha-\mathbb{H})!}{l!(\alpha-\mathbb{H}-l)!} \frac{(\mathbb{H}-1)!}{(\mathbb{H}-1+l)!} \left(\frac{b\beta T}{b\beta + 1} \mathbb{S}^2 \right)^l d\mathbb{S} \end{aligned} \quad (\text{A.12})$$

Again, moving the discrete sum outside the integral in eq. (A.12) results in

$$\begin{aligned}
& \frac{2 T^{\mathbb{H}}}{(b\beta + 1)^{\alpha} \Gamma(\mathbb{H})} \int_1^{\infty} \mathbb{S}^{2\mathbb{H}-1} e^{-T \mathbb{S}^2} e^{\frac{b\beta T}{b\beta+1} \mathbb{S}^2} \\
& \times \sum_{l=0}^{\alpha-\mathbb{H}} \frac{(\alpha - \mathbb{H})!}{l! (\alpha - \mathbb{H} - l)!} \frac{(\mathbb{H} - 1)!}{(\mathbb{H} - 1 + l)!} \left(\frac{b\beta T}{b\beta + 1} \mathbb{S}^2 \right)^l d\mathbb{S} \\
& = \sum_{l=0}^{\alpha-\mathbb{H}} \binom{\alpha - \mathbb{H}}{l} \frac{(b\beta T)^l}{(1 + b\beta)^{\alpha+l}} \frac{2T^{\mathbb{H}}}{\Gamma(\mathbb{H})} \frac{(\mathbb{H} - 1)!}{(\mathbb{H} - 1 + l)!} \\
& \quad \times \int_1^{\infty} \mathbb{S}^{2\mathbb{H}+2l-1} e^{\left(\frac{b\beta T}{b\beta+1} - T\right) \mathbb{S}^2} d\mathbb{S} \tag{A.13}
\end{aligned}$$

Then, using [118, eq. (3.381-9)] the integral in eq. (A.13) has a closed form solution, i.e.,

$$\int_1^{\infty} \mathbb{S}^{2\mathbb{H}+2l-1} e^{\left(\frac{b\beta T}{b\beta+1} - T\right) \mathbb{S}^2} d\mathbb{S} = \frac{\Gamma_{inc}\left(\mathbb{H}+l, \frac{T}{b\beta+1}\right)}{2\left(\frac{T}{b\beta+1}\right)^{\mathbb{H}+l}} \tag{A.14}$$

and, therefore, eq. (A.13) simplifies to

$$\begin{aligned}
& \sum_{l=0}^{\alpha-\mathbb{H}} \binom{\alpha - \mathbb{H}}{l} \frac{(b\beta T)^l}{(1 + b\beta)^{\alpha+l}} \frac{2T^{\mathbb{H}}}{\Gamma(\mathbb{H})} \frac{(\mathbb{H} - 1)!}{(\mathbb{H} - 1 + l)!} \\
& \quad \times \int_1^{\infty} \mathbb{S}^{2\mathbb{H}+2l-1} e^{\left(\frac{b\beta T}{b\beta+1} - T\right) \mathbb{S}^2} d\mathbb{S} \\
& = \sum_{l=0}^{\alpha-\mathbb{H}} \binom{\alpha - \mathbb{H}}{l} \frac{(b\beta)^l}{(1+b\beta)^{\alpha-\mathbb{H}} \Gamma(\mathbb{H}+l)} \Gamma_{inc}\left(\mathbb{H} + l, \frac{T}{b\beta+1}\right) \tag{A.15}
\end{aligned}$$

Q.E.D.

References

- [1] ESA website. [Online]. Available: <https://www.esa.int>
- [2] M. Maffei, A. Aubry, A. De Maio, and A. Farina, "On the exploitability of the Ka band for spaceborne radar debris detection and tracking measurements," in Proc. IEEE Int. Workshop Metrology Aerosp., Jun. 2019, pp. 355–360.
- [3] Committee for the Assessment of NASA's Orbital Debris Programs, Limiting Future Collision Risk to Spacecraft—An Assessment of NASA's Meteoroid and Orbital Debris Programs. Washington, D.C., USA: Nat. Academies Press, 2011.
- [4] J. A. Shaud, Air Force Strategy Study 2020-2030. Montgomery, AL, USA: Air Univ. Press, 2011.
- [5] H. Klinkrad, Space Debris Models and Risk Analysis. Berlin, Germany: Springer-Verlag, 2006.
- [6] H. Klinkrad, F. Alby, D. Alwes, C. Portelli, and R. Tremayne-Smith, "Space debris activities in Europe," in Proc. 4th Eur. Conf. Space Debris, 2005, pp. 1–6.
- [7] H. Wilden et al., "GESTRA—Recent progress, mode design and signal processing," in Proc. IEEE Int. Symp. Phased Array Syst. Technol., 2019, pp. 1–8.
- [8] A. I. Baskakov, A. A. Komarov, and A. V. Ruban, "Estimation of the energy characteristics of a multiposition radar system for the control of small-sized space debris for various orbital zones," in Proc. Prog. Electromagn. Res. Symp., 2018, pp. 470–475.
- [9] J. A. Haimerl, B. Hudson, G. P. Fonder, and D. K. Lee, "Overview of the large digital arrays of the space fence radar," in Proc. IEEE Int. Symp. Phased Array Syst. Technol., 2016, pp. 1–8.

- [10] H. G. Weiss, "The Millstone and Haystack radars," *IEEE Trans. Aerosp. Electron. Syst.*, vol. 37, no. 1, pp. 365–379, Jan. 2001.
- [11] J. M. Usoff, "Haystack ultra-wideband satellite imaging radar antenna," in *Proc. IEEE Benjamin Franklin Symp. Microw. Antenna Subsystem. Radar, Telecommun., Biomed. Appl.*, 2014, pp. 1–3.
- [12] A. P. Cox, C. K. Nebelecky, R. Rudnicki, W. A. Tagliaferri, J. L. Crassidis, and B. Smith, "The space object ontology," in *Proc. 19th Int. Conf. Inf. Fusion*, 2016, pp. 146–153.
- [13] A. Horstmann et al., "Survey of the current activities in the field of modeling the space debris environment at TU Braunschweig," *Aerospace*, vol. 5, no. 2, 2018, Art. no. 37.
- [14] A. Horstmann, E. Stoll, and H. Krag, "A validation method of ESA's MASTER 1 cm population in low Earth orbit," in *Proc. Adv. Maui Opt. Space Surveillance Technol. Conf.*, 2017, pp. 1–11.
- [15] F. D'Amico et al., "Risk mitigation activities for potential collision avoidance events for Cosmo-SkyMed constellation in flight operations," in *Proc. 63rd Int. Astronaut. Congr.*, 2012, pp. 1–11.
- [16] H. Krag and H. Klinkrad, "Surveillance radar design options as a function of cataloguing performance requirements," in *Proc. 5th Eur. Conf. Space Debris*, 2009, pp. 1–9.
- [17] D. Mehrholz, L. Leushacke, W. Flury, R. Jehn, H. Klinkrad, and M. Landgraf, "Detecting, tracking and imaging space debris," *ESA Bull.*, vol. 109, pp. 128–134, 2002.
- [18] F. T. Ulaby and D. G. Long, *Microwave Radar and Radiometric Remote Sensing*. Ann Arbor, MI, USA: Univ. Michigan Press, 2013.
- [19] W. L. Patterson, "The propagation factor, F_p , in the radar equation," in *The Radar Handbook*, M. I. Skolnik, Ed., 3rd ed. New York, NY, USA: McGraw-Hill, 2008, ch. 26.

- [20] Space Engineering—Space Environment, ECSS-E-ST-10-04C, ESA Requirements Standards Division, ECSS, Noordwijk, The Netherlands, 2008.
- [21] “ESA website on space weather.” Accessed: Feb. 12, 2021. [Online]. Available: <http://swe.ssa.esa.int/>
- [22] O. I. Yakovlev, Space Radio Science. New York, NY, USA: Taylor & Francis, 2002.
- [23] D. H. Staelin, A. W. Morgenthaler, and J. A. Kong, Electromagnetic Waves. London, U.K.: Pearson, 1993.
- [24] K. C. Yeh and C. H. Liu, “Radio wave scintillations in the ionosphere,” Proc. IEEE, vol. 70, no. 4, pp. 324–360, Apr. 1982.
- [25] A. I. Eriksson, “Waves in space plasmas,” Lecture Notes, Swedish Inst. Space Phys., Dept. Astron. Space Phys., Uppsala Univ., Uppsala, Sweden, 2004.
- [26] J. G. Proakis and M. Salehi, Digital Communications, 5th ed. New York, NY, USA: McGraw-Hill, 2008.
- [27] L. J. Cantafio, Space-Based Radar Handbook. Norwood, MA, USA: Artech House, 1989.
- [28] Y. Feria, M. Belongie, T. McPheeters, and H. Tan, “Solar scintillation effects on telecommunication links at Ka-band and X-band,” Jet Propulsion Lab, Pasadena, CA, USA, NASA JPL TDA Progress Report TDA PR 42-129, 1997.
- [29] D. D. Morabito, “Solar corona-induced fluctuations on spacecraft signal amplitude observed during solar superior conjunctions of the Cassini spacecraft,” Radio Sci., vol. 42, pp. 1–16, 2007.
- [30] F. De Tiberis et al., “The X/X/Ka-band deep space transponder for the BepiColombo mission to mercury,” Acta Astronaut., vol. 68, no. 5/6, pp. 591–598, Feb. 2010.
- [31] A. Papoulis and S. U. Pillai, Probability, Random Variables and Stochastic Processes. New York, NY, USA: McGraw-Hill, 2002.

- [32] T. E. Humphreys, M. L. Psiaki, J. C. Hinks, B. O. Hanlon, and P. M. Kintner, Jr., "Simulating ionosphere-induced scintillation for testing GPS receiver phase tracking loops," *IEEE J. Sel. Topics Signal Process.*, vol. 3, no. 4, pp. 707–715, Aug. 2009.
- [33] C. M. Ho, M. K. Sue, A. Bedrossian, and R. W. Sniffin, "Scintillation effects on radio wave propagation through solar corona," in *Proc. 27th URSI Gen. Meeting*, 2002.
- [34] P. D. Shaft, "On the relationship between scintillation index and Rician fading," *IEEE Trans. Commun.*, vol. COM-22, no. 5, pp. 731–732, May 1974.
- [35] J. S. Lee and E. Pottier, "Polarimetric Radar Imaging—From Basics to Applications. Boca Raton, FL, USA: CRC Press, 2009.
- [36] E. F. Knott, J. F. Shaeffer, and M. T. Tuley, *Radar Cross Section*. Rijeka, Croatia: SciTech, 2004.
- [37] R. D. De Roo and F. T. Ulaby, "Bistatic specular scattering from rough dielectric surfaces," *IEEE Trans. Antennas Propag.*, vol. 42, no. 2, pp. 220–231, Feb. 1994.
- [38] R. A. Simpson, "Spacecraft studies of planetary surfaces using bistatic radar," *IEEE Trans. Geosci. Remote Sens.*, vol. 31, no. 2, pp. 465–482, Mar. 1993.
- [39] W. Kofman et al., "Comet nucleus sounding experiment by radiowave transmission," *Adv. Space Res.*, vol. 21, no. 11, pp. 1589–1598, 1998.
- [40] P. Z. Peebles, *Radar Principles*. Hoboken, NJ, USA: Wiley, 1998.
- [41] P. Z. Peebles, Jr., "Bistatic radar cross sections of chaff," *IEEE Trans. Aerosp. Electron. Syst.*, vol. AES-20, no. 2, pp. 128–140, Mar. 1984.
- [42] P. Z. Peebles, Jr., "Bistatic radar cross sections of horizontally oriented chaff," *IEEE Trans. Aerosp. Electron. Syst.*, vol. AES-20, no. 6, pp. 798–809, Nov. 1984.

- [43] S. W. Marcus, "Dynamics and radar cross section density of chaff clouds," *IEEE Trans. Aerosp. Electron. Syst.*, vol. 40, no. 1, pp. 93–102, Jan. 2004.
- [44] A. Moreira, P. Prats-Iraola, M. Younis, G. Krieger, I. Hajnsek, and K. P. Papathanassiou, "A tutorial on synthetic aperture radar," *IEEE Geosci. Remote Sens. Mag.*, vol. 1, no. 3, pp. 6–35, Sep. 2013.
- [45] M. I. Skolnik, *Introduction to Radar Systems*, 3rd ed. New York, NY, USA: McGraw-Hill, 2001.
- [46] G. Boscagli, "Strumentazione per Esperimenti di Radio Science con Mercury Orbiter," (translated "Instruments for Radio Science Experiments with Mercury Orbiter") Doctoral Dissertation (in Italian), Aerospace Eng. Dept., La Sapienza Univ. Rome, Rome, Italy, 1999.
- [47] U. R. Kraft, "Gain and G/T of multielement receive antennas with active beamforming networks," *IEEE Trans. Antennas Propag.*, vol. 48, no. 12, pp. 1818–1829, Dec. 2000.
- [48] C. E. Cook, M. Bernfeld, "Radar Signals: An Introduction to Theory and Application," Artech House, 1993.
- [49] A. W. Rihaczek, "Radar resolution of moving targets," *IEEE Trans. Inf. Theory*, vol. IT-13, no. 1, pp. 51–56, Jan. 1967.
- [50] A. W. Rihaczek, "Delay-Doppler ambiguity function for wideband signals," *IEEE Trans. Aerosp. Electron. Syst.*, vol. AES-3, no. 4, pp. 705–711, Nov. 1967.
- [51] O. Montenbruck and E. Gill, *Satellite Orbits: Models, Methods, Applications*. Berlin, Germany: Springer, 2000.
- [52] H. Schaub and J. L. Junkins, *Analytical Mechanics of Space Systems*, 3rd ed. Reston, VA, USA: AIAA, 2014.
- [53] M. Mallick, S. Rubin, and B.-N. Vo, "An introduction to force and measurement modeling for space object tracking," in *Proc. 16th Int. Conf. Inf. Fusion*, 2013, pp. 1013–1020.
- [54] B. A. Jones, D. S. Bryant, B.-T. Vo, and B.-N. Vo, "Challenges of multi-target tracking for space situational

- awareness,” in Proc. 18th Int. Conf. Inf. Fusion, 2015, pp. 1278–1285.
- [55] G. Tommei, A. Milani, and A. Rossi, “Orbit determination of space debris: Admissible regions,” *Celestial Mechanics Dyn. Astron.*, vol. 97, no. 4, pp. 289–304, 2007.
- [56] E. Delande, C. Frueh, J. Franco, J. Houssineau, and D. Clark, “Novel multiobject filtering approach for space situational awareness,” *J. Guid., Control, Dyn.*, vol. 41, no. 1, pp. 59–73, 2018.
- [57] R. P. S. Mahler, *Advances in Statistical Multisource-Multitarget Information Fusion*. Norwood, MA, USA: Artech House, 2014.
- [58] W. G. Bath and G. V. Trunk, “Automatic detection, tracking, and sensor integration,” *The Radar Handbook*, M. I. Skolnik, Ed. New York, NY, USA: McGraw-Hill, 2008, ch. 7.
- [59] L. D. Stone, R. L. Streit, T. L. Corwin, and K. L. Bell, *Bayesian Multiple Target Tracking*. Norwood, MA, USA: Artech House, 2014.
- [60] Y. Bar-Shalom, X. R. Li, and T. Kirubarajan, “Estimation with applications to tracking and navigation: Theory algorithms and software,” Hoboken, NJ, USA: Wiley, 2001.
- [61] R. K. Raney, *Space-Based Remote Sensing Radars*, of the *Radar Handbook*, 3rd ed. M. I. Skolnik, Ed. New York, NY, USA: McGraw-Hill, 2008, ch. 18.
- [62] S. U. Pillai, K. Y. Li, and B. Himed, *Space Based Radar*. New York, NY, USA: McGraw-Hill, 2008.
- [63] J. P. Stralka and W. G. Fedarko, *Pulse Doppler Radar*, of the *Radar Handbook*, 3rd ed. M. I. Skolnik, New York, NY, USA: McGraw-Hill, 2008, ch. 4.
- [64] [Online]. Available: www.gaisler.com
- [65] R. Ginosar, P. Aviely, T. Israeli and H. Meirov, "RC64: High performance rad-hard manycore," 2016 IEEE Aerospace Conference, Big Sky, MT, 2016, pp. 1-9.

- [66] N. Salerno, L. Simone, S. Cocchi, V. Piloni, M. Maffei and O. Cociolillo, "Wideband arbitrary waveform generator for enhanced spaceborne SAR," 2008 European Radar Conference, Amsterdam, 2008, pp. 416-419.
- [67] D. W. Allan, "Time and Frequency (Time-Domain) Characterization, Estimation, and Prediction of Precision Clocks and Oscillators," in IEEE Transactions on Ultrasonics, Ferroelectrics, and Frequency Control, vol. 34, no. 6, pp. 647-654, Nov. 1987.
- [68] D. W. Allan and J. Levine, "A Historical Perspective on the Development of the Allan Variances and Their Strengths and Weaknesses," in IEEE Transactions on Ultrasonics, Ferroelectrics, and Frequency Control, vol. 63, no. 4, pp. 513-519, April 2016.
- [69] L. Simone, M. Maffei, D. Gelfusa and G. Boscagli, "On-board DSP techniques for Radio-Science applications," 2008 10th International Workshop on Signal Processing for Space Communications, Rhodes Island, 2008, pp. 1-10.
- [70] R. J. Mailloux, "Phased Array Antenna Handbook," Artech House, 2018.
- [71] R. L. Haupt, "Antenna Arrays – A Computational Approach," Wiley, 2010.
- [72] D. M. Pozar, "Microwave Engineering," 4th Ed., Wiley, 2011.
- [73] P. Rocca, G. Oliveri, R. J. Mailloux and A. Massa, "Unconventional Phased Array Architectures and Design Methodologies—A Review," in Proceedings of the IEEE, vol. 104, no. 3, pp. 544-560, March 2016.
- [74] S. M. Sherman, D. K. Barton, "Monopulse Principles and Techniques," Artech House, 2011.
- [75] U. R. O. Nickel, E. Chaumette and P. Larzabal, "Statistical Performance Prediction of Generalized Monopulse Estimation," in IEEE Transactions on Aerospace and Electronic Systems, vol. 47, no. 1, pp. 381-404, January 2011.

- [76] E. Mosca, "Angle Estimation in Amplitude Comparison Monopulse Systems," in *IEEE Transactions on Aerospace and Electronic Systems*, vol. AES-5, no. 2, pp. 205-212, March 1969.
- [77] M. Greco, F. Gini and A. Farina, "Joint Use of Sum and Delta Channels for Multiple Radar Target DOA Estimation," in *IEEE Transactions on Aerospace and Electronic Systems*, vol. 43, no. 3, pp. 1146-1154, July 2007.
- [78] P. Rocca and A. F. Morabito, "Optimal Synthesis of Reconfigurable Planar Arrays With Simplified Architectures for Monopulse Radar Applications," in *IEEE Transactions on Antennas and Propagation*, vol. 63, no. 3, pp. 1048-1058, March 2015.
- [79] G. Gottardi, L. Poli, P. Rocca, A. Montanari, A. Aprile and A. Massa, "Optimal Monopulse Beamforming for Side-Looking Airborne Radars," in *IEEE Antennas and Wireless Propagation Letters*, vol. 16, pp. 1221-1224, 2017.
- [80] R. Croci, A. Delfino and F. Marchetti, "Space Based Radar technology evolution," 2009 European Radar Conference (EuRAD), Rome, 2009, pp. 601-604.
- [81] S. Pasupathy, A.N. Venetsanopoulos, "Optimum Active Array Processing Structure and Space-Time Factorability," *IEEE Transactions on Aerospace and Electronic Systems*, Vol. 10, No. 6, November 1974.
- [82] M. Maffei and L. Simone, "Code detection at Launch and Early Orbit Phase for CDMA TT&C," 2008 10th International Workshop on Signal Processing for Space Communications, Rhodes Island, 2008, pp. 1-12.
- [83] [Online]. Available: STMicroelectronics - www.st.com
- [84] J. E. Volder, "The CORDIC Trigonometric Computing Technique," in *IRE Transactions on Electronic Computers*, vol. EC-8, no. 3, pp. 330-334, Sept. 1959.
- [85] A. Aubry, A. D. Maio, V. Carotenuto and A. Farina, "Radar Phase Noise Modeling and Effects-Part I : MTI Filters," in

- IEEE Transactions on Aerospace and Electronic Systems, vol. 52, no. 2, pp. 698-711, April 2016.
- [86] A. Aubry, V. Carotenuto, A. Farina and A. De Maio, "Radar phase noise modeling and effects-part II: pulse doppler processors and sidelobe blankers," in IEEE Transactions on Aerospace and Electronic Systems, vol. 52, no. 2, pp. 712-725, April 2016.
- [87] B. Widrow, I. Kollár,"Quantization Noise: Roundoff Error in Digital Computation, Signal Processing, Control, and Communications," Cambridge University Press, 2008.
- [88] Technologies for European Non-Dependence and Competitiveness (Critical Space Technologies) - SPACE-10-TEC-2018 - Ref. Ares(2017)5361666 - 03/11/2017.
- [89] S. S. Blackman," Multiple-Target Tracking with Radar Applications," Artech House, 1986.
- [90] S. Blackman, R. Popoli,"Design and Analysis of Modern Tracking Systems," Artech House, 1999.
- [91] A. Farina, "Antenna Based Signal Processing Techniques for Radar Systems," Artech House, 1992.
- [92] G. Cui, A. De Maio, M. Piezzo and A. Farina, "Sidelobe Blanking with Generalized Swerling-Chi Fluctuation Models," in IEEE Transactions on Aerospace and Electronic Systems, vol. 49, no. 2, pp. 982-1005, April 2013.
- [93] J. V. DiFranco, W. L. Rubin, "Radar Detection," Scitech Publishing, 2004.
- [94] H. L. Van Trees, "Detection Estimation and Modulation Theory, Part I: Detection, Estimation, and Filtering Theory," Wiley, 2013.
- [95] A. De Maio, M. S. Greco, "Modern Radar Detection Theory," Scitech Publishing, 2015.
- [96] R. J. Muirhead,"Aspects of Multivariate Statistical Theory," Wiley, 2005.
- [97] G. Muntoni et al., "A space debris-dedicated channel for the P-band receiver of the Sardinia radio telescope: A detailed

- description and characterization," *IEEE Antennas Propag. Mag.*, vol. 62, no. 3, pp. 45–57, Jun. 2020.
- [98] G. A. Fabrizio, "High Frequency Over-The-Horizon Radar: Fundamental Principles, Signal Processing, and Practical Applications," McGraw Hill, 2013.
- [99] R. A. Dana and D. L. Knepp, "The Impact of Strong Scintillation on Space Based Radar Design I: Coherent Detection," *IEEE Transactions on Aerospace and Electronic Systems*, vol. AES-19, no. 4, pp. 539-549, July 1983.
- [100] R. A. Dana and D. L. Knepp, "The Impact of Strong Scintillation on Space Based Radar Design II: Noncoherent Detection," *IEEE Transactions on Aerospace and Electronic Systems*, vol. AES-22, no. 1, pp. 34-46, Jan. 1986.
- [101] J. M. Hammersley, D.C. Handscomb, "Monte Carlo Methods," Wiley, 1964.
- [102] R. A. Dana, "Effects of two-way decorrelation on radar detection in scintillation," *IEEE Transactions on Aerospace and Electronic Systems*, vol. 31, no. 2, pp. 795-804, April 1995.
- [103] E. L. Mokole and D. L. Knepp, "Ionospheric scintillation-induced integration losses for space-based radar," *IEEE Transactions on Aerospace and Electronic Systems*, vol. 29, no. 3, pp. 636-650, July 1993.
- [104] J. Marcum, "A statistical theory of target detection by pulsed radar," *IRE Transactions on Information Theory*, vol. 6, no. 2, pp. 59-267, April 1960.
- [105] P. Swerling, "Probability of detection for fluctuating targets," *IRE Transactions on Information Theory*, vol. 6, no. 2, pp. 269-308, April 1960.
- [106] D. A. Shnidman, "Radar detection probabilities and their calculation," *IEEE Transactions on Aerospace and Electronic Systems*, vol. 31, no. 3, pp. 928-950, July 1995.

- [107] D. A. Shnidman, "Expanded Swerling target models," *IEEE Transactions on Aerospace and Electronic Systems*, vol. 39, no. 3, pp. 1059-1069, July 2003.
- [108] P. Swerling, "Radar probability of detection for some additional fluctuating target cases," *IEEE Transactions on Aerospace and Electronic Systems*, vol. 33, no. 2, pp. 698-709, April 1997.
- [109] I. Kanter, "Exact Detection Probability for Partially Correlated Rayleigh Targets," *IEEE Transactions on Aerospace and Electronic Systems*, vol. AES-22, no. 2, pp. 184-196, March 1986.
- [110] A. Farina and A. Russo, "Radar Detection of Correlated Targets in Clutter," *IEEE Transactions on Aerospace and Electronic Systems*, vol. AES-22, no. 5, pp. 513-532, Sept. 1986.
- [111] G. Cui, A. DeMaio and M. Piezzo, "Performance Prediction of the Incoherent Radar Detector for Correlated Generalized Swerling-Chi Fluctuating Targets," *IEEE Transactions on Aerospace and Electronic Systems*, vol. 49, no. 1, pp. 356-368, Jan. 2013.
- [112] A. De Maio and A. Aubry, "Radar Detection, Performance Analysis, and CFAR Techniques," 2019 IEEE Radar Conference (RadarConf), Boston, MA, USA, 2019, pp. 1-120.
- [113] M. A. Richards, J. A. Scheer, and W. A. Holm, *Principles of modern radar: Basic principles*, Scitech Publishing, Inc., 2010.
- [114] C. D. Papanicolopoulos, W. D. Blair, D. L. Sherman and M. Brandt-Pearce, "Use of a Rician Distribution for Modeling Aspect-Dependent RCS Amplitude and Scintillation," 2007 IEEE Radar Conference, Boston, MA, 2007, pp. 218-223.
- [115] X. Song, W. D. Blair, P. Willett and S. Zhou, "Dominant-plus-Rayleigh Models for RCS: Swerling III/IV versus

- Rician," *IEEE Transactions on Aerospace and Electronic Systems*, vol. 49, no. 3, pp. 2058-2064, July 2013.
- [116] M. K. Simon, "Probability Distributions Involving Gaussian Random Variables," Springer, 2002.
- [117] G. Di Blasio and A. Neri, "Modified Q-functions and their use in detection analysis," *IEEE Transactions on Information Theory*, vol. 37, no. 4, pp. 1123-1142, July 1991.
- [118] I. S. Gradshteyn, I. M. Ryzhik, "Tables of Integrals, Series, and Products," Edited by A. Jeffrey and D. Zwillinger, 7th Ed., Academic Press, 2007.
- [119] P. C. Sofotasios, S. Muhaidat, G. K. Karagiannidis and B. S. Sharif, "Solutions to Integrals Involving the Marcum Q-Function and Applications," *IEEE Signal Processing Letters*, vol. 22, no. 10, pp. 1752-1756, Oct. 2015.
- [120] N. Y. Ermolova and O. Tirkkonen, "Laplace Transform of Product of Generalized Marcum Q, Bessel I, and Power Functions With Applications," *IEEE Transactions on Signal Processing*, vol. 62, no. 11, pp. 2938-2944, June 1, 2014.
- [121] W. Rudin, "Principles of Mathematical Analysis," McGraw Hill, 1976.
- [122] M. Abramowitz, I. Stegun," *Handbook of Mathematical Functions with Formulas, Graphs, and Mathematical Tables*," Dover, 1965.
- [123] A. Farina, F. A. Studer (1985). *Radar Data Processing. 1 – Introduction and Tracking*. Research Studies Press. p. 325. ISBN 978-0863800269.
- [124] A. Farina, F. A. Studer (1986). *Radar Data Processing. 2 – Advanced topics and applications*. Research Studies Press. p. 362. ISBN 978-0863800382.
- [125] D. J. Rabideau, P. A. Parker, "Ubiquitous MIMO Multifunction Digital Array Radar ... and the Role of Time-Energy Management in Radar," MIT LL Project Report DAR-4, Issued 10 March 2004.

- [126] J. Li, P. Stoica, "MIMO Radar Signal Processing," Wiley, 2009.
- [127] D. J. Rabideau, "MIMO Radar Waveforms and Cancellation Ratio" IEEE Transactions on Aerospace and Electronic Systems, vol. 48, no. 2, April 2012.
- [128] M. S. Davis, "MIMO Radar," Chapter 4 of "Principles of Modern Radar – Vol II: Advanced Techniques," (Edited by W. L. Melvin, J. A. Scheer), SciTech Publishing, 2013.
- [129] J. Bergin, J. R. Guerci, "MIMO Radar – Theory and Applications," Artech House, 2018.
- [130] F. Daum, J. Huang, "MIMO Radar: Snake Oil or Good Idea?" IEEE AESS Systems Magazine, May 2009.
- [131] D. J. Rabideau, "Hybrid Mitigation of Distortion in Digital Arrays," IEEE, 2005.
- [132] G. Krieger, "MIMO-SAR: Opportunities and Pitfalls," IEEE Transactions on Geoscience and Remote Sensing, vol. 52, no. 5, May 2014.
- [133] M. K. Simon, J. K. Omura, R. A. Scholtz, B. K. Levitt, "Spread Spectrum Communications Handbook," Mc-Graw Hill, 1994.
- [134] D. R. Fuhrmann, G. San Antonio, "Transmit Beamforming for MIMO Radar Systems using Signal Cross-Correlation," IEEE Transactions on Aerospace and Electronic Systems, Vol. 44, No. 1, January 2008.
- [135] W. Huleihel, J. Tabrikian, R. Shavit, "Optimal Adaptive Waveform Design for Cognitive MIMO Radar," IEEE Transactions on Signal Processing, vol. 61, no. 20, October 15, 2013.
- [136] N. Sharaga, J. Tabrikian, H. Messer, "Optimal Cognitive Beamforming for Target Tracking in MIMO Radar/Sonar," IEEE Journal of Selected Topics in Signal Processing, vol. 9, no. 8, December 2015.
- [137] A. Aubry, A. De Maio, Y. Huang, "MIMO Radar Beampattern Design via PSL/ISL Optimization," IEEE

- Transactions on Signal Processing, vol. 64, no. 15, August 1, 2016.
- [138] M. M. Naghsh, M. Modarres-Hashemi, M. A. Kerahroodi and E. H. M. Alian, "An Information Theoretic Approach to Robust Constrained Code Design for MIMO Radars," in IEEE Transactions on Signal Processing, vol. 65, no. 14, pp. 3647-3661, 15 July 15, 2017.
- [139] B. Tang, J. Tang, "Relative Entropy-Based Waveform Design for MIMO Radar," Chapter 10 of the Radar Waveform Design Based on Optimization Theory (Editor G. Cui, A. De Maio, A. Farina, J. Li), IET 2020.
- [140] L. Wu, D. P. Palomar, "Radar Waveform design via the Majorization-Minimization Framework," Chapter 7 of the Radar Waveform Design Based on Optimization Theory (Editor G. Cui, A. De Maio, A. Farina, J. Li), IET 2020.
- [141] C. Gao, K. C. Teh, A. Liu, H. Sun, "Piecewise LFM Waveform for MIMO Radar," IEEE Transactions on Aerospace and Electronic Systems, Vol. 52, No. 2, April 2016.
- [142] G. Solodky, O. Longman, S. Villeval, I. Bilik, "CDMA-MIMO Radar with Tansec Waveform," IEEE Transactions on Aerospace and Electronic Systems, Vol. 57, No. 1, February 2021.
- [143] J. Overvest, F. Jansen, F. Uysal, A. Yarovoy, "Doppler Influence on Waveform Orthogonality in 79 GHz MIMO Phase-Coded Automotive Radar," IEEE Transactions on Vehicular Technology, Vol. 69, No. 1, January 2020.
- [144] S. W. Golomb, G. Gong, "Signal Design for Good Correlation for Wireless Communication, Cryptography, and Radar," Cambridge Univ. Press, 2005.
- [145] A. Suriani, P. Capece, G. Mannocchi, "Developments in SAR Active Phased Array Antennas in Thales Alenia Space" International Symposium on Phased Array Systems and Technology, 15 – 18 Oct., 2019, Waltham, MA, 2019.

- [146] D. J. Bekers, S. Jacobs, S. Monni, R. J. Bolt, D. Fortini, P. Capece, G. Toso, "A Ka-Band Spaceborne Synthetic Aperture Radar Instrument," *IEEE Antennas and Propagation Magazine*, October 2019.
- [147] Millimeter Wave Gallium Nitride Space Evaluation and Application to Observation Satellites (MiGaNSOS) – H2020 Project No. 776322.
- [148] L. Pace, F. Costanzo, P. E. Longhi, W. Ciccognani, S. Colangeli, A. Suriani, R. Leblanc, E. Limiti, "Design of a Ka-Band Single-Chip Front-End based on a 100 nm GaN-on-Si technology," 2020 International Workshop on Integrated Nonlinear Microwave and Millimetre-Wave Circuits (INMMiC), 2020, pp. 1-3.
- [149] M. Parlak and R. J. McGlen, "Cooling of high power active phased array antenna using axially grooved heat pipe for a space application," 2015 7th International Conference on Recent Advances in Space Technologies (RAST), 2015, pp. 743-748.
- [150] U. Nickel, "Target Parameter Estimation and Array Features," Chapter 1 of "Novel Radar Techniques and Applications – Volume 1: Real Aperture Array Radar, Imaging Radar, and Passive and Multistatic Radar," (Edited by R. Klemm, U. Nickel, C. Gierull, P. Lombardo, H. Griffiths, W. Koch), IET, 2018.
- [151] W. D. Wirth, Chapter 11 of "Radar Techniques using Array Antennas," IEE, 2001.
- [152] R. J. Mailloux, S. G. Santarelli, T. M. Roberts, D. Luu, "Irregular Polyomino-Shaped Subarrays for Space-Based Active Arrays," Hindawi Publishing Corporation, *International Journal of Antennas and Propagation* Volume 2009, Article ID 956524, 9 pages.
- [153] Boeringer et al., "Tiled Phased Array Antenna," United States Patent, No.: US 6,621,470 B1, Sep. 16, 2003.

- [154] N. Anselmi, P. Rocca, M. Salucci, A. Massa, "Irregular Phased Array Tiling by means of Analytic Schaemata-Driven Optimization," *IEEE Transactions on Antennas and Propagation*, Vol. 65, No. 9, September 2017.
- [155] N. Anselmi, P. Rocca, C. Castlunger, D. Marcantonio, P. Rosatti, L. Tosato, F. Zardi, E. Rajo-Iglesias, A. Massa, "Domino-Tiling in Phased Arrays Through Innovative/Computational/Analytic Strategies," 2018 IEEE International Symposium on Antennas and Propagation & USNC/URSI National Radio Science Meeting, 2018, pp. 1-2.
- [156] A. Nafe and G. M. Rebeiz, "On the phase center analysis of linear phased-array antennas," 2017 IEEE International Symposium on Antennas and Propagation & USNC/URSI National Radio Science Meeting, 2017, pp. 2023-2024.
- [157] G. San Antonio, D. R. Fuhrmann, F. C. Robey, "Generalized MIMO Radar Ambiguity Functions," Chapter 3 of the *MIMO Radar Signal Processing* (Editor J. Li, P. Stoica), Wiley, 2009.
- [158] H. Urkowitz, C. A. Hauer, J. F. Koval, "Generalized Resolution in Radar Systems," *Proceedings of the IRE*, October 1962.
- [159] A. Dogandzic, A. Nehorai, "Cramér-Rao Bounds for Estimating Range, Velocity, and Direction with an Active Array," *IEEE Transactions on Signal Processing*, vol. 49, No. 6, June 2001.
- [160] Sami W. Asmar, J. W. Armstrong, D. H. Atkinson, D. J. Bell, M. K. Bird, V. Dehant, L. Iess, T.J.W. Lazio, I. R. Linscott, A. J. Mannucci, E. Mazarico, R. S. Park, M. Pätzold, R. A. Preston, and R. A. Simpson, "The Future of Planetary Atmospheric, Surface, and Interior Science Using Radio and Laser Links," 32nd URSI GASS, Montreal, Canada, 2017.
- [161] R. A. Simpson, G. L. Tyler, M. Pätzold, Bernd Häusler, S. W. Asmar, A. K. Sultan-Salem, "Polarization in Bistatic Radar Probing of Planetary Surfaces: Application to Mars

- Express Data,” Proceedings of the IEEE, Vol. 99, No. 5, May 2011.
- [162] D. Cinarelli, A. Di Domenico, A. Palli, S. Martì, N. Salerno, L. Simone, P. Tortora, A. J. Allen, I. C. F. Müller-Wodarg, “On-Board Radio-Science: Science Requirements, System and Architectural Trade-Offs and Preliminary Performance Analysis, ”5th ESA International Workshop on Tracking, Telemetry and Command Systems for Space Applications, ESA-ESTEC – Noordwijk, The Netherlands, 2010.
- [163] NASA website. [Online]. Available: <https://www.nasa.gov>
- [164] Technical Considerations for Enabling a NATO-Centric Space Domain Common Operating Picture (COP) – STO/NATO Technical Report STO-TR-SCI-279, December 2020.
- [165] A Strategic Compass for Security and Defence - For a European Union that protects its citizens, values and interests and contributes to international peace and security - EEAS(2021) 1169.
- [166] A. Farina, G. Battistelli, L. Chisci, A. Di Lallo, “40 years of tracking for radar systems: a cross-disciplinary academic and industrial viewpoint,” ICCAIS Conf. Proceedings, Chiang Mai, Thailand, 2017.
- [167] R. Briskman, “Autonomous Satellite Orbital Debris Avoidance System and Method,” US Patent No.: US 8,333,702 B2, Sep. 16, 2014.
- [168] W. G. Bath, G. V. Trunk, “Automatic Detection, Tracking, and Sensor Integration,” Chapter 7 of the Radar Handbook, 3rd Edition (Editor M.I. Skolnik), Mc Graw Hill, 2008.
- [169] X. R. Li and V. P. Jilkov, "Survey of Maneuvering Target Tracking. Part II: Motion Models of Ballistic and Space Targets," in IEEE Transactions on Aerospace and Electronic Systems, vol. 46, no. 1, pp. 96-119, Jan. 2010.

- [170] S. Haykin, “Cognitive Dynamic Systems: Perception-Action Cycle, Radar and Radio,” Cambridge University Press, 2012.
- [171] K. L. Bell, C. J. Baker, G. E. Smith, J. T. Johnson and M. Rangaswamy, "Cognitive Radar Framework for Target Detection and Tracking," in IEEE Journal of Selected Topics in Signal Processing, vol. 9, no. 8, pp. 1427-1439, Dec. 2015.
- [172] A. Farina, A. De Maio, S. Haykin, “The impact of Cognition on Radar Technology,” Scitech, 2017.
- [173] SpaceFibre Standard, “ECSS-E-ST-50-11C spaceFibre – Very High Speed Serial Link”.
- [174] D. C. Schleher, ”MTI and Pulsed Doppler Radar,” Artech House, 1991.
- [175] A. Benavoli, A. Balleri, and A. Farina, “Joint waveform and guidance control optimization for target rendezvous,” IEEE Trans. Signal Process., vol. 67, no. 16, pp. 4357–4369, Aug. 2019.
- [176] E. Brookner, W. M. Hall, and R. H. Westlake, “Faraday loss for Lband radar and communications systems,” IEEE Trans. Aerosp. Electron. Syst., vol. AES-21, no. 4, pp. 459–469, Jul. 1985.
- [177] P. C. Sofotasios and S. Freear, “The α – κ – μ /gamma distribution: A generalized non-linear multipath/shadowing fading model,” in Proc. Annu. IEEE India Conf., Hyderabad, India, Dec. 2011, pp. 1–6.
- [178] M. D. Yacoub, “The α – η – κ – μ fading model,” IEEE Trans. Antennas Propag., vol. 64, no. 8, pp. 3597–3610, Aug. 2016.
- [179] C. R. N. da Silva, G. R. D. L. Tejerina, and M. D. Yacoub, “The α – η – κ – μ fading model: New fundamental results,” IEEE Trans. Antennas Propag., vol. 68, no. 1, pp. 443–454, Jan. 2020.
- [180] P. C. Sofotasios, T. A. Tsiftsis, Y. A. Brychkov, S. Freear, M. Valkama, and G. K. Karagiannidis, “Analytic expressions

- and bounds for special functions and applications in communication theory,” *IEEE Trans. Inf. Theory*, vol. 60, no. 12, pp. 7798–7823, Dec. 2014.
- [181] E. Biglieri, K. Yao, and C.-A. Yang, “Fading models from spherically invariant processes,” *IEEE Trans. Wireless Commun.*, vol. 14, no. 10, pp. 5526–5538, Oct. 2015.
- [182] E. Conte and M. Longo, “Characterisation of radar clutter as a spherically invariant random process,” *IEE Proc. F Commun., Radar Signal Process.*, vol. 134, no. 2, p. 191, Apr. 1987.
- [183] F. Gini, M. V. Greco, and A. Farina, “Clairvoyant and adaptive signal detection in non-Gaussian clutter: A data-dependent threshold interpretation,” *IEEE Trans. Signal Process.*, vol. 47, no. 6, pp. 1522–1531, Jun. 1999.
- [184] S. M. Rytov, Y. A. Kravtsov, and V. I. Tatarskii, *Principles of Statistical Radiophysics 4—Wave Propagation Through Random Media*. Berlin, Germany: Springer-Verlag, 1989.
- [185] C. Liu, A. Wernik, and K. Yeh, “Propagation of pulse trains through a random medium,” *IEEE Trans. Antennas Propag.*, vol. AP-22, no. 4, pp. 624–627, Jul. 1974.
- [186] T. A. Bekkeng, E. S. Helgeby, A. Pedersen, E. Trondsen, T. Lindem, and J. I. Moen, “Multi-needle Langmuir probe system for electron density measurements and active spacecraft potential control on CubeSats,” *IEEE Trans. Aerosp. Electron. Syst.*, vol. 55, no. 6, pp. 2951–2964, Dec. 2019.
- [187] M. Jehle, O. Frey, D. Small, and E. Meier, “Measurement of ionospheric TEC in spaceborne SAR data,” *IEEE Trans. Geosci. Remote Sens.*, vol. 48, no. 6, pp. 2460–2468, Jun. 2010.
- [188] J. Kepner, “Parallel Matlab for Multicore and Multinode Computers,” SIAM, 2009.
- [189] A. Aubry, A. De Maio, S. Marano, M. Rosamilia, “Single-Pulse Simultaneous Target Detection and Angle Estimation in

- a Multichannel Phased Array Radar,” IEEE Transactions on Signal Processing, vol. 68, 2020.
- [190] G. Cui, A. De Maio, A. Aubry, A. Farina, L. Kong, “Advanced SLB Architectures with Invariant Receivers,” IEEE Transactions on Aerospace and Electronic Systems, vol. 49, no. 2, April 2013.
- [191] G. Cui, A. De Maio, M. Piezzo, A. Farina, “Sidelobe Blanking with Generalized Swerling-Chi Fluctuation Models,” IEEE Transactions on Aerospace and Electronic Systems, vol. 49, no. 2, April 2013.
- [192] E.J. Kelly, “Finite-Sum Expressions for Signal Detection Probabilities,” MIT LL Technical Report 566, Issued 20 May 1981.

End of Thesis